

# **The Physics of a Collisionless Micro-scale Tearing Mode**

Chen Geng

Doctor of Philosophy

University of York  
Physics

August 2020



## Abstract

Microtearing modes and electron temperature gradient modes are two types of micro-instability that are driven by the electron temperature gradient in magnetised plasmas. Both have been widely studied and are well known respectively as an electromagnetic tearing parity mode and an electrostatic twisting parity mode. Microtearing modes, as the tearing parity one, can cause fine scale reconnection of the magnetic field lines in the vicinity of rational flux surfaces. This leads to formation of magnetic islands, which increases the heat and particle flux across the magnetic confinement devices. Microtearing modes therefore are considered as a candidate for anomalous electron heat transport in tokamak plasmas.

Gyrokinetic theories are used in modelling the physics drive mechanism and the stability of micro-scale modes. Early theories for microtearing modes in slab geometry concludes that the drive mechanism of this mode requires a finite collision frequency; thus it is stabilised at low collision frequencies. However, we find in linear gyrokinetic simulations that a fine scale tearing parity instability, driven also by the electron temperature gradients, persists even in the collisionless or electrostatic limit. We demonstrate that this mode has a much larger radial wavenumber than the binormal one and poses numerical challenges to resolve in simulations. The mode growth rate is sensitive to electron finite Larmor radius effects, which are often neglected in previous studies. We develop two linear analytic gyrokinetic models to identify that this collisionless tearing parity mode is consistent with a higher harmonic of the electron temperature gradient mode, which becomes more unstable than the conventional twisting eigenmode under the parameter range in this thesis. When including electromagnetic fields, this mode is capable of forming magnetic islands even in the absence of collisions.

Our study provides an example that tearing parity micro-instabilities can arise from various physics drives. This result brings up thoughts for further studies on turbulent transport in magnetised plasmas.



# Contents

<b>Abstract</b>	<b>i</b>
<b>List of Figures</b>	<b>vii</b>
<b>Acknowledgements</b>	<b>xi</b>
<b>Declaration</b>	<b>xiii</b>
<b>1 Controlled fusion energy</b>	<b>1</b>
1.1 Demands for fusion energy . . . . .	2
1.2 Solutions to controlled fusion confinement . . . . .	5
1.2.1 Ignition and self-sustaining conditions . . . . .	5
1.2.2 Challenges and solutions . . . . .	9
<b>2 Magnetic confinement fusion</b>	<b>11</b>
2.1 Plasma in electromagnetic field . . . . .	11
2.1.1 Charged particle motion . . . . .	11
2.1.2 Kinetic theory and fluid description . . . . .	15
2.2 Magnetic field geometries and coordinates . . . . .	19
2.2.1 From magnetic mirror to tokamak . . . . .	19
2.2.2 Flux surface coordinates . . . . .	22
2.2.2.1 Mapping between toroidal and slab geometries . . . . .	23
2.3 Transport and Micro-instabilities . . . . .	24
2.3.1 Temperature gradient modes . . . . .	25
2.3.2 Microtearing modes . . . . .	26
<b>3 Gyrokinetic theory</b>	<b>31</b>
3.1 Guiding centre coordinates . . . . .	31
3.2 Gyrokinetic ordering . . . . .	32
3.3 Gyrophase averaging . . . . .	33

3.3.1	Finite Larmor radius effects . . . . .	34
3.3.2	Nonlinear effects . . . . .	34
3.3.3	Collision operator . . . . .	34
3.4	Applications of gyrokinetic theory . . . . .	35
3.4.1	MTMs in the slab geometry . . . . .	35
3.4.2	Gyrokinetic simulation programmes . . . . .	40
<b>4</b>	<b>The limitation of the classic slab MTM model</b>	<b>43</b>
4.1	Numerical approach for solving simultaneous eigenmode equations . . . . .	43
4.1.1	Benchmark with previous results . . . . .	46
4.2	Benchmark slab MTMs with GS2 . . . . .	47
4.2.1	The slab collisionless unstable branch . . . . .	49
4.2.2	Convergence verification for simulation data . . . . .	51
4.3	Reviewing and verifying the assumptions in slab model derivation . . . . .	53
4.3.1	Ion dynamics model . . . . .	53
4.3.2	FLR effects from electrons . . . . .	54
4.4	Impact of the collision model . . . . .	56
4.5	Electrostatic limit of the collisionless mode . . . . .	59
<b>5</b>	<b>Developing the collisionless micro-scale tearing mode model</b>	<b>61</b>
5.1	Electrostatic model at zero collision frequency . . . . .	61
5.2	Electromagnetic model at finite collision frequency . . . . .	64
<b>6</b>	<b>Numerical calculation and discussion</b>	<b>71</b>
6.1	Confirming the collisionless instability . . . . .	71
6.1.1	Validation for the small binormal wavenumber condition . . . . .	73
6.1.2	Validation for the electrostatic limit . . . . .	73
6.1.3	The eigenmode harmonic series . . . . .	75
6.2	Magnetic islands in the collisionless model . . . . .	77
6.3	The limitation of our collisionless models . . . . .	79

<b>7</b>	<b>Conclusions and future work</b>	<b>81</b>
7.1	The physics of the collisionless micro-scale tearing mode in slab geometry	81
7.2	Extending to toroidal geometry . . . . .	82
<b>Appendix A Auxiliary derivations</b>		<b>85</b>
A.1	Lagrangian in single particle motion . . . . .	85
A.2	Bessel functions from gyroaveraging . . . . .	86
A.3	Differential of the matrix product . . . . .	87
<b>Appendix B Complexity regarding a Bessel-Legendre integration for developing the electromagnetic model</b>		<b>89</b>
<b>Glossary</b>		<b>93</b>
<b>References</b>		<b>95</b>



# List of Figures

1.1	Nuclear binding energy chart . . . . .	1
1.2	World energy supply by source from 1990 to 2016 . . . . .	3
1.3	Increasing amount of carbon emission from fossil fuel and the growth of global temperature since 1880 . . . . .	4
1.4	Fusion reaction cross sections in the laboratory reference frame . . . . .	5
1.5	Fusion reactivity and Lawson criterion as a function of temperature . . . . .	8
2.1	Single particle motion trajectory in uniform constant magnetic and electric fields . . . . .	12
2.2	Illustration of a non-uniform magnetostatic field with gradient and curvature, and a uniform electrostatic field . . . . .	13
2.3	Illustration of the magnetic mirror concept and the velocity loss cone . . . . .	19
2.4	Illustration of the tokamak magnetic field lines and coils . . . . .	21
2.5	Sketch to explain the toroidal and poloidal magnetic fields in a tokamak . . . . .	21
2.6	Sketch of tokamak flux surface coordinates . . . . .	23
2.7	Mapping between toroidal and slab geometries . . . . .	24
2.8	Illustration of the mechanism for temperature gradient modes . . . . .	26
2.9	Illustration of the mechanism for microtearing modes . . . . .	27
2.10	Structure of MTMs in a tokamak simulation . . . . .	28
2.11	Comparison of the MTM growth rate as a function of collision frequency for slab and toroidal geometries in the literature . . . . .	29
3.1	Illustration of the slab geometry . . . . .	36
4.1	Comparison of the numerical results in the reference slab model . . . . .	47
4.2	Benchmark of eigenmode, comparing analytically reduced slab MTM model and full gyrokinetic simulation GS2 as a function of collision frequency . . . . .	48
4.3	Mode structures in normalised perturbed electrostatic potential and parallel magnetic vector potential for collisional and collisionless instability branches in GS2 simulations . . . . .	49
4.4	Contour plot showing the eigenvalues of $\omega$ calculated from the slab model . . . . .	50

4.5	Convergence verification for GS2 numerical parameter $n\theta$ in the collisionless branch . . . . .	51
4.6	Comparison of the mode structure with sufficient and insufficient grid extent in GS2 simulations . . . . .	52
4.7	Validation test for the small $k_{\parallel}v_i$ assumption using GS2 calculated $ \omega /k_{\parallel}v_i$ values for different collision frequencies . . . . .	53
4.8	Validation for the inference of adiabatic ions using GS2 . . . . .	54
4.9	Validation for the small $k_x$ assumption using GS2 calculated $k_x\rho_i$ values along the collision frequencies . . . . .	55
4.10	Impact of the electron FLR effects on the growth rate of collisionless and collisional branches in GS2 simulations . . . . .	55
4.11	Comparison of the GS2 collision models . . . . .	58
4.12	Growth rate and mode frequency of the collisionless instability as a function of plasma beta . . . . .	58
6.1	Benchmark for eigenvalue as a function of collision frequency between the electromagnetic model and GS2 . . . . .	72
6.2	Mode structures of two harmonics in GS2 simulations of the collisionless instability . . . . .	73
6.3	Validation for the small $k_y$ condition with GS2 simulations . . . . .	74
6.4	Comparison of impact of plasma beta in the electromagnetic model and GS2 . . . . .	74
6.5	Mode structures of the most unstable harmonic in GS2 simulations at different plasma beta . . . . .	75
6.6	Contour plot of $\omega$ calculated from the electrostatic model . . . . .	76
6.7	Growth rate and mode frequency of different harmonics calculated from the electrostatic model and GS2 . . . . .	77
6.8	Magnetic islands structure evolution calculated by the electromagnetic model . . . . .	78
6.9	Benchmark for the collision operators between GS2 and the electromagnetic model . . . . .	80
7.1	GS2 simulations of the collisionless micro-scale tearing parity mode in cylindrical geometry against normalised curvature . . . . .	82

7.2 GS2 simulations showing the impact of the Bessel factor on this collision-less micro-scale tearing parity mode in cylindrical geometry for varying curvature . . . . . 83



## Acknowledgements

The four year's PhD life in York has been a treasurable experience for me. I feel exceedingly grateful for every transferable skills I have developed, for every trustworthy friends I have made, for every scenic places I have been to, and for every cheerful moments I have enjoyed.

I would like to address my special appreciation to my supervisors, Prof. Howard Wilson and Dr. David Dickinson, who have offered invaluable support and guidance throughout my research. Their solid knowledge, intellectual insight and rigorous attitude have greatly inspired me and are a target for me to aspire to. I have made substantial progress through their meticulous feedback and comments, not only in physics but also in English. Particularly, it was a challenging time when we first found the disagreement with an existing theory; it was my supervisors' wisdom that encouraged me to move out of the confusion and to make the breakthrough.

My next thanks come to all PhD, CDT students, postdocs and the administration teams in YPI and the university. Your enthusiastic support on both academic and well-being has made me feel part of a big family. There are too many to thank individually, but all the physics discussions, the science outreach events, the board games and the Christmas trips with you have fulfilled our motivated days. I would also thank all my mountaineering friends in Ben Lairig society. The ridges and caves, the sunshine and storms, and the aurora in the Skye have all become my indelible memories.

Finally and particularly, I give my sincere gratitude to all my family and friends from China, who have consistently cared about and supported me, especially during the last couple of months of the pandemic.

This PhD work was made possible through funding provided by China Scholarship Council and University of York. It was also part of the TDoTP project funded by EPSRC with Grant No. EP/R034737/1. The computationally intensive gyrokinetic simulations were carried out on YARCC and Viking High Performance Computing facilities provided by University of York.



## Declaration

I, Chen Geng, declare that the work presented in this Thesis is my own original work performed at the University of York under the joint supervision of Prof. H. R. Wilson and Dr. D. Dickinson. This work has not been presented for an award at this, or any other, University. All sources are acknowledged as References with the exceptions given below.

Several components of the results given in Chapter 4, Chapter 5 and Chapter 6 have been presented or published in the following forms:

1. (Conference talk) C. Geng, D. Dickinson, and H. Wilson, Pinning down the collisionless microtearing mode, the 46th IoP Plasma Physics Conference, Loughborough UK, 2019;
2. (Conference poster and in conference proceedings) C. Geng, D. Dickinson, and H. Wilson, Physics of the collisionless microtearing mode, the 46th EPS Conference on Plasma Physics, Milan Italy, 2019;
3. (Journal article) C. Geng, D. Dickinson, and H. Wilson, The physics of a small-scale tearing mode in collisionless slab plasmas, *Plasma Physics and Controlled Fusion* 62 (085009), 2020.



# Chapter 1

## Controlled fusion energy

Fusion is the process in which two or more nuclei combine into heavier nuclei and byproduct particles. The total nuclear binding energy<sup>1</sup> of the reactants and products usually changes. This results in the release or absorption of energy as well as the change of total mass. Figure (1.1) reproduced from [1] shows the average binding energy per

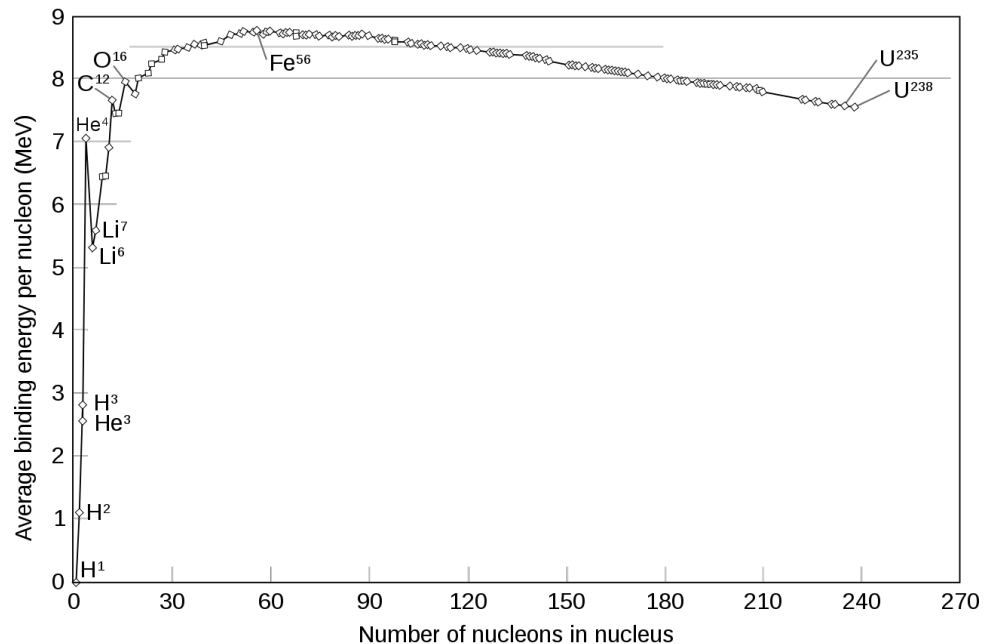
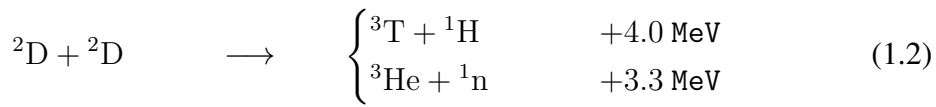


**Figure 1.1:** The nuclear binding energy chart. The isotope notations in this graph  $H^1$ ,  $H^2$  and  $H^3$  stand for hydrogen ( $^1H$ ), deuterium ( $^2D$ ) and tritium ( $^3T$ ). Separated by iron ( $Fe^{56}$  in graph), nuclei on the left side of the curve release energy through fusion reactions while nuclei on the right side release energy through fission reactions. Graph reproduced from [1].

<sup>1</sup>Nuclear binding energy is the minimum required energy to disassemble or form a nucleus into or from its nucleons.

nucleon as a function of the number of nucleons in nucleus. For the elements which are lighter than iron ( $^{56}\text{Fe}$ ), the fusion process will release energy. In nature, fusion of light elements, especially by hydrogen ( $^1\text{H}$ ) and deuterium ( $^2\text{D}$ ), is the process that powers the stars. More commonly, the most preferred<sup>2</sup> fusion reactions include the following.



In general, controlled fusion research aims to find a solution to generate energy from fusion reactions in a safe, controlled and self-sustaining way here on Earth, so that it can be used as an energy source for our human society.

## 1.1 Demands for fusion energy

Most of the world energy consumption today comes directly or indirectly from the sun, the nearest star to the earth. Solar cells and thermal panels are direct ways of using solar energy. Fossil fuel, wind turbine and hydroelectricity are indirect ways. Fossil fuel, including coal, crude oil plus their petroleum products, and natural gas, is a chemical storage of the historical solar energy over the millions of years; both wind and hydropower rely on atmospheric circulation, which is also driven by the solar heat. Other substantial energy sources include nuclear fission, geothermal and biomass. Figure (1.2) reproduced from [3] shows the total supply of energy in the world from 1990 to 2016. The demand of energy is increasing and fossil fuel constitutes over 80% to the total supply.

These energy sources have downsides. Fossil fuel has limited reserves. Studies [4, 5, 6] predict the significant risk for oil supplies to be depleted in about twenty years and for gas and coal in about a hundred years. Meanwhile, burning fossil fuel releases carbon dioxide, which is well known as one of the greenhouse gases. Since the Industrial Revolution, the rapid growth of population and economy has produced billions of tons of carbon dioxide as well as other greenhouse gases into the atmosphere. Studies [7, 8, 9] have shown that the increasing amount of greenhouse gases in the atmosphere caused by human activities, typically carbon dioxide as a primary example, have strong and irreplaceable contributions to the global temperature rising over the last hundred years. Figure (1.3) shows the

---

<sup>2</sup>This means that these reactions have a higher cross section than others. Reaction (1.2) has two approaches with approximately equal possibilities. Details will be discussed in Section 1.2.1. The stellar  $^1\text{H}-^1\text{H}$  reaction is not listed here because of its small cross section [2].

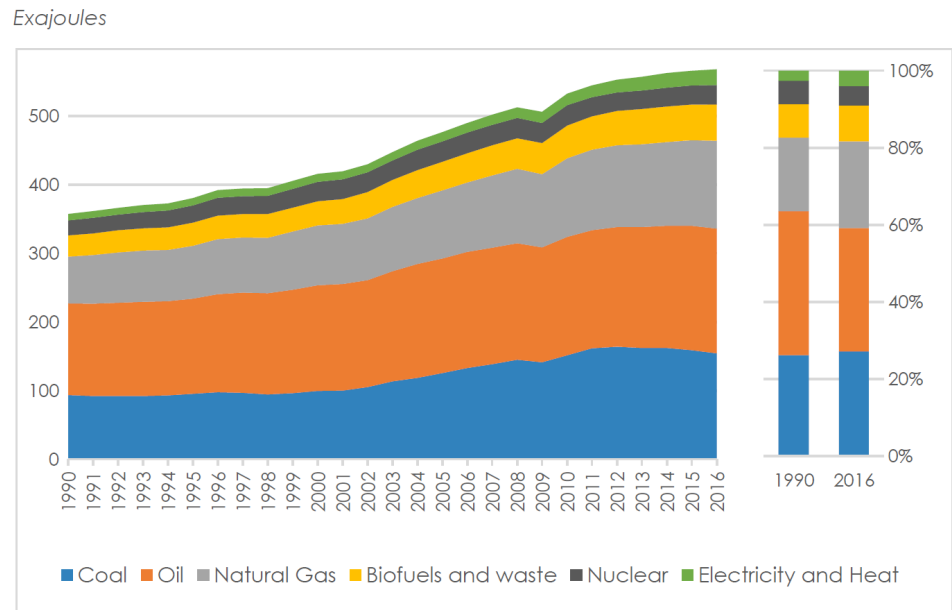


**Figure 1.2:** The world total energy supply by source from 1990 to 2016. The colours of each category represent the source of the supply, in which coal, oil and natural gas are components of fossil fuel. The nuclear category in this graph represents only the fission energy supply. Figure reproduced from [3].

correlation between carbon emission from fossil fuel and global temperature since 1880 [10, 11]. Further increase of global temperature will result in serious climate and ecological crises [12, 13]; therefore we need to replace the use of fossil fuel with other energy resources. However, renewable energy sources, including solar, wind, hydro and geothermal energy, strongly depend on geographic localisation and are distributed unevenly in space and time. Long-distance ultrahigh voltage electricity transmission and advanced energy storage techniques can partially overcome this problem but not completely. Nuclear fission energy does not have site limitation in theory, but maintaining the safety of fission reactors and processing the radioactive waste are a challenge. Overall, we need to look for a better energy resource.

Compared with the above energy resources, fusion has many advantages. The fuels for fusion reactors (deuterium, tritium and helium-3) can be obtained directly or indirectly from seawater and brine<sup>3</sup>, which is globally abundant and transportable; the reaction does not produce greenhouse gases nor large amounts of long-lived radioactive waste<sup>4</sup>, there-

<sup>3</sup>In the reactants of reactions (1.1) to (1.3), only deuterium can be considered as abundant on earth: it constitutes about 0.0115% among isotopes of hydrogen thus can be extracted from seawater without much difficulty; tritium is not stable with the half-life being only 12.32 years thus it is rare in nature; helium-3 is plentiful in the solar system (for example, on the moon) but is scarce on earth [14]. However, tritium and helium-3 can be produced using lithium-6 which is also sufficient in seawater and brine. In fact, the current design of fusion reactors requires deuterium and lithium as the fuels (see Section 1.2.2).

<sup>4</sup>The productions of reactions (1.1) to (1.3) do not contain radioactive particles. However, neutrons ( $^1_0n$ )

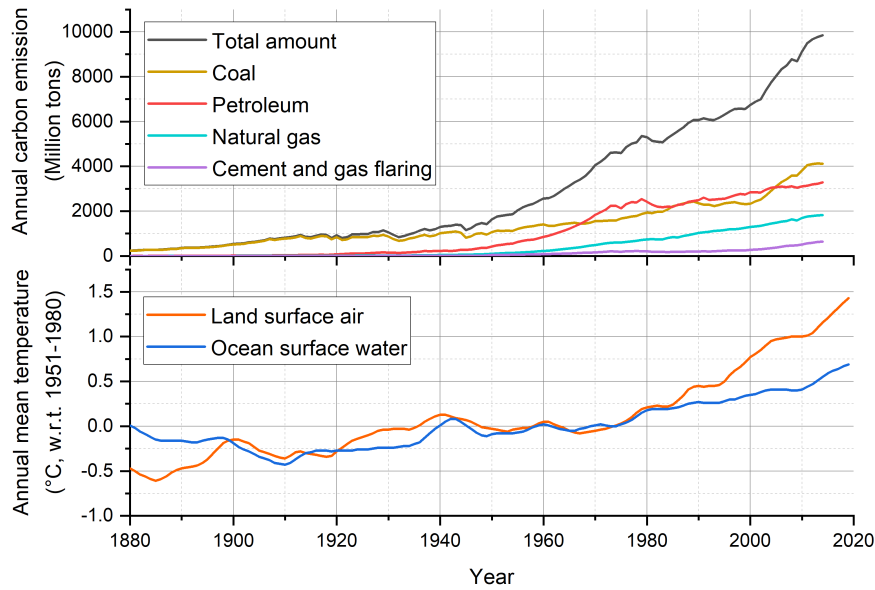


**Figure 1.3:** The increasing amount of carbon emission from fossil fuel (top) and the growth of global temperature (bottom) since 1880. In the top graph, the total amount (black) is the sum of each individual sector (other colours); data obtained from [10]. In the bottom graph, orange and blue curves are global annual mean temperature anomalies averaged over the surface of land and open ocean areas with respect to 1951-1980, fitted with five-year Lowess smoothing; data obtained from [11].

fore fusion reactors are both cleaner and safer; because of the sharp gradient around the fusion reactants on the binding energy curve in figure (1.1), fusion reactions have a much higher energy yield per fuel mass than any other energy resources above, and the potential capacity of fusion energy from available fuel is sufficient to supply our energy demands in the foreseen future.

With the continuous growth of the world economy, the demands for energy will keep increasing [15]. To overcome both energy shortage and climate crisis, research towards realising the potential of fusion energy becomes a must.

can activate other materials when fired into them. Therefore, the materials in the chamber and structures of a fusion reactor, such as stainless steel, can become damaged and radioactive after a period of operating. How to upgrade and recycle those related materials is another important research branch in the fusion research community (see Section 1.2.2).

## 1.2 Solutions to controlled fusion confinement

### 1.2.1 Ignition and self-sustaining conditions

The happening of a fusion reaction requires the reactant nuclei to get close into the nuclear force range. These positive charged particles overcome the Coulomb repulsion during the approaching, therefore intuitively one may believe that the particles' kinetic energy is required to be comparable to the Coulomb potential barrier. However, quantum tunnelling effects allow particles to penetrate the barrier without climbing over the barrier peak [16], so that the fusion reactions actually can occur at a lower impact energy<sup>5</sup>. This quantum tunnelling process determines the outcome of the reaction, which leads the fusion reaction probability to depend on the impact energy. Such a probability is defined as the cross section  $\sigma$ . Figure (1.4) shows the cross sections for fusion reactions (1.1) to (1.3) as a function of kinetic energy.  ${}^2\text{D}-{}^3\text{T}$  fusion generally has the largest cross section compared to the other reactions at the lower end of the temperature range. This makes it the most promising approach. The highest cross section value on top  ${}^2\text{D}-{}^3\text{T}$  curve appears when the kinetic energy is just above 100 keV.

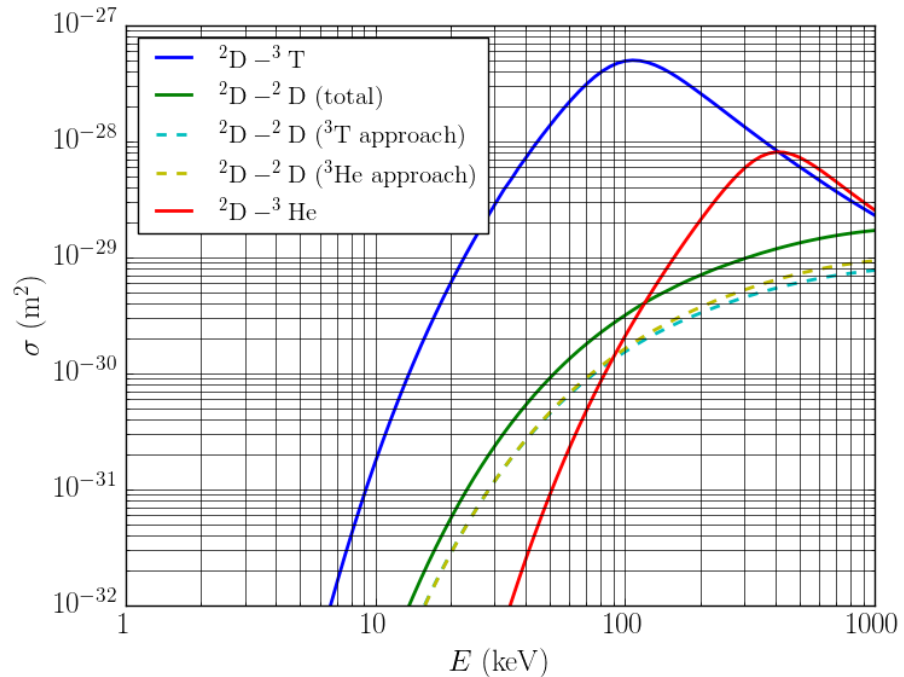


**Figure 1.4:** Cross sections for the fusion reactions (1.1) to (1.3) in the laboratory reference frame. The two dashed lines illustrate the two approaches in reaction (1.2) while the solid line labelled with  ${}^2\text{D}-{}^2\text{D}$  (total) is the sum of the two. Data obtained from [2].

<sup>5</sup>Figures (1.4) and (1.5) to be presented later actually indicate that the majority of fusion reaction occurs in the tail of the distribution.

However, even the peak value of fusion cross section is still very small comparing with the collision cross section, which is around  $10^{-19} \sim 10^{-20} \text{ m}^2$  for isotopes of hydrogen at this range of temperature [17]. This around  $10^8$  times difference means that ordinary collisional scattering is the dominant process when reactant nuclei collide. For fusion to become useful, it requires the energy output to be larger than the ignition input. But each fusion reaction releases only about  $10^2$  times more energy than incident kinetic energy, taking into account the  $10^8$  energy loss in collisions, so it is not possible to gain net energy by injecting particles into each other. In fact, it requires the reactive species to be thermalised and confined together for plenty of contact to take place, and that the kinetic energy of the scattered particles is not wasted. Note that this temperature range is well above the first ionisation energy (for isotopes of hydrogen it is about 13.6 eV; for isotopes of helium it is about 24.6 eV [18]), therefore those thermalised particles are in the state of plasma (see Section 2.1).

The minimum confinement requirement for net energy output can be calculated by balancing input and output power of a fusion reactor. Considering a unit volume in a  ${}^2\text{D}-{}^3\text{T}$  magnetic confinement fusion<sup>6</sup> reactor, for instance, the released energy is carried by the kinetic energies in the products:  $\alpha$  particles ( ${}^4\text{He}$ ) and neutrons. Due to the mass difference of the two,  $\alpha$  particles carry about 20% of the produced energy while neutrons carry the remaining 80%. The  $\alpha$  particles have positive charge so will be constrained in the magnetic field in the reactor and thus heat up the reactants. The neutrons do not have charge so will transport the energy away from the reactor core to be captured for electricity production. Let us assume that reactants deuterium and tritium are fully ionised and their densities are both  $\frac{1}{2}n$  (so that the total plasma density is  $n$ ). Writing the  $\alpha$  particle kinetic energy per reaction as  $E_\alpha$ , so the fuel heating from the  $\alpha$  particles is  $P_{\alpha\text{-heating}} = (\frac{1}{2}n)^2 \langle \sigma v \rangle E_\alpha$ . To maintain the thermal energy in this unit volume at the given temperature<sup>7</sup>  $T$ , the minimum energy confinement time  $\tau_E$  for a reactor running in steady state is given through the power balance condition

$$P_{\alpha\text{-heating}} \cdot \tau_E = \frac{1}{4} n^2 \langle \sigma v \rangle E_\alpha \tau_E \geq W_{\text{thermal}} = 3nT, \quad (1.4)$$

in which  $W_{\text{thermal}} = 3nT$  considers the contribution to the plasma thermal energy from

---

<sup>6</sup>The two types of fusion realisation approaches, magnetic confinement fusion (MCF) and inertial confinement fusion (ICF), will be introduced in Section 1.2.2. The minimum confinement requirement example here is based on the MCF approach, which concerns the relation of particle density and confinement time. The requirement for ICF approach, on the other hand, is equivalently converted to the relation of size and density of the fuel pellet because of its different ignition process.

<sup>7</sup>Unless otherwise specified, temperature  $T$  in this thesis means the thermal kinetic energy and is in the unit of electron-Volts (eV); it converts to the temperature in the unit of Kelvin (K) following  $T [\text{in eV}] = k_B T [\text{in K}]$ , where  $k_B = 1.380649 \times 10^{-23} \text{ m}^2 \text{ kg s}^{-2} \text{ K}^{-1} \approx 8.617333 \times 10^{-5} \text{ eV K}^{-1}$  is the Boltzmann constant.

both ions and electrons and  $\langle\sigma v\rangle$  represents the reactivity (reaction rate averaged over the velocity distribution). Note that this is the ideal power balance condition, which considers only  $\alpha$ -heating and plasma thermal energy, but does not include the heating that comes from the “recycled” neutron energy, and does not include any energy loss due to engineering reality or other related physics processes [19], for example, Bremsstrahlung. In other words, this ideal condition gives out the lower limit for the confinement requirement in reality.

The power balance condition (1.4) gives the Lawson criterion

$$n\tau_E \geq \frac{12T}{\langle\sigma v\rangle E_\alpha}. \quad (1.5)$$

The reactivity  $\langle\sigma v\rangle$  can be calculated as follows. If the species are described by the Maxwellian distribution  $f(v) = n \left(\frac{m}{2\pi T}\right)^{3/2} e^{-mv^2/2T}$  and considering only two-body impact,

$$\begin{aligned} \langle\sigma v\rangle &= \frac{(m_D m_T)^{3/2}}{(2\pi T)^3} \int_{-\infty}^{\infty} \int_{-\infty}^{\infty} \sigma(v_r) v_r e^{-(m_D v_D^2 + m_T v_T^2)/2T} d\mathbf{v}_D d\mathbf{v}_T \\ &= \frac{(m_D m_T)^{3/2}}{(2\pi T)^3} \int_{-\infty}^{\infty} e^{-(m_D + m_T)v_c^2/2T} d\mathbf{v}_c \int_{-\infty}^{\infty} \sigma(v_r) v_r e^{-\mu v_r^2/2T} dv_r \\ &= 4\pi \left(\frac{\mu}{2\pi T}\right)^{3/2} \int_0^{\infty} \sigma(v_r) v_r^3 e^{-\mu v_r^2/2T} dv_r \\ &= \left(\frac{8}{\pi}\right)^{1/2} \left(\frac{\mu}{T}\right)^{3/2} \frac{1}{m_D^2} \int_0^{\infty} \sigma(\varepsilon) \varepsilon e^{-\mu\varepsilon/m_D T} d\varepsilon, \end{aligned} \quad (1.6)$$

in which the subscripts D and T represent deuterium and tritium nuclei, respectively,  $\mathbf{v}_r = \mathbf{v}_D - \mathbf{v}_T$  is the relative particle velocity,  $\mathbf{v}_c = (m_D \mathbf{v}_D + m_T \mathbf{v}_T) / (m_D + m_T)$  is the centre of mass velocity,  $\mu = (m_D m_T) / (m_D + m_T)$  is the reduced mass,  $\varepsilon$  is the impact energy and  $\sigma(\varepsilon)$  is the reaction cross section in figure (1.4).

The Lawson criterion describes a condition on the triple product  $(n, \tau_E, T)$ , which reflects the level of difficulty to operate a controlled fusion facility in engineering. In the form of equation (1.5), the right hand side of the Lawson criterion is a function of temperature. This means that at a given temperature, for the reaction being self-sustaining, it requires the product of density and confinement time of the reactant plasma to be large enough.

Substituting the  ${}^2\text{D}-{}^3\text{T}$  fusion cross section data from figure (1.4) into equation (1.6) then equation (1.5), we can plot the reactivity  $\langle\sigma v\rangle$  and the confinement requirement  $n\tau_E$  as functions of temperature. Figure (1.5) shows the results for reactions (1.1) to

(1.3). The peaks of the reactivity curves appear at lower temperature than that on the cross section curves because of the velocity distribution. Combining the two graphs, the optimised temperature for igniting a  ${}^2\text{D}-{}^3\text{T}$  fusion reactor (in this simple ideal scenario)

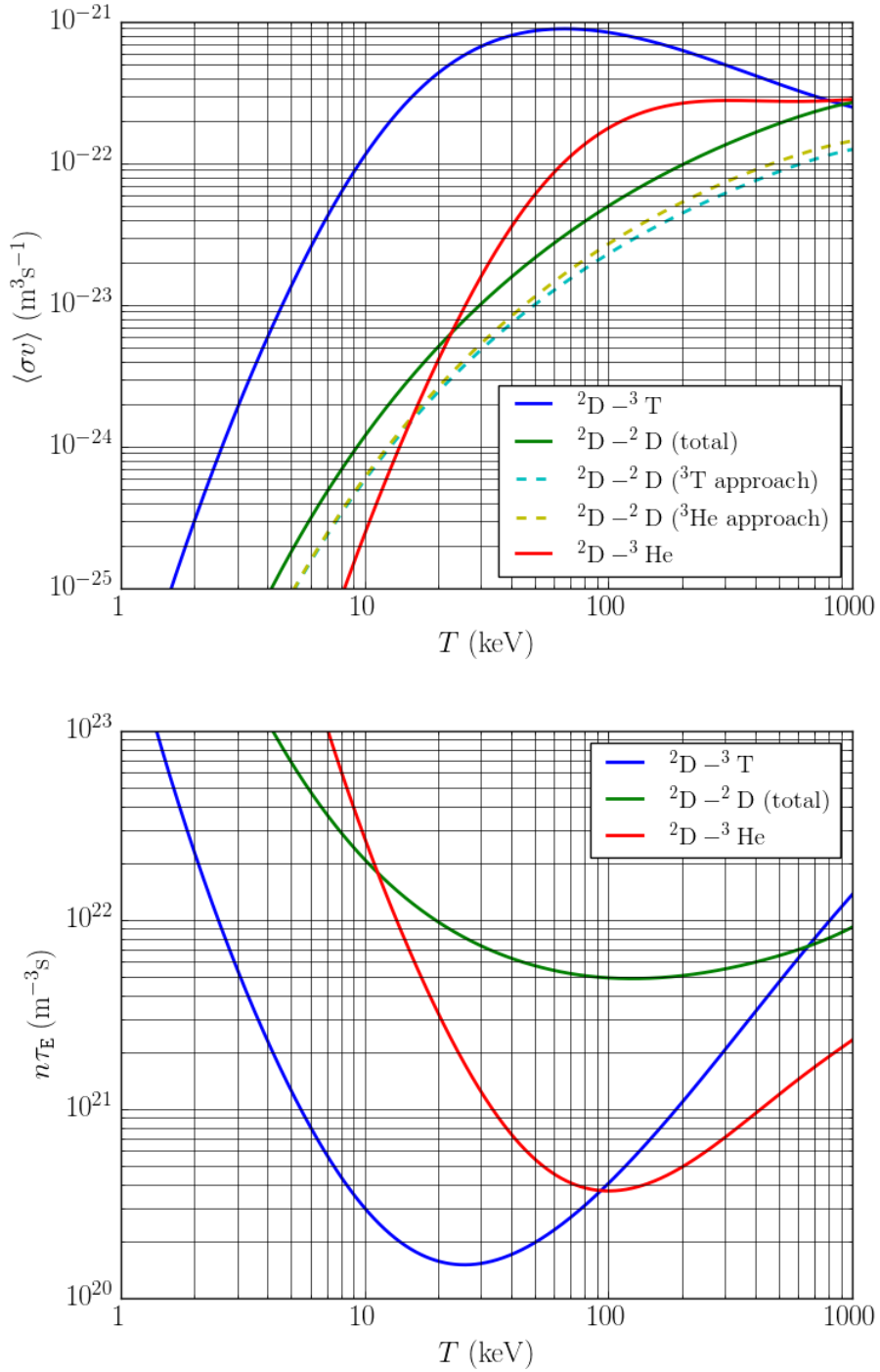


**Figure 1.5:** The fusion reactivity  $\langle\sigma v\rangle$  (top) and Lawson criterion  $n\tau_E$  (bottom) as a function of temperature  $T$  for fusion reactions (1.1) to (1.3). It is unnecessary to calculate  $n\tau_E$  for individual approaches of reaction (1.2).

should be around 30~60 keV, which converts to  $3.5\sim 7.0 \times 10^8$  K. If the density of fusion plasmas reaches  $10^{19}\sim 10^{20} \text{ m}^{-3}$  (for example, the ITER project design [20]), the minimum required confinement time will be  $10^1\sim 10^2$  s. Longer operation time can eventually output net energy.

## 1.2.2 Challenges and solutions

The first challenge is how to tackle the high temperature. As the reaction temperature is extremely high, there is no normal material that can hold the activating fuels for a long time. Currently there are two main solutions, magnetic confinement fusion (MCF) and inertial confinement fusion (ICF); whilst some other novel solutions try to combine MCF and ICF features together, for example magnetised target fusion (MTF) [21].

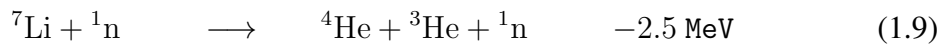
In MCF, magnetic fields are used to constrain the hot plasma via its electromagnetic characteristics. The plasma consists of free-moving ions and electrons. These charged particles are affected by the Lorentz force and can be tethered around the magnetic fields (see Section 2.1). Therefore, the contact of hot plasma and the inner wall of the reactor chamber is limited by magnetic fields and it becomes possible to confine the hot plasma for a sufficient time. Researchers have been studying different designs of magnetic field topology. Many early designs have been proved non-realistic because of the highly chaotic turbulence and transport events in the plasma (see Section 2.3). The most promising MCF designs now are the tokamak [22, 23], stellarator [24, 25] and reversed-field pinch [26, 27]. Generally speaking, these devices all confine plasma in a toroidal magnetic field geometry, but the different field configurations brings in unique characteristics and physics challenges [28, 29], for example, how to heat the plasma and how to generate the required current. This thesis focuses on one type of physics challenge about the transport issues (micro-instabilities, see Section 2.3.2).

ICF, on the other hand, aims at achieving an ultra high density while conducting the reaction for a very short time. The reactant fuels in a pellet shape are rapidly compressed by high energy laser pulses to create the ignition reaction before the fuel disperses apart. ICF designs include direct drive and indirect drive, in which the former focuses the lasers directly at the pellet while the latter converts the energy in lasers to X-rays first.

The second challenge is material, which includes structural material designing and fuel mining. Although the MCF confinement designs reduce the heating load on the surface of the reactor chamber, the material is still in extreme conditions. Meanwhile, the generated neutrons in reaction (1.1) or (1.2) can cause degradation of the material structures around the reactor. Consequences include activation of the material, reduction in the structural

strength or changes in the (super-)conductivity characteristics. The related material study is also an important part of fusion research community.

Apart from the carrying output energy (positive effect) and causing material degradation (negative effect), the generated neutrons can also be used to produce tritium or helium-3. As mentioned in Section 1.1, these two elements are not naturally abundant. One solution for this is to produce the fuel from lithium-6 ( ${}^6\text{Li}$ ) and lithium-7 ( ${}^7\text{Li}$ ). This process is called lithium breeding.



For reactions (1.7) and (1.9), the process can be integrated within a reactor via design of the lithium wall.

As the proverb says “where there is a will there is a way”, though challenges exist, we strongly believe that with the efforts from generations of fusion scientist community, the utilisation of controlled fusion energy is coming.

# Chapter 2

## Magnetic confinement fusion

### 2.1 Plasma in electromagnetic field

The reactant particles for fusion are thermalised to an energy that is significantly higher than its ionisation energy, thus the particles unbind into free-moving electrons and ions (fully ionised). The system is defined as a plasma when the mixture state of these electrons, ions and remaining neutral particles (in a more general sense) features with quasineutral and collective behaviour [30]. Since the plasma consists of charged components, it interacts with electromagnetic fields. However, the two fundamental characteristics of the plasma give its ability to shield out distant external electric potentials by redistributing the ample free-moving charged particles in space. This ability is called Debye shielding. External magnetic fields cannot be shielded out in the same way, and will provide a way to confine the plasma. One of the core tasks for MCF research is to find out the special configuration of magnetic fields to be able to confine plasma to meet the requirement in equation (1.4).

#### 2.1.1 Charged particle motion

Charge particles experience the Lorentz force in the electromagnetic field. In the most simple but general case which exhibits finite uniform constant magnetostatic field  $\mathbf{B}$  and electric static field  $\mathbf{E}$ , a single charged particle with mass  $m$  and charge  $q$  obeys the Lorentz force

$$m \frac{d\mathbf{v}}{dt} = q(\mathbf{E} + \mathbf{v} \times \mathbf{B}). \quad (2.1)$$

The solution of the particle velocity  $\mathbf{v}$  for this linear non-homogeneous differential equation is a superposition of a gyromotion about the magnetic field line and a transverse drift

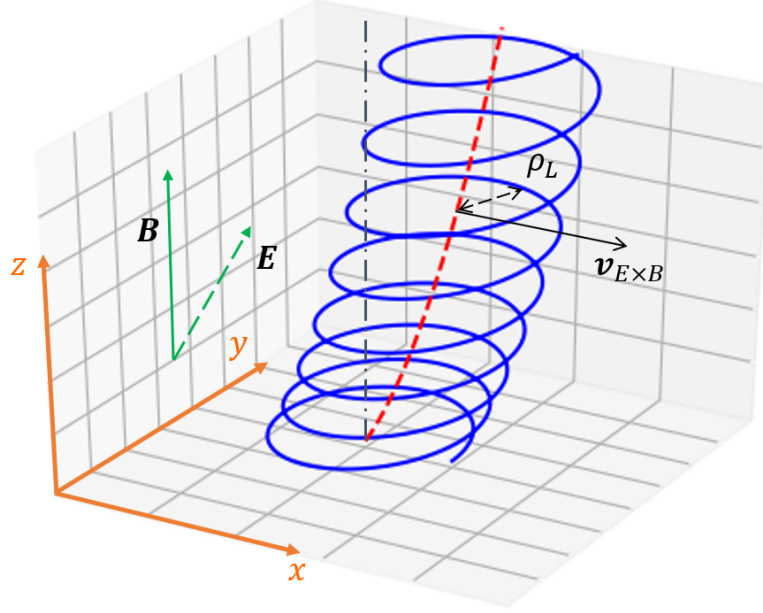


**Figure 2.1:** An example illustration for the single particle motion trajectory in uniform constant magnetic field  $\mathbf{B}$  and electric field  $\mathbf{E}$ . The coordinates are chosen as such that  $z$  axis is parallel to magnetic field while electric field is parallel to  $y$ - $z$  plane. The blue solid spiral is the trajectory for an electron, as an example; the red dashed curve notates the positions of the guiding centre. Gyroradius  $\rho_L$  and  $\mathbf{E} \times \mathbf{B}$  drift velocity  $\mathbf{v}_{E \times B}$  are labelled in this illustration.

motion across the magnetic field line, as is illustrated in figure (2.1). In the coordinates which are defined as in the figure, the motion of the particle at time  $t$  follows

$$\begin{cases} v_x = -v_{\perp} \sin\left(\frac{qB}{m}t + \theta_0\right) + \frac{E_y}{B}, & (2.2) \end{cases}$$

$$\begin{cases} v_y = v_{\perp} \cos\left(\frac{qB}{m}t + \theta_0\right), & (2.3) \end{cases}$$

$$\begin{cases} v_z = v_{z0} + \frac{qE_z}{m}t, & (2.4) \end{cases}$$

in which  $v_{\perp} = \sqrt{(v_x - E_y/B)^2 + v_y^2} = \sqrt{(v_{x0} - E_y/B)^2 + v_{y0}^2}$  where  $v_{x0}$ ,  $v_{y0}$  and  $v_{z0}$  are initial velocity components along  $x$ ,  $y$  and  $z$  axes, respectively; phase  $\theta_0$  depends on the initial direction of  $v_{\perp}$ . If we define the central point of the gyration as the guiding centre, then the motion of the particle can be described as the guiding centre's translational motion plus the particle's circular motion around the guiding centre. This guiding centre description can simplify mathematical equations under certain conditions - the derived gyrokinetic theory will be introduced in Section 3.3. The radius of the particle's circular

motion is named the Larmor radius or gyroradius  $\rho_L$ ,

$$\rho_L = \frac{mv_{\perp}}{qB} = \frac{v_{\perp}}{\omega_c}, \quad (2.5)$$

in which  $\omega_c = qB/m$  is the gyrofrequency. The guiding centre's perpendicular motion component is perpendicular to both magnetic field and electric field. This is referred to as the  $\mathbf{E} \times \mathbf{B}$  drift  $\mathbf{v}_{E \times B}$  and is

$$\mathbf{v}_{E \times B} = \frac{\mathbf{E} \times \mathbf{B}}{B^2}. \quad (2.6)$$

Note that the  $\mathbf{E} \times \mathbf{B}$  drift is independent of either perpendicular velocity nor particle's charge and mass, therefore ions and electrons drift with the same velocity.

In a more general scenario when the magnetic field is not uniform but has gradient and curvature, the particle will experience other drifts. Let us consider the layout of a magnetostatic field  $\mathbf{B}$  as is illustrated in figure (2.2) and a homogeneous electrostatic field  $\mathbf{E}$ . The magnetic field gradient vector  $\nabla B$  and the curvature vector (normal vector)  $\mathbf{R}_c$  are labelled in the figure. The solution for  $v_x$ ,  $v_y$  and  $v_z$  depends on the specific shape of  $\mathbf{B}$  and can be very complex. An insight expression uses the guiding centre description and calculates the velocity components parallel to and perpendicular to the magnetic

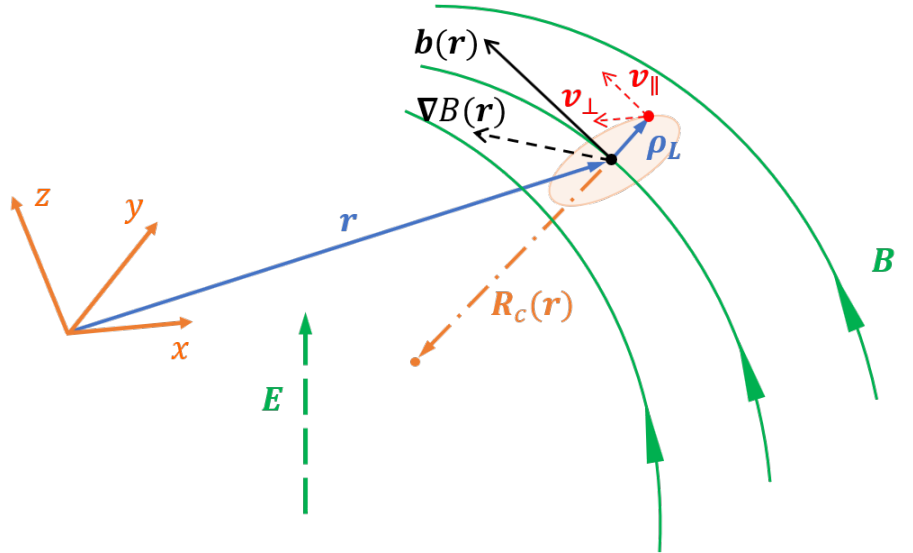


**Figure 2.2:** The illustration of a non-uniform magnetostatic field  $\mathbf{B}$  with gradient and curvature, and a uniform electrostatic field  $\mathbf{E}$ . In this figure,  $\mathbf{b}$  is the unit direction vector of the magnetic field at the guiding centre position  $\mathbf{r}$ ;  $\nabla B$  is the magnitude gradient vector;  $\mathbf{R}_c$  is the curvature vector;  $\rho_L$  is the particle's position with respect to the guiding centre;  $\mathbf{v}_{\parallel}$  and  $\mathbf{v}_{\perp}$  are the particle's velocity components parallel to and perpendicular to  $\mathbf{b}$ , respectively. The direction of  $\mathbf{v}_{\perp}$  shown here is for the electrons as an example.

field. As shown in the figure, the velocity components are  $v_{\parallel} = |\mathbf{v}_{\parallel}| = |\mathbf{v} \cdot \mathbf{b}|$  and  $v_{\perp} = |\mathbf{v}_{\perp}| = |-(\mathbf{v} \times \mathbf{b}) \times \mathbf{b}|$ , where  $\mathbf{b} = \mathbf{B}/B$  is the unit direction vector along the magnetic field line. A more rigorous, Lagrangian approach [31] to derive the particle's motion can be found in Appendix A.1. Here, we present an intuitive picture by looking at the effective forces. The gyration of a charged particle in a magnetic field has magnetic moment  $\boldsymbol{\mu}$

$$\boldsymbol{\mu} = -\frac{mv_{\perp}^2}{2B}\mathbf{b} = -\mu\mathbf{b}, \quad (2.7)$$

which leads to the potential energy  $-\boldsymbol{\mu} \cdot \mathbf{B}$  in the magnetic field. The force related to this is  $-\nabla(-\boldsymbol{\mu} \cdot \mathbf{B})$ . Besides, the parallel motion along the curved magnetic field requires a centripetal force which is given by  $mv_{\parallel}^2 \mathbf{R}_c/R_c^2$ . Note that  $\mathbf{R}_c/R_c^2 = (\mathbf{b} \cdot \nabla)\mathbf{b}$ , therefore the particle's motion equation becomes

$$m \frac{d\mathbf{v}}{dt} = q(\mathbf{E} + \mathbf{v} \times \mathbf{B}) + \nabla(\boldsymbol{\mu} \cdot \mathbf{B}) - mv_{\parallel}^2 (\mathbf{b} \cdot \nabla)\mathbf{b}. \quad (2.8)$$

When the variation of  $\mathbf{B}$  is small compared with the Larmor radius,  $\mu$  is an adiabatic invariant<sup>1</sup> (see Appendix A.1). Therefore, the parallel component of equation (2.8) is

$$\frac{dv_{\parallel}}{dt} = \frac{q}{m}E_{\parallel} - \frac{\mu}{m}\nabla_{\parallel}B, \quad (2.9)$$

in which  $E_{\parallel} = \mathbf{E} \cdot \mathbf{b}$  and  $\nabla_{\parallel}B = \nabla B \cdot \mathbf{b}$ . Compared with the  $z$  direction in equation (2.4), the additional term  $-\mu\nabla_{\parallel}B/m$  indicates that the particle experiences a reflecting force when moving at the direction of increasing magnetic strength, regardless of whether positive or negative charge. This force redistributes the particle energy in  $v_{\parallel}$  and  $v_{\perp}$ , and is called the magnetic mirror force.

Note that the magnetic field does not vary with time. The perpendicular component of equation (2.8) can be obtained from the cross product with  $\mathbf{B}$

$$\frac{d\mathbf{v}}{dt} \times \mathbf{B} = \frac{d\mathbf{v}_{\perp}}{dt} \times \mathbf{B} = \left[ \frac{q}{m}(\mathbf{E} + \mathbf{v}_{\perp} \times \mathbf{B}) - \frac{\mu}{m}\nabla B - v_{\parallel}^2 (\mathbf{b} \cdot \nabla)\mathbf{b} \right] \times \mathbf{B}. \quad (2.10)$$

When  $\mathbf{E}$  and  $\nabla B$  are small, in a *posterior* condition that  $dv_{\parallel}/dt \ll |d\mathbf{v}_{\perp}/dt|$ , the solution can be written as  $\mathbf{v}_{\perp}(t) = \mathbf{v}_c(t) + \mathbf{v}_D$ , in which  $\mathbf{v}_c(t)$  is the homogeneous solution for  $d\mathbf{v}_{\perp}/dt = (q/m)\mathbf{v}_{\perp} \times \mathbf{B}$ . This gives the gyration motion with  $\omega_c$  and  $\rho_L$  as in the

---

<sup>1</sup>An adiabatic variant is a constant of the motion. In the further general case where  $\mathbf{B}$  and  $\mathbf{E}$  vary in both space and time, slow temporal variation is also required for  $\mu$  being an adiabatic invariant. Mathematically that is to say,  $\mu$  is conserved to leading order of  $x/\rho_L$  and  $\omega/\omega_c$ , where  $x$  and  $\omega$  are spatial and temporal characteristic variation of the field, respectively.

uniform fields. The quantity  $\mathbf{v}_D$  is the drift velocity, which is given by

$$\frac{q}{m} (\mathbf{E} \times \mathbf{B} + \mathbf{v}_D \times \mathbf{B} \times \mathbf{B}) - \frac{\mu}{m} \nabla B \times \mathbf{B} - v_{\parallel}^2 (\mathbf{b} \cdot \nabla) \mathbf{b} \times \mathbf{B} = 0. \quad (2.11)$$

Therefore,

$$\begin{aligned} \mathbf{v}_D &= \frac{\mathbf{E} \times \mathbf{B}}{B^2} + \frac{\mu}{q} \frac{\mathbf{B} \times \nabla B}{B^2} + \frac{mv_{\parallel}^2}{qB^2} \mathbf{B} \times (\mathbf{b} \cdot \nabla) \mathbf{b} \\ &= \mathbf{v}_{\mathbf{E} \times \mathbf{B}} + \mathbf{v}_{\nabla B} + \mathbf{v}_R, \end{aligned} \quad (2.12)$$

in which the two new drifts are the grad-B drift  $\mathbf{v}_{\nabla B}$  and the curvature drift  $\mathbf{v}_R$ . These two drifts are charge- and mass-dependent.

The equations describing single particle motion give a clear picture of a charged particle's behaviour in a *given (known)* field. However, in a real plasma each ion and electron contributes to the electromagnetic field; vice versa the field influences each particle's motion. The time-varying self-consistent situation makes it difficult to solve the plasma's evolution using simple single particle motion method. Considering the large number of particles in a plasma, a statistical method is to be introduced in the next section.

### 2.1.2 Kinetic theory and fluid description

Kinetic theory employs the phase-space distribution function  $f_s(\mathbf{r}, \mathbf{v}, t)$  for each species  $s$  to describe the system. The macroscopic physics quantities are determined by the ensemble average of this distribution function. Integrating over the whole velocity domain gives the number density of one species  $n_s(\mathbf{r}, t) = \int_{-\infty}^{\infty} f_s(\mathbf{r}, \mathbf{v}, t) d\mathbf{v}$ . Furthermore, the total particle number of a species is  $N_s(t) = \int_{-\infty}^{\infty} \int_V f_s(\mathbf{r}, \mathbf{v}, t) d\mathbf{v} d\mathbf{r}$ , where the integral range over the spatial domain covers the whole volume  $V$ . The average flow velocity is  $\mathbf{u}_s = \frac{1}{n_s} \int_{-\infty}^{\infty} \mathbf{v} f_s(\mathbf{r}, \mathbf{v}, t) d\mathbf{v}$ . The charged particles' contribution to the electromagnetic field can be determined using the overall charge density  $\sigma(\mathbf{r}, t)$  and the current density  $\mathbf{j}(\mathbf{r}, t)$  via Maxwell's equations, in which

$$\sigma(\mathbf{r}, t) = \sum_s q_s \int_{-\infty}^{\infty} f_s(\mathbf{r}, \mathbf{v}, t) d\mathbf{v}, \quad (2.13)$$

$$\mathbf{j}(\mathbf{r}, t) = \sum_s q_s \int_{-\infty}^{\infty} \mathbf{v} f_s(\mathbf{r}, \mathbf{v}, t) d\mathbf{v}. \quad (2.14)$$

The continuity equation in the six dimensional phase-space gives the general kinetic equation (Boltzmann equation)

$$\frac{df_s}{dt} = \frac{\partial f_s}{\partial t} + \frac{d\mathbf{r}}{dt} \cdot \nabla f_s + \frac{d\mathbf{v}}{dt} \cdot \nabla_{\mathbf{v}} f_s = C_s(f_s, f_{s'}), \quad (2.15)$$

in which  $C_s(f_s, f_{s'})$  represents collisions between species  $s$  and  $s'$ , and we consider no source term. The collisions between charged particles in a plasma differ from those in a neutral gas. Due to the long-range Coulomb interaction, the collisions in plasmas are dominated by small-angle scattering. Taking only binary interactions into account gives the well-known Fokker-Planck collision operator, though the exact form of it will not be discussed in this thesis. When  $C_s = 0$  and substituting the Lorentz force from equation (2.1), equation (2.15) becomes the Vlasov equation

$$\frac{\partial f_s}{\partial t} + \mathbf{v} \cdot \nabla f_s + \frac{q_s}{m_s} (\mathbf{E} + \mathbf{v} \times \mathbf{B}) \cdot \nabla_{\mathbf{v}} f_s = 0. \quad (2.16)$$

Taking the moments<sup>2</sup> of the kinetic equation will give a fluid description for the plasma. The lowest (zeroth) order moment of the Vlasov equation results in the continuity equation as follows

$$\begin{aligned} 0 &= \int_{-\infty}^{\infty} \left[ \frac{\partial f_s}{\partial t} + \mathbf{v} \cdot \nabla f_s + \frac{q_s}{m_s} (\mathbf{E} + \mathbf{v} \times \mathbf{B}) \cdot \nabla_{\mathbf{v}} f_s \right] d\mathbf{v} \\ &= \frac{\partial}{\partial t} \int_{-\infty}^{\infty} f_s d\mathbf{v} + \nabla \cdot \int_{-\infty}^{\infty} \mathbf{v} f_s d\mathbf{v} \\ &\quad + \frac{q_s}{m_s} \int_{-\infty}^{\infty} \nabla_{\mathbf{v}} \cdot [f_s (\mathbf{E} + \mathbf{v} \times \mathbf{B})] d\mathbf{v} \quad \textcircled{1} \quad - \frac{q_s}{m_s} \int_{-\infty}^{\infty} f_s \nabla_{\mathbf{v}} \times (\mathbf{v} \times \mathbf{B}) d\mathbf{v} \quad \textcircled{2} \\ \implies \frac{\partial n_s}{\partial t} + \nabla \cdot (n_s \mathbf{u}_s) &= 0. \end{aligned} \quad (2.17)$$

The term  $\textcircled{1}$  is zero provided that  $f_s \rightarrow 0$  as  $\mathbf{v} \rightarrow \infty$ ; the term  $\textcircled{2}$  is zero because of  $(\mathbf{v} \times \mathbf{B}) \perp \mathbf{v}$ . Furthermore, the first order moment is the momentum (force-balance) equation

$$m_s n_s \left[ \frac{\partial \mathbf{u}_s}{\partial t} + (\mathbf{u}_s \cdot \nabla) \mathbf{u}_s \right] = n_s (\mathbf{E} + \mathbf{u}_s \times \mathbf{B}) - \nabla \cdot \mathbf{P}_s, \quad (2.18)$$

in which  $\mathbf{P}_s = m_s \int_{-\infty}^{\infty} (\mathbf{v}\mathbf{v} - \mathbf{u}\mathbf{u}) f_s d\mathbf{v}$  is the pressure tensor. In an isotropic system, this reduces to the scalar pressure  $p_s$  times the identity matrix, where  $p_s = \frac{1}{3} m_s \int_{-\infty}^{\infty} v^2 f_s d^3v =$

---

<sup>2</sup>The moment is an integral measure of the shape of a function. In general, the  $n$ -th order moment  $\mu_n$  for a real continuous function  $f(x)$  is  $\mu_n = \int_{-\infty}^{\infty} x^n f(x) dx$ .

$n_s T_s$  if  $f_s$  is Maxwellian.

Equations (2.17) and (2.18) provide a fluid description. To close the set of equations can include Maxwell's equations for  $\mathbf{E}$  and  $\mathbf{B}$ , which couple to the charge density and current density in equations (2.13) and (2.14), and the adiabatic thermodynamic equation of state for  $p_s$

$$\frac{\nabla p_s}{p_s} = \gamma_s \frac{\nabla n_s}{n_s}, \quad (2.19)$$

in which  $\gamma$  is the heat capacity ratio. This set of equations, also referred to as magnetohydrodynamics (MHD) equations, provide a more comprehensive description for the plasma system than the single particle motion picture. One inference conclusion coming from this fluid description is the diamagnetic drift  $\mathbf{v}_{\nabla p}$ . Considering an isotropic and slowly varying approximation where  $-i\partial/\partial t \ll \omega_c$ , taking the cross product of the momentum equation (2.18) with  $\mathbf{B}$ , we can get the perpendicular drift in this situation as

$$\mathbf{u}_{sD} = \frac{\mathbf{E} \times \mathbf{B}}{B^2} + \frac{\mathbf{B} \times \nabla p_s}{q_s n_s B^2}. \quad (2.20)$$

The first term is the  $\mathbf{E} \times \mathbf{B}$  drift in equation (2.6). The second term is a new drift caused by the pressure gradient in the fluid, which is defined as the diamagnetic drift

$$\mathbf{v}_{\nabla p} = \frac{\mathbf{B} \times \nabla p_s}{q_s n_s B^2}. \quad (2.21)$$

Note that this diamagnetic drift is charge-dependent, thus the motion of electrons and ions leads to a diamagnetic current, which generates a magnetic field that mitigates the external magnetic field  $\mathbf{B}$ . Although the diamagnetic drift can be regarded as a combination of the gyromotion and the magnetic drift, the phenomena of diamagnetic drift cannot be captured by the single particle motion equations.

In the most simple plasma system where there are two species, ions with  $q_i = +e$  and electrons with  $q_e = -e$ , the equilibrium of the force-balance equation (2.18) gives

$$\mathbf{j} \times \mathbf{B} = \nabla p, \quad (2.22)$$

where  $p$  is the total pressure. Considering  $\nabla \times \mathbf{B} = \mu_0 \mathbf{j}$ , we have

$$\begin{aligned} \nabla p &= \frac{1}{\mu_0} \left[ (\mathbf{B} \cdot \nabla) \mathbf{B} - \frac{1}{2} \nabla B^2 \right] \\ \implies \frac{1}{\mu_0} (\mathbf{B} \cdot \nabla) \mathbf{B} - \nabla \left( p + \frac{B^2}{2\mu_0} \right) &= 0. \end{aligned} \quad (2.23)$$

The first term is the magnetic tension which is caused by the curvature of the field line;

from the second term we can define the magnetic pressure as  $B^2/2\mu_0$  and a ratio of plasma pressure to the magnetic pressure as  $\beta$

$$\beta = \frac{P}{B^2/2\mu_0}. \quad (2.24)$$

This ratio measures the efficiency of a magnetic confinement system [32]. For the plasma instabilities to be discussed later in this thesis,  $\beta$  also determines the strength of the magnetic fluctuations compared to the electrostatic ones (see Section 4.5).

Both MHD equations and kinetic theory can demonstrate that plasma in an electromagnetic field is not stationary but usually supports waves and instabilities, which is where the MCF research heavily focuses<sup>3</sup>. A famous fundamental example can be seen by assuming a small perturbation in the electron distribution function and electric field

$$f(\mathbf{r}, \mathbf{v}, t) = f_0(\mathbf{v}) + f_1(\mathbf{r}, \mathbf{v}, t), \quad (2.25)$$

$$\mathbf{E} = \mathbf{E}_0 + \mathbf{E}_1, \quad \mathbf{B} = 0 \quad (2.26)$$

Here we drop the subscripts for species and use 0 and 1 to represent the equilibrium part and fluctuations, respectively. For our present purpose, the ions can be considered as stationary due to their large mass compared to the electrons. When there is no external electric field  $\mathbf{E}_0 = 0$  and letting  $f_0$  be Maxwellian, the linearised Vlasov equation for electrons is

$$\frac{\partial f_1}{\partial t} + \mathbf{v} \cdot \nabla f_1 - \frac{e}{m} \mathbf{E}_1 \cdot \frac{\partial f_0}{\partial \mathbf{v}} = 0. \quad (2.27)$$

Applying the Poisson's equation  $\varepsilon_0 \nabla \cdot \mathbf{E}_1 = - \int_{-\infty}^{\infty} f_1 d\mathbf{v}$  and employing the  $x$  direction plane wave expression for the perturbation  $f_1 \sim e^{i(kx - \omega t)}$ , we can derive the dispersion relation after integral over  $v_y$  and  $v_z$  as

$$1 = \frac{n_0 e^2}{\varepsilon_0 m k^2} \int_{-\infty}^{\infty} \frac{\partial \bar{f}_0(v_x)/\partial v_x}{v_x - (\omega/k)} dv_x. \quad (2.28)$$

Here,  $\bar{f}_0(v_x) = \left(\frac{m}{2\pi T}\right)^{3/2} e^{-mv_x^2/2T}$  is the normalised one-dimensional Maxwellian distribution. This result gives the frequency<sup>4</sup>  $\omega$  of an electron wave that propagates along the  $x$  direction. This wave is called the electron plasma wave or Langmuir wave. It is related to the electron oscillation in response to the perturbation, which is called the plasma

---

<sup>3</sup>However, MHD equations do not describe kinetic effects thus cannot capture micro-instabilities which are the main focus of this thesis; therefore, kinetic theory is needed for the following chapters.

<sup>4</sup>Usually the wave frequency is a complex number and its imaginary part identifies the growth rate of the wave.

oscillation and its frequency  $\omega_{pe}$  is

$$\omega_{pe} = \sqrt{\frac{n_0 e^2}{\epsilon_0 m}}. \quad (2.29)$$

Note that the integral of the dispersion equation (2.28) contains a singularity (resonant) thus it should be treated carefully. L. Landau was the first to correctly analyse this integral using contour integration [30, 33]. A rigorous calculation shows that the growth rate of this electron plasma wave is not zero, but is

$$\text{Im}(\omega) = -\sqrt{\pi} \omega_{pe} \left( \frac{\omega_{pe}}{k v_{th}} \right)^3 e^{-\frac{\omega_{pe}^2}{k^2 v_{th}^2} - \frac{3}{2}}. \quad (2.30)$$

It reveals a collisionless energy exchange mechanism between wave and resonant particles. This is called Landau damping. Although in this example the growth rate is negative, which means that the wave is stable, in later sections we will discuss other examples of unstable modes and our research focus.

## 2.2 Magnetic field geometries and coordinates

### 2.2.1 From magnetic mirror to tokamak

It is well-known that in a magnetic field the plasma spreads faster along the magnetic field lines than across them; in the parallel direction, the gradient of magnetic strength puts a force towards the weak field area. This informs the early design of the magnetic

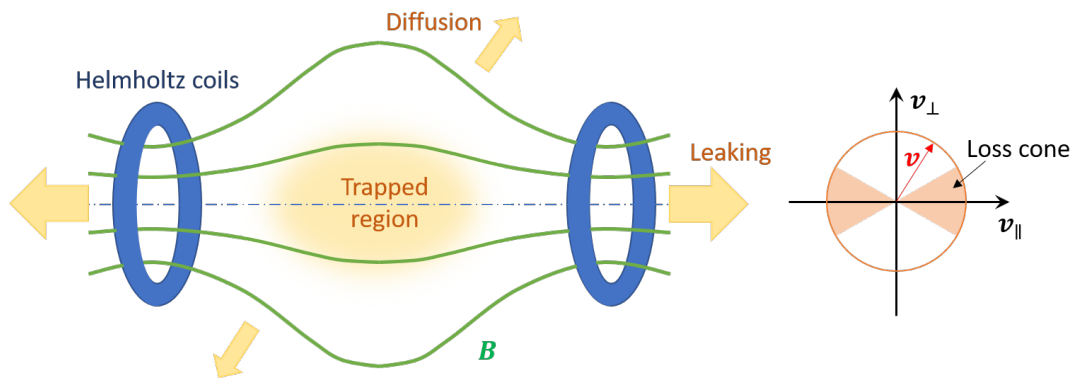


**Figure 2.3:** An illustration of the magnetic mirror concept (left) and the velocity loss cone (right). The plasma can be trapped around the central region where the magnetic strength is weak. However, the particles with a velocity in the loss cone will not be confined by this field and the leaking from the ends of the magnetic mirror design is significant.

mirror for confining plasma. Shown in figure (2.3) is the concept of the magnetic mirror created by a pair of Helmholtz coils. The magnetic field is strong near the coils but has a minimum in between. Due to the grad-B drift  $\mathbf{v}_{\nabla B}$  in equation (2.12), the plasma can be trapped near the central region. However, this confinement is not perfect. The collisions and instabilities can cause diffusion across the field line; but more importantly the leaking at the ends of the magnetic mirror is significant. The leaking portion can be shown using the adiabatic invariant  $\mu$  in equation (2.7) and the conservation of kinetic energy  $mv^2/2$ , with neglecting electric field. These two conserved quantities give a limitation in the pitch angle<sup>5</sup> of the trapped particles. Particles with the pitch angle

$$\frac{v_{\parallel}}{v_{\perp}} \geq \sqrt{\frac{B_{\max}}{B} - 1} \quad (2.31)$$

cannot be trapped by the magnetic mirror. Here  $B_{\max}$  is the maximum magnetic strength towards the Helmholtz coils and  $B$  is the magnetic strength at the particle's position where  $v_{\parallel}$  and  $v_{\perp}$  are measured. This pitch angle range is known as the loss cone in the velocity space in figure (2.3). Unless  $B_{\max} \rightarrow \infty$ , all particles will eventually enter the loss cone due to collisions and leak from the device. Considering the inefficiency of confinement as well as other instabilities [30], alternative confinement designs are needed.

Over the decades, fusion scientists have explored many other possible magnetic confinement configurations. Though a perfect magnetic trap does not exist, the most optimised concepts are the tokamak, stellarator and reversed-field pinch. Here we introduce the tokamak as the closest one to the research focus of this thesis.

The tokamak uses a toroidal magnetic field to eliminate the leaking ends of the magnetic mirror design. Figure (2.4) reproduced from [34] shows the layout of the magnetic fields and coils in the tokamaks. The toroidal field coils and central column generate a toroidal magnetic field that loops along the torus geometry. The Maxwell's equation  $\nabla \times \mathbf{B} = 0$  in cylindrical coordinates shows that the toroidal magnetic field is inversely proportional to the radius, so there is a strength gradient radially inwards. Ions and electrons therefore will drift apart due to the charge dependence in the curvature drift and the grad-B drift in equation (2.12). This is shown as  $\mathbf{v}_{R+\nabla B}$  in figure (2.5). The separation of charges establishes a vertical electric field which causes  $\mathbf{E} \times \mathbf{B}$  drift as the consequence. The  $\mathbf{E} \times \mathbf{B}$  drift is charge- and mass-independent and will eventually push the plasma off to the vessel wall and lose the confinement. To resolve this problem, in tokamaks a poloidal magnetic field  $B_{\theta}$  is generated by inducing a plasma current in the toroidal direction

---

<sup>5</sup>Pitch angle is defined as the cotangent of the angle between velocity and parallel direction, or the ratio of parallel velocity component to the perpendicular component.

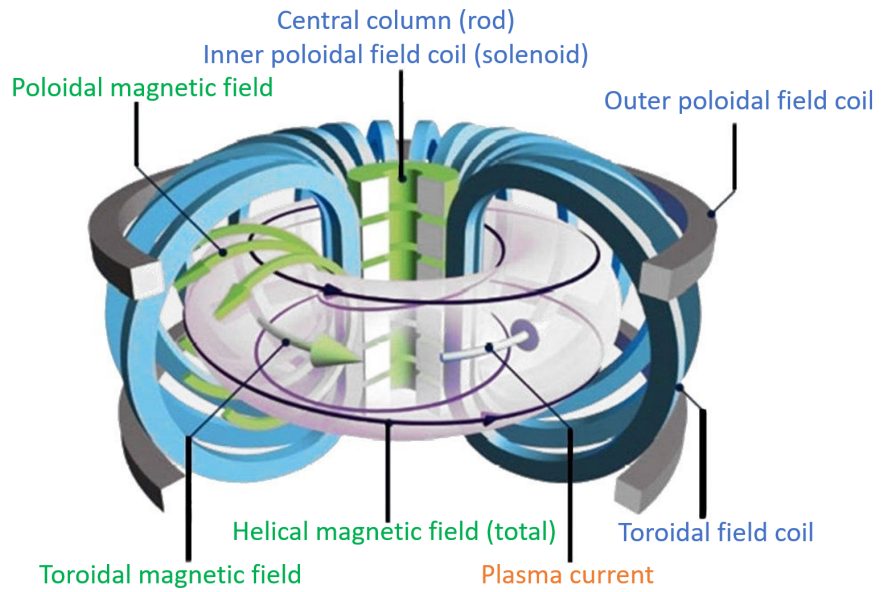


**Figure 2.4:** An illustration of the tokamak magnetic field lines and coils. Central column and toroidal field coils generate toroidal magnetic field; inner and outer poloidal field coils generate plasma current which produce poloidal magnetic field. The combination results in the helical magnetic field. Figure reproduced from [34].

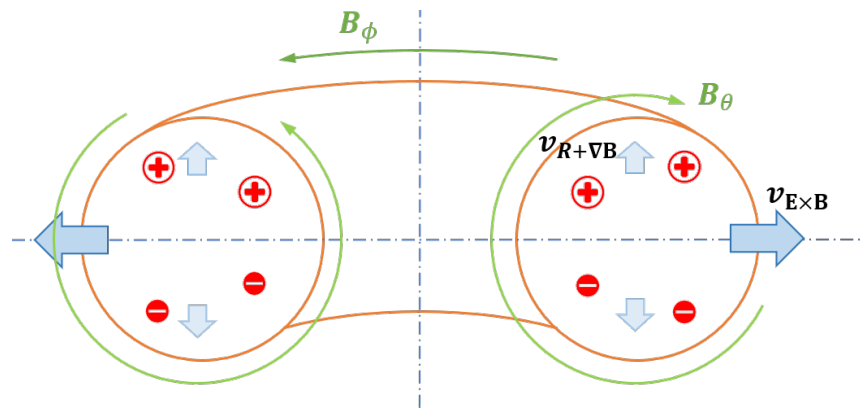


**Figure 2.5:** A sketch to explain the toroidal and poloidal magnetic fields in a tokamak. The toroidal magnetic field  $B_\phi$  causes the curvature drift and the grad-B drift  $v_{R+\nabla B}$  which separates charges. This establishes an electric field which brings in  $\mathbf{E} \times \mathbf{B}$  drift  $v_{\mathbf{E} \times \mathbf{B}}$ . A poloidal magnetic field  $B_\theta$  is required to average the charge separation to zero, and maintain the confinement.

using the solenoid. The resultant helical magnetic field lines loop between outward and inward, upside and downside of the chamber. This helical magnetic field is axisymmetric, in which particles will spend approximately same time at the inward side and the outward side while looping along the field lines. This offsets the charge separation noting the faster parallel velocity than the perpendicular drift velocity. As the result, plasma is confined

within the torus area.

As the poloidal magnetic field is important in retaining the confinement, its relative strength is a key factor related to the “safety” of the control. The safety factor  $q$  is defined as the slope of helical magnetic field with respect to toroidal direction  $\phi$  and poloidal direction  $\theta$ , averaged over a  $2\pi$  period in the poloidal plane

$$q = \frac{1}{2\pi} \oint \frac{d\phi}{d\theta} d\theta = \frac{1}{2\pi} \oint \frac{1}{R} \frac{B_\phi}{B_\theta} ds, \quad (2.32)$$

in which  $R$  is the major radius (see Section 2.2.2) and  $ds$  is the differential poloidal arc length. In other words,  $q$  is the number of times a field line migrates toroidally for each poloidal rotation. Note that as mentioned before, the tokamak confinement is not perfect. The instabilities that occur in the tokamaks affect the confinement. Generally speaking, a higher  $q$  value can put a limit on the instabilities therefore can benefit the stability [32].

In tokamaks, there exists a self-generated toroidal current caused by the diamagnetic drift and the momentum transfer between trapped particles and passing particles<sup>6</sup> [32, 35, 36, 37]. This current is called bootstrap current. It can contribute to a large portion of required poloidal magnetic field therefore can reduce the external induction expense [35, 38].

### 2.2.2 Flux surface coordinates

Equation (2.22) indicates that  $\mathbf{j} \cdot \nabla p = 0$  and  $\mathbf{B} \cdot \nabla p = 0$ , which means that in an equilibrium both magnetic field lines and current density lie in surfaces of constant pressure. Furthermore, the definition of  $q$  implies that  $q$  is also a function of the surface where magnetic field lines lie in, and the magnetic surfaces in a tokamak are nested about the toroidal axis (known as magnetic axis). In real (3D) machines, toroidal field ripple and other perturbations may mean that the field is not exactly axisymmetric in the toroidal direction. Nevertheless, it is convenient to introduce a coordinate that can reveal the insight of the magnetic geometry.

Considering  $\nabla \cdot \mathbf{B} = 0$  in a cylindrical coordinate system and the symmetry in toroidal angle, we have

$$\nabla \cdot \mathbf{B} = \frac{1}{R} \frac{\partial}{\partial R} (R B_R) + \frac{1}{R} \frac{\partial B_\phi}{\partial \phi} + \frac{\partial B_Z}{\partial Z} = 0, \quad (2.33)$$

---

<sup>6</sup>Following the helical field lines the magnetic strength varies between inward and outward, whose magnetic mirror effect traps a fraction of particles into a smaller orbit (known as banana orbit or potato orbit) - these particles are referred to as trapped particles; particles with a higher parallel velocity component are not trapped and can move through the toroidal trajectory - these are called passing particles.

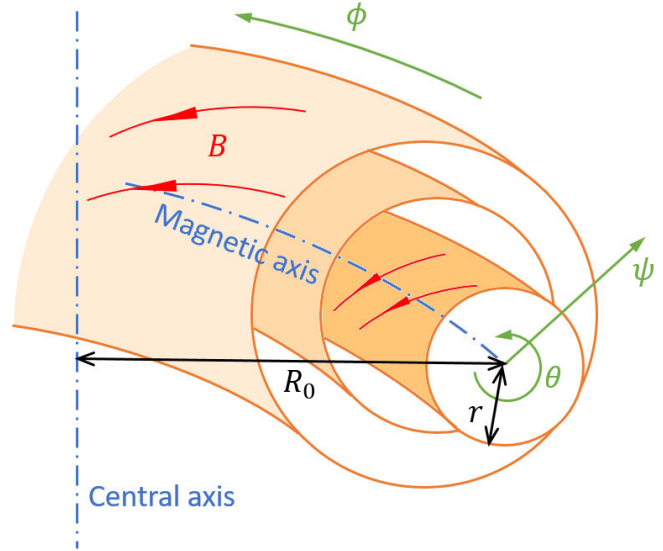


**Figure 2.6:** A sketch of the tokamak flux surface coordinates  $\{\psi, \theta, \phi\}$ . Three flux surfaces are coloured and the illustration of magnetic field lines on the flux surfaces are shown. The major radius  $R$ , minor radius  $r$  and magnetic axis are also labelled.

in which  $R$  is the radial direction in the cylindrical coordinate<sup>7</sup>. A poloidal flux function  $\psi$  is defined through

$$B_R = -\frac{1}{R} \frac{\partial \psi}{\partial Z}, \quad B_Z = \frac{1}{R} \frac{\partial \psi}{\partial R}, \quad (2.34)$$

which satisfies that

$$\mathbf{B} \cdot \nabla \psi = \frac{1}{R} \frac{\partial \psi}{\partial Z} \frac{\partial \psi}{\partial R} - \frac{1}{R} \frac{\partial \psi}{\partial R} \frac{\partial \psi}{\partial Z} = 0. \quad (2.35)$$

As a result, field lines lie in the surfaces of constant  $\psi$ , which are defined as flux surfaces. The plasma pressure and safety factor are therefore both functions of flux surfaces  $p = p(\psi)$ ,  $q = q(\psi)$ . And the plasma equilibrium can be solved by a differential equation for  $\psi$ . This equation, which we do not go into details in this thesis, is called the Grad-Shafranov equation [32, 39, 40]. A sketch of the flux surface coordinates  $\{\psi, \theta, \phi\}$  is shown in figure (2.6).

### 2.2.2.1 Mapping between toroidal and slab geometries

We shall be concerned with short wavelength instabilities in a tokamak plasma, which are then localised near a flux surface, or even locally to the vicinity of a field line - a flux tube. Sometimes it is helpful to consider toroidal annulus. Meanwhile, towards the

<sup>7</sup>The radial direction in the cylindrical coordinate is referred to as the major radius in the torus view; the radius in poloidal plane is referred to as the minor radius. Here, to avoid confusion we use  $\mathbf{R}$  for major radius direction and  $\mathbf{r}$  for minor radius direction. For a given tokamak device, the minor radius of the edge of the plasma is customarily noted as  $a$  while the major radius to the centre of the plasma is  $R_0$ . An inverse aspect ratio is defined as  $a/R_0$ .

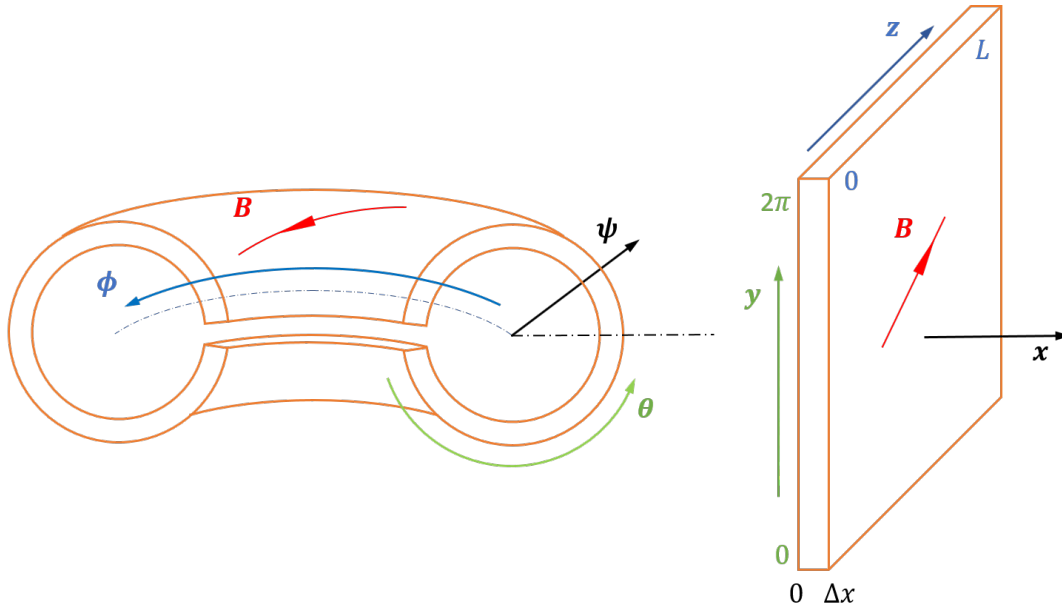


**Figure 2.7:** Illustration for mapping between toroidal geometry  $\{\psi, \theta, \phi\}$  (left) and slab geometry  $\{x, y, z\}$  (right). An example magnetic field line within  $\theta$ - $\phi$  flux surface and  $y$ - $z$  plane is also shown.

edge of a tokamak where the minor radius is large (ideally  $r \rightarrow \infty$ ) and the curvature is small, a reduced slab geometry can provide a simple approximation of the physics model when the main drive mechanism does not require curvature effects<sup>8</sup>. In this thesis, the instability to be studied is mainly driven by the electron temperature gradient, therefore we will predominantly use slab geometry.

The relation between the toroidal ring and the slab geometry<sup>9</sup> is shown in figure (2.7). The  $x$  direction in slab corresponds to radial direction  $\psi$  in toroidal geometry, which is considered as a thin layer; the  $y$  direction maps to poloidal direction  $\theta$  and is usually treated with periodic boundaries; the  $z$  direction relates to toroidal direction  $\phi$ . An example magnetic field line on  $\theta$ - $\phi$  flux surface is shown in the illustration, which lies in  $y$ - $z$  plane in the corresponding slab.

## 2.3 Transport and Micro-instabilities

A long plasma confinement time is the key goal in MCF, but it is limited by the diffusive losses caused by transport across flux surfaces. The confinement time can be estimated by

<sup>8</sup>Caution that in the complete tokamak model the curvature effects can be important. Some modes or instabilities can be localised only in the outward region where the curvature vector and the pressure gradient are parallel (bad curvature region), for example, interchange instability [41] and ballooning modes [42].

<sup>9</sup>The mapping relation shown here is the most simple and straightforward one. Another common choice maps the magnetic direction ( $\mathbf{b}$ ) to  $z$  direction and the binormal direction (perpendicular to  $\mathbf{b}$ ) to  $y$  direction.

the size of a machine and the transport rate towards the wall. In early theory and practice, the transport rate is predicted using classical diffusion equations (for example, Fick's second law [43]) with the complex modelling of trapped and passing particles, effective collision frequency, and impurities [30, 32, 44, 45, 46]. These studies are referred to as neoclassical estimates. However, experiments observe that the actual transport rate is much higher than the neoclassical estimates, especially for electrons [47, 48, 49]. This extra transport is called anomalous transport. Studies have revealed that the source of the anomalous transport is likely related with small scale fluctuations and instabilities driven by gradients in the plasma [50, 51, 52, 53]. In this thesis, we do not discuss more details of neoclassical calculations for the transport, but focus on the physics of two types of micro-instabilities that are driven by the electron temperature gradient.

### 2.3.1 Temperature gradient modes

Electron temperature gradient (ETG) modes and ion temperature gradient (ITG) modes are electrostatic instabilities<sup>10</sup> driven by electron or ion temperature gradient, respectively. In toroidal geometry, they occur due to the temperature-dependent drift velocity variation in the plasma. Figure (2.8) illustrates the fundamental mechanism of these instabilities in an equivalent slab cross section. In a magnetised plasma where a perpendicular magnetic drift exists, for example, the grad-B drift<sup>11</sup>, when a temperature gradient also exists, the magnetic drift velocity is faster for higher temperature. Along a perturbed contour of the temperature profile, the drift velocity variation leads to charge separation which creates the perturbed electric fields as shown in the figure. The electric fields cause  $\mathbf{E} \times \mathbf{B}$  drift which will modify the original perturbation. If the temperature gradient is parallel to the magnetic gradient, this ends up in a positive feedback so that the instability grows. On the contrary, if the direction of gradients are anti-parallel, the perturbation is suppressed. In tokamaks, these instabilities can happen in the bad curvature region.

The physics of ETG and ITG modes have been widely studied [54, 55, 56, 57, 58, 59, 60]. Usually these instabilities are believed to cause rippling of the equilibrium magnetic flux surfaces. Measuring along the  $x$  direction, on two sides of this flux surface, the parallel component of the fluctuating magnetic vector potential<sup>12</sup> is an odd function, while the electrostatic potential<sup>13</sup> is an even function. Such a parity characteristic is defined as the

<sup>10</sup>The magnetic fluctuations are not essential for electrostatic instabilities, therefore the modes can exist at  $\beta = 0$ . Though electromagnetic effects are still important especially at high  $\beta$ .

<sup>11</sup>In a slab geometry where the grad-B drift does not exist, the mechanism of the temperature gradient modes is actually more complicated. The parallel flow causes a density variation along the perturbed field lines, which gives rise to the instability [54]. Analytic calculations are presented in later chapters.

<sup>12</sup>The magnetic vector potential  $\mathbf{A}$  is defined through  $\mathbf{B} = \nabla \times \mathbf{A}$ .

<sup>13</sup>The electrostatic potential  $\phi$  is defined through  $\mathbf{E} = -\nabla\phi - \partial\mathbf{A}/\partial t$ .

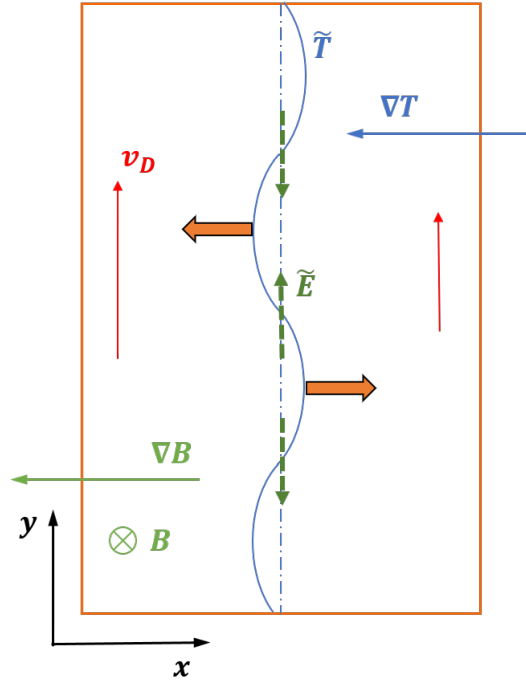


**Figure 2.8:** Illustration of the mechanism for temperature gradient modes. The cartoon shows the  $x$ - $y$  cross section in the equivalent slab coordinates for toroidal geometry. The magnetic field is along the  $z$  direction. A magnetic strength gradient  $\nabla B$  and temperature gradient  $\nabla T$  is set as parallel to the  $x$  direction. The drift velocity direction is shown as the electron species for an example. The dash-dotted line is unperturbed temperature contour while the curled line illustrates for a perturbation of the equilibrium temperature profile.

twisting parity, in which the converse parity characteristic can be seen through the spatial derivative in the definition of electrostatic potential. Another type of parity, tearing parity, is to be introduced in the next section. The parity (or parity mixture) of a mode gives a boundary condition for solving the eigenmode equations for an instability, and leads to specific physics impacts. Detailed discussions can be found in later chapters.

### 2.3.2 Microtearing modes

The microtearing mode (MTM), on the contrary, is a tearing parity micro-instability driven by the electron temperature gradient - the component of magnetic vector potential parallel to  $B$  is an even function about the flux surface while the electrostatic potential is odd. Note that in tokamak geometry, the safety factor  $q$  of this perturbed flux surface is required to be a rational number, where one field line re-joins with itself and forms an enclosed period. Such a flux surface is named a rational surface. In rational surfaces, the

field lines are easier to bend compared with in irrational surfaces [32]. Therefore, in the vicinity of rational surfaces when a shearing perturbation<sup>14</sup> happens, the field lines are able to reconnect to another field line which forms a magnetic island structure. The magnetic island structure is characterised by a set of nested magnetic flux surfaces appearing in the vicinity of the original rational surface position. This phenomenon is also referred to as magnetic reconnection. The size of magnetic islands are characterised by toroidal and poloidal wavenumbers, which are assumed large for MTMs.

Figure (2.9) shows the fundamental mechanism of MTM instability in the slab cross section. On the rational surface denoted with a dash-dotted line, a current density  $j_z$  along the  $z$  direction causes the sheared magnetic field  $B_y$  along  $\pm y$  directions. With finite inertia or resistivity, the sheared magnetic field can reconnect into a chain of magnetic islands in the nearby region. When a temperature gradient  $\nabla T$  exists, the width of magnetic islands may grow which leads to the growth of the instability. The labels for O-point and X-point are shown.

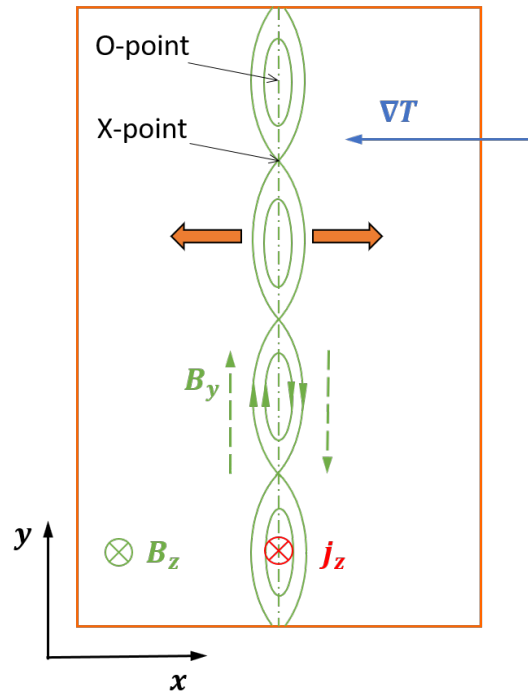


**Figure 2.9:** Illustration of the mechanism for microtearing modes. The cartoon shows the  $x$ - $y$  cross section in the equivalent slab coordinates for toroidal geometry. The magnetic field  $B_z$  is along the  $z$  direction. A current density  $j_z$  at the rational surface (the dash-dotted line) causes the sheared magnetic field  $B_y$  in  $\pm y$  directions. The reconnection of the sheared magnetic field lines form a chain of magnetic islands in the nearby region. When a temperature gradient  $\nabla T$  exists, the width of magnetic islands may grow which leads to the growth of the instability. The labels for O-point and X-point are shown.

<sup>14</sup>The shearing perturbation means that the perturbation has opposite directions across the perturbed surface, for example,  $\pm B_y$  in figure (2.9).

islands, which lowers the magnetic energy state [61]. At the point where reconnection occurs, the flux surface cross into a singularity topology. This crossing place is named the “X-point”, while the middle place in a magnetic island is named the “O-point”. When a temperature gradient  $\nabla T$  exists, a similar mechanism to figure (2.8) can apply to the magnetic island surfaces, thus the width of magnetic islands may grow. This results in the growth of the instability. Figure (2.10) reproduced from [62] shows an example of the existence of MTMs in a tokamak simulation.

Once a magnetic island forms, the inward and outward sides of the island becomes the same flux surface. This allows an increasing particle and heat transport across the radial direction and may result in significant energy loss in tokamak plasmas [65]. Although the rate of the transport can be affected by many reasons and sometimes can be hard to estimate, MTMs have been studied extensively and are believed to be a candidate for anomalous electron thermal transport in tokamaks [66, 67, 68], where they can cause loss of confinement towards the edge pedestal region where the pressure gradient is high and the rational surfaces are close to each other [64, 69]. In the earliest studies in the simple slab geometry by R. D. Hazeltine et. al [70], J. F. Drake et. al [61] and N. T. Gladd et. al [63], the detailed mechanism driven by the electron temperature gradient is shown to closely rely on the collision process, which is energy-dependent. Their work shows that MTMs are stable at both low and high collision frequencies, and are unstable at only semi-collisional conditions. However, recently, many different toroidal gyrokinetic simulations

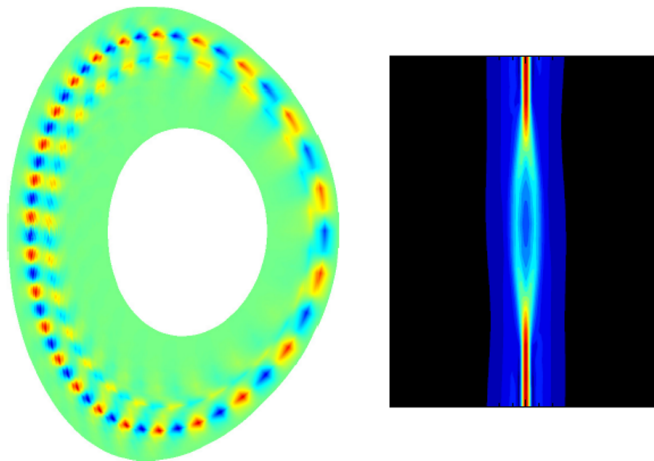


**Figure 2.10:** Structure of MTMs in a tokamak simulation. Figure reproduced from [62]. The left figure shows the contour of perturbed magnetic vector potential near two rational surfaces in the poloidal cross section; the right figure shows the contour of a typical current layer for the magnetic island crossing the radial direction.

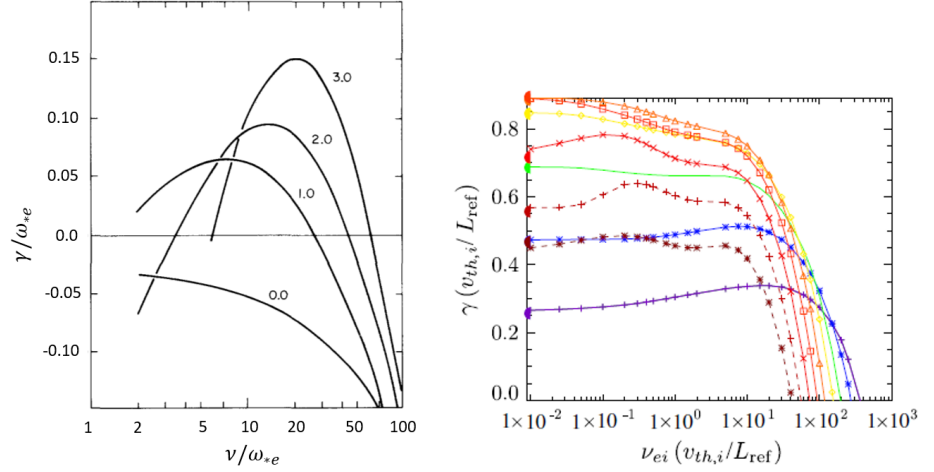


**Figure 2.11:** Comparison of slab and toroidal MTM results in the literature. The left figure is reproduced from [63] for slab geometry (the layout of the slab geometry will be introduced in figure (3.1)), in which four curves with different electron temperature gradients are shown; the right figure is reproduced from [64] for toroidal geometry, in which the curves have different binormal wavenumbers. Although the two figures are calculated with different parameters, both show the growth rate as a function of collision frequency.

have found a micro-scale tearing parity instability, which is believed to be a MTM, with the collision operator that neglects the energy dependence or even in the collisionless limit [64, 71, 72, 73]. Figure (2.11) shows the growth rate as a function of collision frequency in slab geometry [63] and toroidal geometry [64]. These toroidal and slab results are at odds at low collision frequency. Studies [64, 71, 74, 75] have explored a couple of possible effects of the toroidal geometry but the full drive mechanism is not yet understood. As modern MCF reactors are designed to operate at higher temperature where the collision frequency is low, comprehending the drive mechanism for the collisionless MTM is vital for identifying the impact on transport.

The following sections of this thesis focus on the physics of this collisionless micro-scale tearing parity mode. In Section 3.4.1 we review the gyrokinetic MTM theory in [61, 63, 70] in the slab geometry; in Section 4.1.1 we correct some mistakes in [63]; in Section 4.2.1 we demonstrate the existence of a collisionless MTM in GS2 simulations even in the slab geometry; in Section 4.3 and Section 4.5 we probe the physics behind this novel instability; in Chapter 5 we develop analytic models; and in Chapter 6 we benchmark our models with simulations.



# Chapter 3

## Gyrokinetic theory

The kinetic theory in Section 2.1.2 is a six dimensional system which in principle can describe the evolution with various spatial and temporal scales, but on the other hand, it can be expensive to solve. In many situations where the frequency of the interesting physics process is much smaller than the rapid gyrofrequency, it is possible to provide a simplified tractable analysis by averaging over the gyroangle. This approach is called the gyrokinetic theory. It results in a five dimensional system<sup>1</sup> for the gyroaveraged distribution function, which can be considered as a distribution function of charged rings.

The validation for the time scale separation assumption is important. This is called the gyrokinetic ordering though the specific form can vary with the physics problems. In the following sections, we will outline the general key ideas of gyrokinetic theory then apply the theory to MTMs in slab geometry as one example<sup>2</sup>; at the end we will introduce the gyrokinetic simulation codes.

### 3.1 Guiding centre coordinates

As the gyrokinetic theory exploits the rapid gyromotion feature, it is convenient to choose the coordinates based on the guiding centre. We recall the illustration shown previously in figure (2.2) to demonstrate the guiding centre coordinates. The particle's position is  $\mathbf{x} = \mathbf{r} + \boldsymbol{\rho}_L = \mathbf{r} + \mathbf{b} \times \mathbf{v}_\perp / \omega_c$ , in which  $\mathbf{r}$  is the position of the guiding centre and the positive or negative sign of charge  $q$  in  $\omega_c$  is required. The velocity can be composed as  $\mathbf{v} = \mathbf{v}_\parallel + \mathbf{v}_\perp = v_\parallel \mathbf{b} + v_\perp (\mathbf{e}_1 \sin \alpha - \mathbf{e}_2 \cos \alpha) = \mathbf{v}(v_\parallel, v_\perp, \alpha)$ , in which  $\alpha$  is the

---

<sup>1</sup>Under some special circumstances where there is also a fast periodic motion along the magnetic field lines, a further averaging can be conducted and the system can be reduced to four dimensional [32].

<sup>2</sup>The discussion in these sections are based from [40, 53, 76, 77, 78, 79].

gyrophase angle of the gyration, with respect to a set of orthogonal basis  $\{\mathbf{e}_1, \mathbf{e}_2\}$  on the perpendicular plane; the basis vectors  $\{\mathbf{e}_1, \mathbf{e}_2, \mathbf{b}\}$  are right-handed. Considering the guiding centre's drift equation (2.12), it may be more convenient to express the velocity in a phase space of  $(\varepsilon, \mu, \alpha)$ <sup>3</sup>, in which  $\varepsilon = v^2/2$  and  $\mu = v_\perp^2/2B$  are kinetic energy per unit mass and magnetic moment per unit mass, respectively. In this adopted coordinate system,

$$\nabla_{\mathbf{v}} = \mathbf{v} \frac{\partial}{\partial \varepsilon} + \frac{\mathbf{v}_\perp}{B} \frac{\partial}{\partial \mu} + \frac{\mathbf{b} \times \mathbf{v}_\perp}{v_\perp^2} \frac{\partial}{\partial \alpha}. \quad (3.1)$$

From here we drop the subscript  $s$  for species. Note that here  $\mathbf{b}$  includes the fluctuating magnetic field contribution. Using equations (3.1) and (2.12), the Vlasov equation (2.16) becomes

$$\frac{\partial f}{\partial t} + (\mathbf{v}_\parallel + \mathbf{v}_D) \cdot \frac{\partial f}{\partial \mathbf{r}} - \omega_c \frac{\partial f}{\partial \alpha} + \frac{q}{m} \mathbf{E} \cdot \left( \mathbf{v} \frac{\partial}{\partial \varepsilon} + \frac{\mathbf{v}_\perp}{B} \frac{\partial}{\partial \mu} + \frac{\mathbf{b} \times \mathbf{v}_\perp}{v_\perp^2} \frac{\partial}{\partial \alpha} \right) f = 0. \quad (3.2)$$

## 3.2 Gyrokinetic ordering

Firstly, we consider  $-i\partial/\partial t = \omega \ll \omega_c$  and  $L \gg \rho_L$ , in which  $\omega$  represents a characteristic frequency associated with plasma fluctuations and  $L$  is the characteristic length of a physics parameter, for example, for density gradient  $L_n^{-1} = -(\nabla n)/n = -\nabla \ln n$  and for temperature gradient  $L_T^{-1} = -(\nabla T)/T = -\nabla \ln T$ . Note that the spatial and temporal scales are linked via the thermal velocity, thus the two inequalities have the same order of magnitude, noting

$$\frac{\omega}{\omega_c} \sim \frac{\rho_L}{L} \sim \delta \ll 1. \quad (3.3)$$

Secondly, we assume a small perturbation on the physics quantities, for example, the distribution function  $f$ . The linearised expansion up to the first order can be written as

$$f = f_0 + \epsilon f_1 + \mathcal{O}(\epsilon^2), \quad (3.4)$$

in which  $f_0$  is the equilibrium (or slow variation) term,  $f_1 \sim e^{i(\mathbf{k} \cdot \mathbf{r} - \omega t)}$  is the perturbation (or fast variation) term and the long-wavelength corrections to the equilibrium, and  $\epsilon \ll 1$  denotes the order of the perturbation. Note that although the magnitude of perturbations is small, the gradient of perturbations can be comparable with the gradient in the equilibrium terms. This allows sharp variation in perturbations. Meanwhile, for plasma instabilities with wavelengths comparable to gyroradius, it is useful to assume  $\epsilon \sim \delta$  [40]<sup>4</sup>. This

---

<sup>3</sup>Note that the dimensions in this expression have changed and the direction of velocity is ambiguous. Another coordinate variable  $\iota = \mathbf{v}_\parallel/|\mathbf{v}_\parallel|$  defining the velocity direction should be introduced if necessary.

<sup>4</sup>For studying equilibrium, transport processes or other instabilities, a drift-kinetic ordering  $\epsilon \ll \delta$  [40, 53] is more often used.

can be expressed as  $\nabla f_0 \sim f_0/L$  and  $\nabla f_1 \sim f_1/\rho_L$ . Using  $\nabla_\perp$  and  $\nabla_\parallel$  to represent the gradient operator in the perpendicular and parallel directions, we can link the two as  $\nabla_\perp \sim k_\perp \sim 1/L_\perp \sim 1/\rho_L$  and  $\nabla_\parallel \sim k_\parallel \sim 1/L_\parallel \sim 1/L$ . Therefore, the orderings can be summarised as

$$\frac{\omega}{\omega_c} \sim \frac{\rho_L}{L} \sim \frac{k_\parallel}{k_\perp} \sim \frac{L_\perp}{L_\parallel} \sim \frac{f_1}{f_0} \sim \delta \ll 1. \quad (3.5)$$

We can now evaluate the ordering for each term in equation (3.2) and separate the equations of each order as

$$\delta^{-1} \text{ order : } -\omega_c \frac{\partial f_0}{\partial \alpha} = 0, \quad (3.6)$$

$$\delta^0 \text{ order : } \mathbf{v}_\parallel \cdot \frac{\partial f_0}{\partial \mathbf{r}} - \frac{q}{mB} \mathbf{E} \cdot \mathbf{v}_\perp \frac{\partial f_0}{\partial \mu} - \omega_c \frac{\partial f_1}{\partial \alpha} = 0, \quad (3.7)$$

$$\delta^1 \text{ order : } \frac{\partial f_1}{\partial t} + \mathbf{v}_\parallel \cdot \frac{\partial f_1}{\partial \mathbf{r}} + \mathbf{v}_D \cdot \nabla (f_0 + f_1) - \omega_c \frac{\partial f_2}{\partial \alpha} + \frac{q}{m} \mathbf{E} \cdot \left( \mathbf{v} \frac{\partial f_0}{\partial \varepsilon} + \frac{\mathbf{v}_\perp}{B} \frac{\partial f_1}{\partial \mu} + \frac{\mathbf{b} \times \mathbf{v}_\perp}{v_\perp^2} \frac{\partial f_1}{\partial \alpha} \right) = 0. \quad (3.8)$$

### 3.3 Gyrophase averaging

The leading order equation (3.6) informs us that  $f_0$  is independent of  $\alpha$ . Gyroaveraging over the  $\delta^1$  order eliminates  $f_2$  term and gives the non-trivial gyrokinetic equation for  $f_0$ . The gyroaveraging operation is represented by  $\langle \dots \rangle = \frac{1}{2\pi} \int_0^{2\pi} \dots d\alpha$ . Assuming the perturbation can be separated into gyrophase independent and dependent parts as  $f_1 = \bar{f}_1 + \tilde{f}_1$ , the gyroaveraged equation can be written as

$$\begin{aligned} \frac{\partial \bar{f}_1}{\partial t} + \mathbf{v}_\parallel \cdot \frac{\partial \bar{f}_1}{\partial \mathbf{r}} + \langle \mathbf{v}_D \rangle \cdot \nabla (f_0 + \bar{f}_1) + \langle \mathbf{v}_D \cdot \nabla \tilde{f}_1 \rangle + \frac{q}{m} \langle \mathbf{E} \cdot \mathbf{v} \rangle \frac{\partial f_0}{\partial \varepsilon} \\ + \frac{q}{mB} \langle \mathbf{E} \cdot \mathbf{v}_\perp \rangle \frac{\partial \bar{f}_1}{\partial \mu} + \frac{q}{mB} \langle \mathbf{E} \cdot \mathbf{v}_\perp \frac{\partial \tilde{f}_1}{\partial \mu} \rangle + \frac{q}{mv_\perp^2} \langle \mathbf{E} \cdot \mathbf{b} \times \mathbf{v}_\perp \frac{\partial \tilde{f}_1}{\partial \alpha} \rangle = 0. \end{aligned} \quad (3.9)$$

Note that  $\mathbf{E} = -\nabla\phi - \partial\mathbf{A}/\partial t$ , in which  $\phi$  is the electric potential and  $\mathbf{A}$  is the magnetic vector potential. Expanding the expression around the guiding centre  $\mathbf{x} - \rho_L$  and using  $\partial\rho_L/\partial\alpha = \mathbf{v}_\perp/\omega_c$  give  $\mathbf{E} \cdot \mathbf{v}_\perp \sim -i\omega_c \partial(\phi - vA)/\partial\alpha$ . Further proceeding with a large amount of algebra, the gyrokinetic equation can be eventually derived as

$$\begin{aligned} \left[ \frac{\partial}{\partial t} + (\mathbf{v}_\parallel + \mathbf{v}_D) \cdot \nabla \right] g = \left[ \frac{q}{m} \frac{\partial f_0}{\partial \varepsilon} \frac{\partial}{\partial t} - \frac{\nabla(f_0 + g) \cdot \mathbf{b} \times \nabla}{B} \right] \\ \left[ (\phi - v_\parallel A_\parallel) J_0(k_\perp \rho_L) + \frac{v_\perp B_\parallel}{k_\perp} J_1(k_\perp \rho_L) \right], \end{aligned} \quad (3.10)$$

in which  $g$  is the gyroaveraged distribution perturbation and  $J_0(k_\perp \rho_L)$  and  $J_1(k_\perp \rho_L)$  are the zeroth and first order Bessel functions of the first kind

$$J_n(x) = \frac{(-i)^n}{\pi} \int_0^\pi e^{ix \cos \alpha} \cos(n\alpha) d\alpha, \quad x, \alpha \in \mathcal{R} \text{ and } n \in \mathcal{N}. \quad (3.11)$$

This is in agreement with equation (2.11.3) in [32].

#### 3.3.1 Finite Larmor radius effects

The Bessel functions in the gyrokinetic equation (3.10) arise from the gyroaveraging. Usually the fluctuating electromagnetic fields vary around the guiding centre. One common assumption for the rapid variation of perturbations is in the eikonal form of  $\propto e^{i\mathbf{k}_\perp \cdot \boldsymbol{\rho}_L}$ . Then the gyrophase averaging gives (see Appendix A.2)

$$\langle e^{i\mathbf{k}_\perp \cdot \boldsymbol{\rho}_L} \rangle = J_0(k_\perp \rho_L), \quad (3.12)$$

$$\langle \boldsymbol{\rho}_L e^{i\mathbf{k}_\perp \cdot \boldsymbol{\rho}_L} \rangle = i\rho_L J_1(k_\perp \rho_L) \frac{\mathbf{k}_\perp}{k_\perp}, \quad (3.13)$$

$$\langle \mathbf{v}_\perp e^{i\mathbf{k}_\perp \cdot \boldsymbol{\rho}_L} \rangle = iv_\perp J_1(k_\perp \rho_L) \frac{\mathbf{k}_\perp \times \mathbf{b}}{k_\perp}. \quad (3.14)$$

This is named the finite Larmor radius (FLR) effects. Because  $J_0(0) = 1$  and  $J_1(0) = 0$ , FLR effects are often neglected when  $\rho_L$  is small compared with the field variation scale length, for example, for electrons.

#### 3.3.2 Nonlinear effects

The  $\nabla g \cdot \mathbf{b} \times \nabla$  term on the right hand side of equation (3.10) contains the nonlinear interactions which can provide quantitative information on amplitude saturation. It is important for calculating heat or particle transport, though it does not typically affect the basic physics drive mechanism contained in linear theories. Dropping this term gives the linear gyrokinetic equation. In this thesis, we focus only on the linear physics. The nonlinear interaction is to be investigated in the future work.

#### 3.3.3 Collision operator

The gyrokinetic equation (3.10) does not include a collision term. A gyroaveraged collision operator can be implemented to the left hand side of the equation. However, the explicit gyroaveraged form of the full Fokker-Planck collision operator can be very complicated [32]. In a simple model considering the small pitch angle scattering between

electrons and ions<sup>5</sup>, a good approximation can be obtained with the pitch angle scattering Lorentz collision operator [80]

$$C_L(\nu) = \frac{\nu}{2} \frac{\partial}{\partial \xi} (1 - \xi^2) \frac{\partial}{\partial \xi}, \quad (3.15)$$

in which  $\nu$  is the velocity-dependent collision frequency and  $\xi = v_{\parallel}/v$ . In the simple pitch angle scattering model, the collision frequency can be estimated as  $\nu \approx (nq^4)/(16\pi\epsilon_0^2 m^2 v^3)$ . The spread of particle speeds  $v$  is described via a distribution  $f(v)$ . However, the collision frequency of a system can be characterised by its value at the thermal velocity  $\nu_{th} = \nu(v_{th})$ , so that  $\nu = \nu_{th} \cdot (v/v_{th})^{-3}$ .

Note that actually this form of Lorentz collision operator does not consider the conservation of momentum nor the change of gyrophase angle [80, 81, 82]. Typically, these are higher order corrections, so the expression presented here is widely adopted in analytic work. Nevertheless, in certain circumstances the deviation cannot be neglected; therefore, in the full gyrokinetic calculations, a correction term is added to this operator to account for their effect [82, 83] (see Section 4.4).

## 3.4 Applications of gyrokinetic theory

### 3.4.1 MTMs in the slab geometry

We demonstrate the derivation of the linear slab MTM model in [61, 63, 70] from gyrokinetic theory as one example of the application. We consider an infinite slab layer of plasma as illustrated in figure (3.1) in an external magnetic field  $B_z = B_0$ . A current density  $j_z$  is applied along the  $z$  direction, which generates a sheared magnetic field  $B_y$ . In this slab the total magnetic field can be expressed by  $\mathbf{B} = B_0(\mathbf{1}_z + (x/L_s)\mathbf{1}_y)$ , in which  $L_s$  represents the magnetic shearing scale length. We consider  $|B_y| \ll |B_z|$  and  $x \ll L_s$ . Two species, hydrogen ions and electrons, are included, each carrying one elementary charge  $q = \pm e$ . A density gradient  $\nabla n$  and a temperature gradient  $\nabla T$  are applied and their scale lengths are  $L_n$  and  $L_T$ , respectively. The normalised temperature gradient is defined as  $\eta = L_n/L_T$ .

The nature of the MTM arises from the sheared magnetic field coupling with the electrons, so that the parallel field dynamic  $B_{\parallel}$  and the ion collision are non-essential. Further assumptions in the linear slab MTM model of [61, 63, 70] include that the grad-B and

---

<sup>5</sup>From the centre of mass frame it can be seen that the collisions between the same particle species have little impact on the system; the interesting physics is associated with collisions between unlike particles [30].

curvature perpendicular drift  $v_D$  for both species is zero; the ion parallel perturbation dynamics  $v_{\parallel} \cdot \nabla g_i$  is neglected considering the electron parallel streaming is much faster, which determines the frequency of the mode; the density gradient  $L_n$  is the same for both species; the ion and electron temperatures are equal in the middle of slab,  $T_i = T_e = T$ , but the ion temperature gradient  $\eta_i$  is zero while allowing a finite electron temperature gradient  $\eta_e$ ; and the mode wavenumber in the  $x$  direction is smaller than that of the  $y$  direction,  $k_x < k_y$ , which brings the authors' attention to an elongated mode. Applying the collisionless gyrokinetic equation (3.10) to ions, dropping the nonlinear term and the parallel perturbation term, and assuming the equilibrium distribution function is Maxwellian  $f_0 = f_M$  yield

$$g_i = -\frac{f_M}{\omega} \left( \frac{e}{T} \omega - \frac{\nabla n k_{\perp}}{n B} \right) J_0(k_{\perp} \rho_i) (\phi - v_{\parallel} A_{\parallel}), \quad (3.16)$$

in which  $k_{\perp} = \sqrt{k_x^2 + k_y^2}$  and  $\rho_i$  is ion gyroradius. A diamagnetic frequency  $\omega_*$  can be defined through the diamagnetic drift equation (2.21) as<sup>6</sup>

$$\omega_{*s} = \frac{k_y T_s}{q_s B} \frac{\nabla n_s}{n_s} = \mp \frac{k_y v_s \rho_s}{2L_n}, \quad (3.17)$$

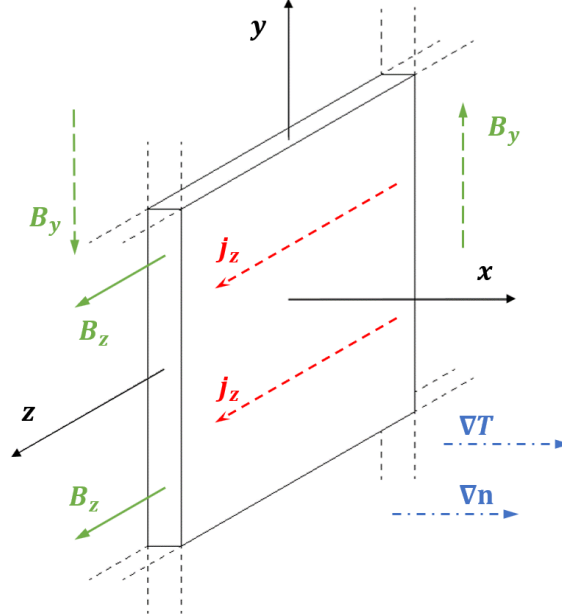


**Figure 3.1:** The illustration for the slab geometry for the MTM derivation. The magnetic field  $B_z$  and  $B_y$ , the current density  $j_z$ , the density gradient  $\nabla n$  and the temperature gradient  $\nabla T$  are shown in the figure.

<sup>6</sup>Note the factor “2” in the denominator. In [63] there is a typographical error in defining the diamagnetic frequency (see Section 4.1.1).

in which  $v_s$  represents the thermal velocity of species  $s$ . The last  $\mp$  sign is used to denote the (ion or electron) direction<sup>7</sup> of the frequency, thus  $\omega_{*i}/\omega_{*e} = -1$  holds in this model.

The ion density  $n_i$  is given by

$$\begin{aligned}
 n_i &= n_0 \frac{e\phi}{T} + \int_{-\infty}^{\infty} d^3\mathbf{v} \cdot g_i J_0(k_{\perp}\rho_i) \\
 &= n_0 \frac{e}{T} \left[ 1 - \frac{2}{v_i^3 \sqrt{\pi}} \left( 1 - \frac{\omega_{*i}}{\omega} \right) \int_{-\infty}^{\infty} dv_{\parallel} \int_0^{\infty} v_{\perp} dv_{\perp} \cdot e^{-(v_{\parallel}^2 + v_{\perp}^2)/v_i^2} J_0^2\left(\frac{k_{\perp}v_{\perp}}{\omega_{ci}}\right) \right] \phi \\
 &= n_0 \frac{e}{T} \left[ 1 - \left( 1 - \frac{\omega_{*i}}{\omega} \right) \left( \Gamma_0\left(\frac{k_y^2 v_i^2}{2\omega_{ci}^2}\right) - \frac{v_i^2}{2\omega_{ci}^2} \Gamma_0'\left(\frac{k_y^2 v_i^2}{2\omega_{ci}^2}\right) \frac{\partial^2}{\partial x^2} \right) \right] \phi,
 \end{aligned} \tag{3.18}$$

in which  $\Gamma_0(z) = e^{-z} I_0(z) = e^{-z} J_0(iz)$  with  $I_0(z)$  being the modified Bessel function. Here, the integration on  $A_{\parallel}$  becomes zero due to the odd function with respect to  $v_{\parallel}$ ; equation (6.615) of [84] and equation (9.6.27) of [85] are used in the calculation.

For electrons, considering the Lorentz collision operator (3.15) and ignoring the FLR effects, the gyrokinetic equation (3.10) becomes

$$\left[ \omega - k_{\parallel} v_{\parallel} - \frac{i\nu}{2} \frac{\partial}{\partial \xi} (1 - \xi^2) \frac{\partial}{\partial \xi} \right] g_e = \frac{e}{T} f_M (\omega - \omega_{*e}^T) (\phi - v_{\parallel} A_{\parallel}), \tag{3.19}$$

in which  $k_{\parallel} = k_y x / L_s$  and  $\omega_{*e}^T = \omega_{*e} [1 + \eta_e (\frac{v^2}{v_e^2} - \frac{3}{2})]$ . The Legendre polynomial series can be adopted to expand  $g_e$  as  $g_e(x, v, \xi) = \sum_{n=0}^{\infty} h_n(x, v) P_n(\xi)$ , where

$$P_n(\xi) = \frac{1}{2^n n!} \frac{d^n}{d\xi^n} (\xi^2 - 1)^n, \quad \xi \in \mathcal{R} \text{ and } n \in \mathcal{N}, \tag{3.20}$$

so that

$$v_{\parallel} P_n = v \xi P_n = v \frac{(n+1)P_{n+1} + nP_{n-1}}{2n+1}, \tag{3.21}$$

$$\frac{\partial}{\partial \xi} (1 - \xi^2) \frac{\partial}{\partial \xi} P_n = -n(n+1)P_n. \tag{3.22}$$

<sup>7</sup>Customarily, the electron direction  $\omega_{*e}$  is chosen positive.

Equation (3.19) results in

$$\begin{aligned} \sum_{n=0}^{\infty} h_n \left[ \left( \omega + \frac{i\nu}{2} n(n+1) \right) P_n - k_{\parallel} v \frac{(n+1)P_{n+1} + nP_{n-1}}{2n+1} \right] \\ = \frac{e}{T} f_M (\omega - \omega_{*e}^T) (\phi - v\xi A_{\parallel}). \end{aligned} \quad (3.23)$$

Multiplying equation (3.23) with  $P_m$  ( $m \in \mathcal{N}$ ) then applying the orthogonality relation of Legendre polynomials in integrating over  $\xi$  from  $-1$  to  $1$

$$\int_{-1}^1 P_n(\xi) P_m(\xi) d\xi = \begin{cases} 2/(2m+1), & \text{for } m = n, \\ 0, & \text{for } m \neq n \end{cases} \quad (3.24)$$

give a set of recurrence relations on  $h_m$

$$m = 0 : \quad \omega h_0 - \frac{k_{\parallel} v}{3} h_1 = \frac{e f_M}{T} (\omega - \omega_{*e}^T) \phi, \quad (3.25)$$

$$m = 1 : \quad (\omega + i\nu) h_1 - k_{\parallel} v \left( h_0 + \frac{2}{5} h_2 \right) = -\frac{e f_M}{T} (\omega - \omega_{*e}^T) v A_{\parallel}, \quad (3.26)$$

$$m \geq 2 : \quad \left[ \omega + \frac{i\nu}{2} m(m+1) \right] h_m - k_{\parallel} v \left[ \frac{m}{2m-1} h_{m-1} + \frac{m+1}{2m+3} h_{m+1} \right] = 0. \quad (3.27)$$

After some algebra, equation (3.27) derives a continued fraction for the ratio defined as

$$\begin{aligned} \alpha_m &= \frac{m}{(2m-1)} \frac{k_{\parallel} v}{[\omega + i\nu m(m+1)/2]} \frac{h_{m-1}}{h_m} \\ &= 1 - \frac{k_{\parallel}^2 v^2 (m+1)^2}{(2m+1)(2m+3)} \left[ \left( \omega + \frac{i\nu}{2} (m+1)(m+2) \right) \left( \omega + \frac{i\nu}{2} m(m+1) \right) \alpha_{m+1} \right]^{-1} \end{aligned} \quad (3.28)$$

with  $\alpha_m \rightarrow 1$  as  $m \rightarrow \infty$ . This continued fraction gives the implicit solution on the series of  $h_m$ .

Equations (3.25) and (3.26) give the parallel electric field

$$E_{\parallel} = i\omega A_{\parallel} - ik_{\parallel} \phi = i \frac{T}{e} \frac{[\omega(\omega + i\nu) \alpha_1 - k_{\parallel}^2 v^2 / 3]}{v f_M (\omega - \omega_{*e}^T)} h_1. \quad (3.29)$$

Substituting equation (3.28), the parallel current density

$$\begin{aligned}
 j_{\parallel} &= \sigma_{\parallel} E_{\parallel} = -e \int_{-\infty}^{\infty} d^3\mathbf{v} \cdot g_e v_{\parallel} \\
 &= -2\pi e \int_0^{\infty} v^2 dv \cdot v \sum_{n=0}^{\infty} h_n \int_{-1}^1 P_1 P_n d\xi \\
 &= -\frac{4\pi e}{3} \int_0^{\infty} v^3 h_1 dv
 \end{aligned} \tag{3.30}$$

gives the parallel electron conductivity  $\sigma_{\parallel}$  as

$$\begin{aligned}
 \sigma_{\parallel} &= -\frac{4\pi e}{3} \int_0^{\infty} \frac{v^3 h_1}{E_{\parallel}} dv \\
 &= \frac{4i}{3\sqrt{\pi}} \frac{n_0 e^2}{v_e^3 T} \int_0^{\infty} \frac{\omega - \omega_{*e}^T}{\omega(\omega + i\nu) \alpha_1 - k_{\parallel}^2 v^2 / 3} e^{-v^2/v_e^2} v^4 dv \\
 &= \frac{8i}{3\sqrt{\pi}} \varepsilon_0 \omega_{pe}^2 \int_0^{\infty} \frac{\omega - \omega_{*e}^T}{\omega(\omega + i\nu) \alpha_1 - k_{\parallel}^2 v_e^2 u^2 / 3} e^{-u^2} u^4 du,
 \end{aligned} \tag{3.31}$$

in which  $u = v/v_e$ . The electron density  $n_e$  is given by

$$\begin{aligned}
 n_e &= -n_0 \frac{e\phi}{T} + \int_{-\infty}^{\infty} d^3\mathbf{v} \cdot g_e \\
 &= -n_0 \frac{e\phi}{T} + 4\pi \int_0^{\infty} v^2 h_0 dv \\
 &= -n_0 \frac{e\phi}{T} + 4\pi \int_0^{\infty} v^2 \left[ \frac{e\phi}{T} f_M \left[ 1 - \frac{\omega_{*e}}{\omega} \left( 1 + \eta_e \left( \frac{v^2}{v_e^2} - \frac{3}{2} \right) \right) \right] + \frac{k_{\parallel} v}{3\omega} h_1 \right] dv \\
 &= -n_0 \frac{e\phi}{T} \frac{\omega_{*e}}{\omega} - \frac{k_{\parallel} \sigma_{\parallel}}{e\omega} E_{\parallel}.
 \end{aligned} \tag{3.32}$$

Therefore, the quasi-neutrality  $n_i = n_e$  eventually derives

$$\frac{\beta}{v_i^2} (\omega + \omega_{*e}) \left[ \frac{2\omega_{ci}^2}{v_i^2} \left( \Gamma_0 \left( \frac{k_y^2 v_i^2}{2\omega_{ci}^2} \right) - 1 \right) - \Gamma_0' \left( \frac{k_y^2 v_i^2}{2\omega_{ci}^2} \right) \frac{\partial^2}{\partial x^2} \right] \phi = k_{\parallel} \mu_0 \sigma_{\parallel} E_{\parallel}, \tag{3.33}$$

in which  $\beta$  is the plasma beta defined in equation (2.24). Another equation to close this system is the Maxwell's equation  $-\nabla^2 \mathbf{A} = \mu_0 \mathbf{j}$  in the parallel direction

$$\left( \frac{\partial^2}{\partial x^2} - k_y^2 \right) A_{\parallel} = \mu_0 \sigma_{\parallel} E_{\parallel}. \tag{3.34}$$

In conclusion, equations (3.34), (3.33), (3.31) and (3.28) give the set of eigenmode equa-

tions for the slab MTM model, with  $\omega$  being the eigenvalue. These equations agree<sup>8</sup> with equations (2), (3), (7) and (8) summarised in [63]. The spatially localised tearing parity boundary condition is adopted when calculating the eigenmode equations

$$|\phi|, |A_{\parallel}| \rightarrow 0 \text{ as } |x| \rightarrow \infty, \quad \phi(0) = 0, \quad \left. \frac{\partial A_{\parallel}}{\partial x} \right|_{x=0} = 0. \quad (3.35)$$

### 3.4.2 Gyrokinetic simulation programmes

Usually a realistic physics system can be too complex to derive or solve the analytic eigenmode equations. Simplification under certain assumptions can sometimes miss out important physics factors while its applicability is limited. Although the analytic solutions are useful for demonstrating the underlying physics mechanism and instability characteristics, advanced numerical iterative methods are more and more often adopted in research, especially with the help of the rapidly developing high-performance supercomputers. The computational simulation approaches can provide assistance in studying experimental data, exploring possible drive mechanisms and estimating transport impact.

In general, a simulation code should consider the following characteristics of a gyrokinetic system and for each characteristic it should provide options to control the physics accounted in the calculation.

1. Electrostatic or electromagnetic field. This implies the nature of the instability.
2. Adiabatic or kinetic particle species. This indicates the source of the instability.
3. Linear or nonlinear gyrokinetic equations. Linear solution can identify the key physics while nonlinear coupling between different eigenmodes is important for quantitative transport calculation.
4. Local or global spatial domain. If the scale length of the instability is much smaller than that of the equilibrium profile variation, a localised approximation can be adopted to reduce the calculation cost.

The most widely used gyrokinetic simulation codes in MCF research include GS2 [86], GENE [87], GEM [88], GKW [89] and GYRO [90]. Each code adopts different algorithms when solving the gyrokinetic equations, which makes it possible to benchmark with each other to provide confidence in drawing conclusions. A complete topical review on different approaches in gyrokinetic simulation codes can be found in [91]; a verific-

---

<sup>8</sup>The sign definition differences for charge  $\pm e$  and diamagnetic frequency  $\omega_*$  between our demonstration and [63] leads to the  $-E_{\parallel}$  and  $\omega_{*i}$  expression in the reference. The  $\beta$  definition in [63] is twice as ours. Besides, another typographical error in the reference is dropping the coefficient “2” in the  $2(\Gamma_0 - 1)$  term.

ation between GS2, GEM and GYRO focusing on micro-instabilities can be found in [92].

In this thesis, we employ GS2 to benchmark the numerical solutions of analytic models. GS2 solves the gyrokinetic equations with an implicit initial value and eigenvalue solving algorithm as described in [93, 94, 95]. It is developed with full electromagnetic physics effects and particles in a general local flux tube domain, with both linear and nonlinear options. The simulation results presented in this thesis are calculated with the linear simulation option by the version v8.0.1 [96].



# Chapter 4

## The limitation of the classic slab MTM model

### 4.1 Numerical approach for solving simultaneous eigenmode equations

The eigenmode equations (3.33) and (3.34) are a set of second order differential equations in which the electromagnetic fields  $\phi$  and  $A_{\parallel}$  are coupled. The analytic solution can be difficult to find, thus a numerical approach is needed. The eigenvalue of  $\omega$  relies on both equations, thus we implement an iterative algorithm<sup>1</sup> that can update  $\phi$  and  $A_{\parallel}$  simultaneously as  $\omega$  is adjusted towards self-consistency. This method is outlined as follows.

First we discretise the derivatives into a finite difference representation following

$$\left. \frac{\partial f(x)}{\partial x} \right|_{x=x_i} = \frac{f_{i+1} - f_{i-1}}{2h}, \quad (4.1)$$

$$\left. \frac{\partial^2 f(x)}{\partial x^2} \right|_{x=x_i} = \frac{f_{i+1} - 2f_i + f_{i-1}}{h^2}, \quad (4.2)$$

where  $f_i$  represents the value of  $f(x_i)$  and  $x_i$  is on a uniform discrete space with the grid spacing  $h$ . Here, the discretisation rule applies to both  $\phi$  and  $A_{\parallel}$  and we define a new vector variable  $U$  as

$$U_i = \begin{pmatrix} A_{\parallel i} \\ \phi_i \end{pmatrix} \quad (4.3)$$

---

<sup>1</sup>This approach is modified based on that introduced in Section 5.4.1 of [53].

to combine the two equations together. In this way, equations (3.33) and (3.34) can be written as

$$\mathbf{P}_i \cdot \mathbf{U}_{i-1} + \mathbf{Q}_i \cdot \mathbf{U}_i + \mathbf{S}_i \cdot \mathbf{U}_{i+1} = 0, \quad (4.4)$$

in which  $\mathbf{P}_i$ ,  $\mathbf{Q}_i$  and  $\mathbf{S}_i$  are square  $2 \times 2$  matrices containing the coefficients for  $\phi$  and  $A_{\parallel}$  on adjacent grids  $x_{i-1}$ ,  $x_i$  and  $x_{i+1}$ . Note that these coefficients are functions of  $\omega$ , therefore the eigenvalue of  $\omega$  relates to the eigenvalue of the matrices and acts as the link between the adjacent grids. The boundary condition (3.35) can be written using the combined variable  $\mathbf{U}$  as

$$\mathbf{U}_{\infty} = \begin{pmatrix} 0 \\ 0 \end{pmatrix}, \quad \mathbf{U}_0 = \begin{pmatrix} A_{\parallel}(0) \\ 0 \end{pmatrix}, \quad \mathbf{U}_1 - \mathbf{U}_{-1} = \begin{pmatrix} 0 \\ \phi'(0) \end{pmatrix}. \quad (4.5)$$

To solve the equation we start with the ansatz

$$\mathbf{U}_{i-1} = \boldsymbol{\kappa}_{i-1} \cdot \mathbf{U}_i + \boldsymbol{\zeta}_{i-1}, \quad (4.6)$$

where  $\boldsymbol{\kappa}$  is a  $2 \times 2$  matrix and  $\boldsymbol{\zeta}$  is a  $2 \times 1$  column vector. The values of  $\boldsymbol{\kappa}$  and  $\boldsymbol{\zeta}$  are to be found at each grid point. Provided that  $\boldsymbol{\kappa}$  and  $\boldsymbol{\zeta}$  have been determined, starting from one boundary point they will give values of  $\mathbf{U}$  at all grid points. Substituting the generated set of  $\mathbf{U}$  into eigenmode equation (4.4) will find the eigenvalue of  $\omega$ . In practice, we first use a trial  $\omega$  to determine the trial  $\boldsymbol{\kappa}$  and  $\boldsymbol{\zeta}$ ; then use the trial  $\boldsymbol{\kappa}$  and  $\boldsymbol{\zeta}$  to iterate and update  $\omega$  until equation (4.4) is satisfied at the boundary.

To find the iteration relation, we substitute equation (4.6) into equation (4.4) and get

$$(\mathbf{P}_i \cdot \boldsymbol{\kappa}_{i-1} + \mathbf{Q}_i) \cdot \mathbf{U}_i = -\mathbf{S}_i \cdot \mathbf{U}_{i+1} - \mathbf{P}_i \cdot \boldsymbol{\zeta}_{i-1}. \quad (4.7)$$

Therefore,

$$\boldsymbol{\kappa}_i = -(\mathbf{P}_i \cdot \boldsymbol{\kappa}_{i-1} + \mathbf{Q}_i)^{-1} \cdot \mathbf{S}_i, \quad (4.8)$$

$$\boldsymbol{\zeta}_i = -(\mathbf{P}_i \cdot \boldsymbol{\kappa}_{i-1} + \mathbf{Q}_i)^{-1} \cdot (\mathbf{P}_i \cdot \boldsymbol{\zeta}_{i-1}). \quad (4.9)$$

The initial values for  $\boldsymbol{\kappa}_0$  and  $\boldsymbol{\zeta}_0$  at the centre of the grid are determined by the boundary conditions at the centre point. For example, the tearing parity condition (4.5) gives

$$\boldsymbol{\kappa}_0 = \begin{pmatrix} 0 & 0 \\ 0 & 0 \end{pmatrix}, \quad \boldsymbol{\zeta}_0 = \begin{pmatrix} A_{\parallel}(0) \\ 0 \end{pmatrix} \xrightarrow{\text{Normalising to}} \begin{pmatrix} 1 \\ 0 \end{pmatrix}. \quad (4.10)$$

The steps to update  $\omega$  can then be summarised as follows.

1. Determine  $P_i$ ,  $Q_i$  and  $S_i$  at all grid points  $i$  using the trial  $\omega$ ;
2. Calculate  $\kappa_i$  and  $\zeta_i$  from the grid centre  $i_0$  towards the edge  $i_{\max}$  using boundary conditions  $\kappa_0$ ,  $\zeta_0$  at the centre grid and iteration relations (4.8), (4.9);
3. Apply the boundary condition at the edge  $U_{\max}$  and use equation (4.6) step by step to get the field variables  $U_{-1}$ ,  $U_0$  and  $U_1$  at the centre grid;
4. Substitute  $P_0$ ,  $Q_0$ ,  $S_0$  and  $U_{-1}$ ,  $U_0$ ,  $U_1$  into the left hand side of the eigenmode equation (4.4), noting as  $L$ ; note that as the trial  $\omega$  may not be the correct eigenvalue,  $L \neq 0$ ;
5. Update  $\omega$  to make  $L \rightarrow 0$  and repeat from step 1 until  $|L| \leq \delta$  is reached, where  $\delta$  is the required numerical precision; the latest converged  $\omega$  is one of the eigenvalues for equation (4.4).

There are different methods to update  $\omega$  in the last step, of which the most common and well-known choice is the Newton–Raphson method. However, note that one eigenmode equation may have multiple eigenvalues; this algorithm might not be able to find all of them. Usually both methods rely on the initial guess and the function smoothness around one eigenvalue, and may have “preferred” or “non-preferred” converged solutions among all eigenvalues. When all eigenvalues are required, a variant of this approach traverses through a range of  $\omega$  and applies each  $\omega$  value to only steps 1 to 4 but records the value of  $L$  for each initial  $\omega$ . A contour plot for  $L = 0$  then gives all possible eigenvalues of  $\omega$  within the tested range.

With regard to numerical precision, the grid size  $i_{\max}$  is determined by both eigenmode equation and the programme floating point precision. Usually a physics system has the vanishing boundary condition where  $U_{\infty} \rightarrow 0$ . The calculation in step 3 is at risk of truncation error accumulation. In practice, an extra level of iteration can be designed to monitor the precision.

In general, this method can also be applied to more complicated systems where  $m$  simultaneous equations and variables exist. In such a case,  $P$ ,  $Q$ ,  $S$  and  $\kappa$  are  $m \times m$  matrices. Sometimes  $U$  and  $\zeta$  are also treated as  $m \times m$  matrices, where each column represents independent solutions based on different settings of boundary condition.

We develop a numerical programme code in Fortran 90 based on the above algorithm. The numerical results for the slab MTM model in this thesis is solved by this code. In this code, to calculate the parallel conductivity  $\sigma_{\parallel}$  in equation (3.31), a numerical complex integration is modified from a recursive adaptive numerical quadrature method described

in Section 18.8 of [97]. Note that the integration in equation (3.31) may contain a residue if  $\gamma \sim -\nu/2$ , where  $\gamma$  is the growth rate of the mode (imaginary part of eigenmode frequency  $\omega$ ) and  $\nu$  is the collision frequency. This requires a careful treatment in the code.

Compared with modern full gyrokinetic simulation codes, our eigenvalue solver code calculates within the set of eigenmode equations that has been derived, in which the gyrokinetic mode is reduced and only the essential physics is kept. This stands as an independent verification against full gyrokinetic simulation codes to help reveal the insight physics of one problem. Meanwhile, due to the reduced system size, our numerical code is faster than the equivalent calculation in full gyrokinetic simulation codes.

### 4.1.1 Benchmark with previous results

We can reproduce the numerical results presented in [63] using our algorithm above, correcting some mistakes we have identified in the reference. In figure (4.1) we display the comparisons with figure (1) and figure (4) from [63] as the key results. These two graphs present the normalised mode growth rate  $\gamma/\omega_{*e}$  and the normalised mode frequency  $\omega_r/\omega_{*e}$  as functions of the normalised collision frequency  $\nu_{th}/\omega_{*e}$  at the electron temperature gradient  $\eta_e = 0.0, 1.0, 2.0$  and  $3.0$ , respectively.

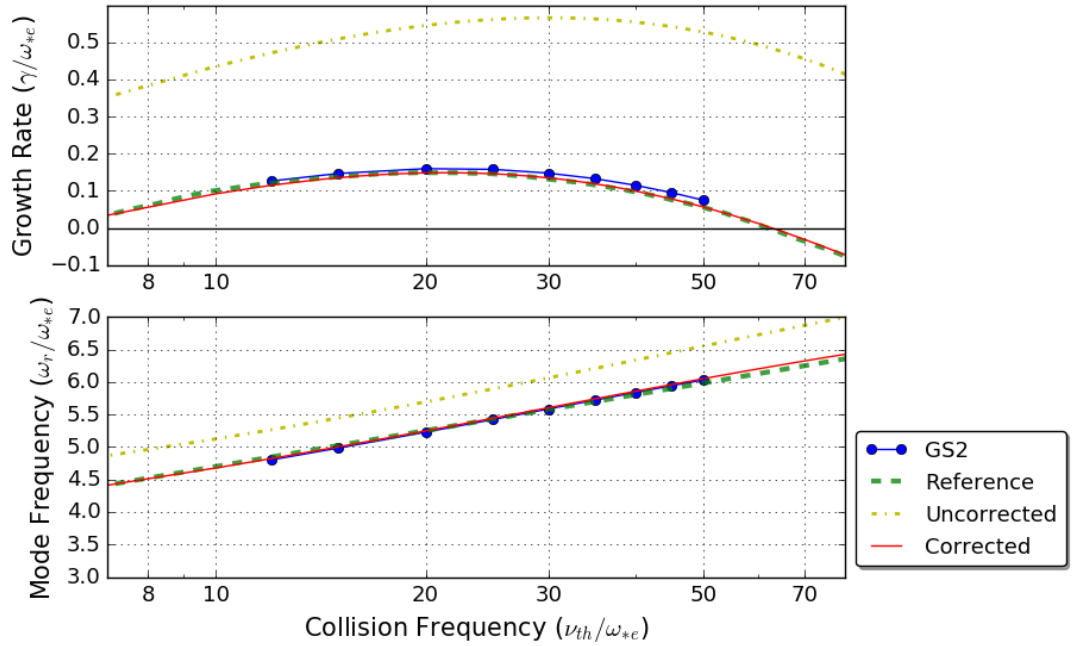
First we notice that there are several typographical errors in [63] when setting the parameters. Some conflict between context and captions, for example,  $k_y\rho_i$  is said to be 0.05 in the captions of figure (1) and figure (4) but is 0.1 in the context of figure (4). Actually, the data in figure (1) match with points at  $k_y\rho_i = 0.1$  in figure (2) and figure (5). There are also other errors in other graphs, for example, the data in figure (3) are 10 times smaller than they should be. After detailed cross check with all other results presented in this reference and benchmark against GS2 simulations, we find that the corrected parameters for figure (1) and figure (4) should be  $k_y\rho_i = 0.1$ ,  $\beta = 0.01$  in the reference's definition ( $\beta = 0.005$  in our definition) and  $L_n/L_s = 0.05$ .

Figure (4.1) presents the comparison and correction to the numerical results in the reference. Both the results presented in the reference and calculated from the correct eigenmode equations (with  $\omega_{*e}$  definition presented in Section 3.4.1) agree with GS2 results. However, the results calculated from the equations published in the reference show a significant deviation compared to procedures. As we have mentioned in Section 3.4.1, we now once again confirm with GS2 that in the reference paper there are missing factors of “2” in the denominator of  $\omega_{*e}$  and in the coefficient for  $2(\Gamma_0 - 1)$  term, although the numerical calculation results presented in the reference are correct; both our derived ei-

genmode equations and numerical algorithm are correct. In the following sections of this thesis, the slab MTM model results are calculated with the corrected eigenmode equations (3.34), (3.33), (3.31) and (3.28), with  $\omega_{*e}$  definition in (3.17) and  $\beta$  definition in (2.24).

## 4.2 Benchmark slab MTMs with GS2

Numerical results of the simplified analytic MTM model in equations (3.33) and (3.34) match well with full gyrokinetic simulation GS2 results in the collisional regime. Shown in figure (4.2) is the mode frequency and growth rate as functions of collision frequency, in which the mode frequency  $\omega_r$  is the real part of the eigenmode  $\omega$  while the growth rate  $\gamma$  is the imaginary part. The parameters are set in a similar range to those in [63], in which a relatively strongly magnetised ( $\beta = 0.005$ ) hydrogen plasma ( $m_i/m_e = 1836$ ) is adopted;  $k_y = 0.3$ ,  $\eta_e = 5.0$  and  $L_n/L_s = 0.05$  are set as the datum case. Both eigenmode



**Figure 4.1:** Comparison of the numerical results in the reference slab model. The blue lines with circles are GS2 simulation results; the green dashed lines are results presented in figure (1) and figure (4) of [63]; the yellow dash-dotted lines are calculated from the eigenmode equations defined in equations (2), (3), (7), (8) of [63] together with the definition of  $\omega_{*e}$  defined there; the red lines are calculated with the corrected eigenmode equations provided in this thesis (3.34), (3.33), (3.31), (3.28) and  $\omega_{*e}$  definition (3.17). The abscissa is in the log scale. The physics parameters are  $k_y \rho_i = 0.1$ ,  $\eta_e = 3.0$ ,  $\beta = 0.005$  (in our definition) and  $L_n/L_s = 0.05$ .

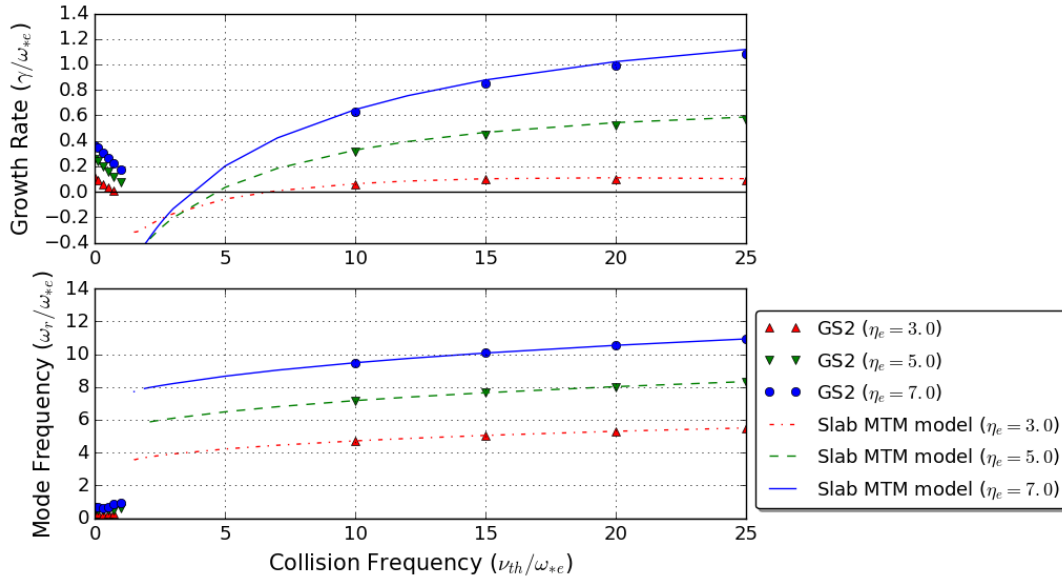


**Figure 4.2:** The benchmark of eigenmode, comparing analytically reduced slab MTM model and full gyrokinetic simulation GS2 as a function of collision frequency. The physics parameters are  $k_y \rho_i = 0.3$ ,  $\beta = 0.005$  and  $L_n/L_s = 0.05$ . Three electron temperature gradients  $\eta_e = 3.0$ ,  $5.0$  and  $7.0$  are shown with red, green, blue colours.

and collision frequencies are normalised to electron diamagnetic frequency  $\omega_{*e}$ . The lines in the graph are numerical results from the slab MTM model, while the symbols are linear GS2 simulation results. The simulations are set to calculate the most unstable (with the largest  $\gamma$ ) tearing parity eigenmode<sup>2</sup>. The GS2 geometry is set as the *s-alpha* option with *const-curve* and *epsl* = 0, which is equivalent to the slab geometry illustrated in figure (3.1); the collision option in GS2 is set to the Lorentz model<sup>3</sup> including only electron-ion collisions; a kinetic species model for both ions and electrons is adopted in GS2; and the parallel magnetic field perturbation is turned off to align with our physics model. Additional numerical parameters for GS2 are *nperiod* = 16, *ntheta* = 4 and *delt* = 0.2 for collision frequency  $\nu_{th}/\omega_{*e} \geq 10$  whilst *nperiod* = 128, *ntheta* = 8 and *delt* = 0.05 for  $\nu_{th}/\omega_{*e} < 10$ ; for both cases, *negridd* = 8, *ngauss* = 16, *shat* = 1 and *fprim* = 1. The convergence of these numerical parameters will be discussed in Section 4.2.2.

A higher  $\eta_e$  value corresponds to a large electron temperature gradient. Both analytically reduced model and GS2 confirm that the MTM can be driven unstable by the electron

<sup>2</sup>Here the GS2 is compiled to the initial value solver mode and in the input parameters the *ginit\_option* is set as *default\_odd*. Another option to compile GS2 is to use the eigenvalue solver, which calculates a series of possible eigenmodes. That option will be used in Section 6.1.3 to investigate the harmonic series.

<sup>3</sup>Note that the GS2 Lorentz model differs from the Lorentz collision operator in equation (3.15); this will be discussed in Section 4.4.

temperature gradient at moderately collisional conditions. However, GS2 reveals a tearing parity instability at the low collision frequency range where the mode is found to be stable in the slab MTM model. Note that this is in a slab geometry, thus such a result is quite unexpected. This implies that the conventional slab MTM model might not be complete, requiring an extra drive mechanism for the collisionless MTM. Therefore, it is priority to understand the drive mechanism of this collisionless mode in the slab geometry, which may in turn shed light on the physics mechanisms of collisionless MTMs in toroidal geometry.

### 4.2.1 The slab collisionless unstable branch

We investigate the slab collisionless unstable branch in GS2 simulations. This collisionless branch shown in figure (4.2) is also driven more unstable by the electron temperature gradient. However, note that the mode frequency of the collisionless branch is discontinuous with the collisional one, which indicates that these two branches are not the same

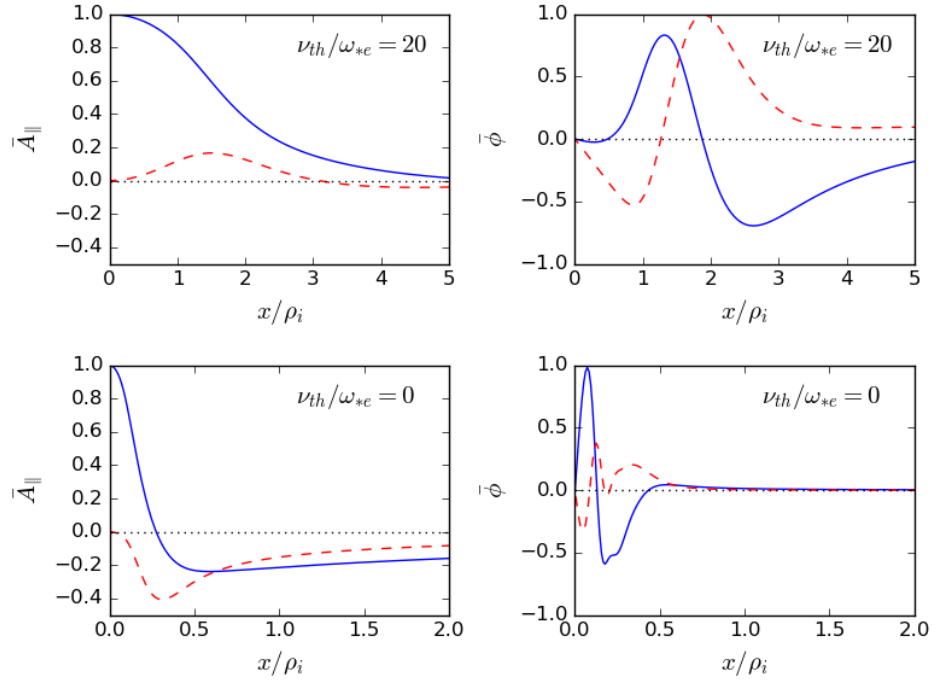


**Figure 4.3:** The mode structures in normalised perturbed electrostatic potential  $\bar{\phi}$  and parallel magnetic vector potential  $\bar{A}_{\parallel}$  for collisional (top panels,  $\nu_{th}/\omega_{*e} = 20$ ) and collisionless (bottom panels,  $\nu_{th}/\omega_{*e} = 0$ ) instability branches in GS2 simulations. The real and imaginary parts of the fields are shown with blue solid lines and red dashed lines, respectively. The collisional branch is shown with the  $\nu_{th}/\omega_{*e} = 20$  and  $\eta_e = 5.0$  data point in figure (4.3); the collisionless branch is shown with  $\nu_{th}/\omega_{*e} = 0$  and  $\eta_e = 5.0$ .

eigenmode.

Figure (4.3) shows the comparison for the mode structure in perturbed electrostatic potential  $\phi$  and parallel magnetic vector potential  $A_{\parallel}$  between the two branches in GS2 simulations. The original output of GS2 is in Fourier space along the field line, but here the data have been transformed into real space for convenience. In this and later figures about mode structures, the plotted range is zoomed to the centre of the slab; the simulation range is much larger where the fields smoothly decay to approximately zero at larger  $x$  values. The potentials are normalised such that  $\bar{A}_{\parallel}|_{x/\rho_i=0} = 1$  and  $\max(|\bar{\phi}|) = 1$ . It is clear that for both branches, the perturbed parallel magnetic vector potential  $A_{\parallel}$  has an even symmetry across the slab while the electrostatic potential  $\phi$  is odd. The integral of  $A_{\parallel}$  across the slab is non-zero, which leads to the “wandering” of the magnetic field and forms the magnetic island (see Section 6.2). The parity characteristic demonstrates that both branches are a tearing parity mode. One may suspect the collisionless unstable branch to be another tearing parity eigenmode solution. However, using the traverse contour code with the slab MTM equations, we do not find any eigenvalue near the GS2 result, as is shown in figure (4.4). Note that importantly the mode width shown in figure (4.3) for the collisionless branch is much smaller than the collisional one. This narrow

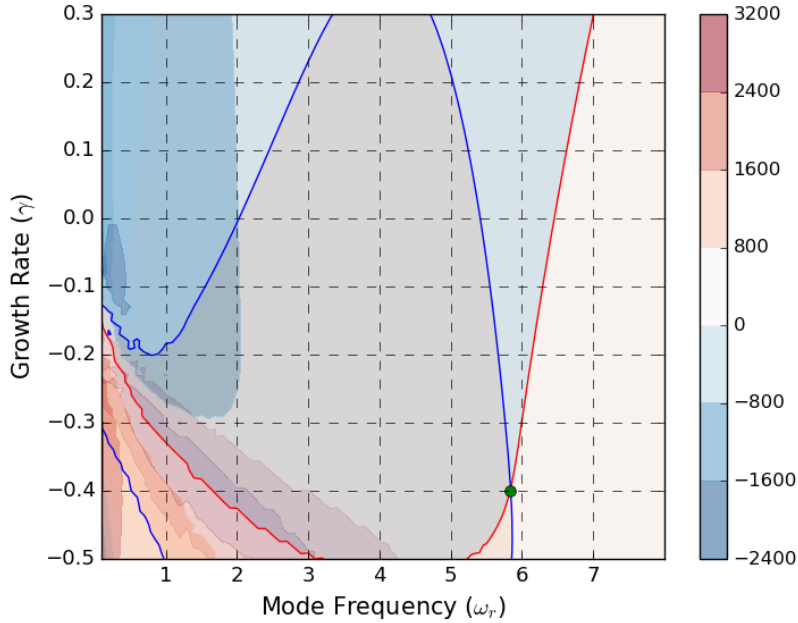


**Figure 4.4:** The contour plot showing the eigenvalues of  $\omega$  calculated from the slab model at  $\eta_e = 5.0$ ,  $\nu_{th}/\omega_{*e} = 2.0$  of figure (4.2). The blue and red curves are real and imaginary parts, respectively, for contours of  $L = 0$  as described in Section 4.1, whilst the colour illustrates the relative value of  $L$ . The green dot denotes the only eigenvalue of this model within the shown  $\omega$  range.

radial structures relate to extended structures along the field line. In other words, the characteristic radial wavenumber  $k_x$  is much larger in the collisionless branch than in the collisional one. We will further investigate this point in Section 4.3.2.

## 4.2.2 Convergence verification for simulation data

It is worth noting here the convergence of GS2 data. As the radial wavenumber  $k_x$  is so large for the collisionless branch, GS2 simulations indeed require sufficient grid extent and resolution to capture this unstable mode accurately. The simulation in GS2 is conducted in a local flux tube domain. The extent of the flux tube is controlled by a numerical parameter  $nperiod$ , such that the number of  $2\pi$  segments along the field line is  $2nperiod - 1$ . Another numerical parameter,  $ntheta$ , defines the grid resolution within each segments. Both high  $nperiod$  and  $ntheta$  is needed to resolve the collisionless branch, otherwise the simulation result can be wrong and sometimes the mode may even appear stable. Figure (4.5) shows an example of the convergence verification results regarding the GS2 numerical parameter  $ntheta$  in the collisionless branch. The sufficient grid extent and resolution requirement can be explained by the vanishing boundary condition. If grid extent is not consistent with the wavenumber requirement, the edge of the mode in the simulation is forced to zero, which gives either a non-physical oscillating field or an inaccurate field, which thus interferes with the accuracy of the eigenmode frequency.

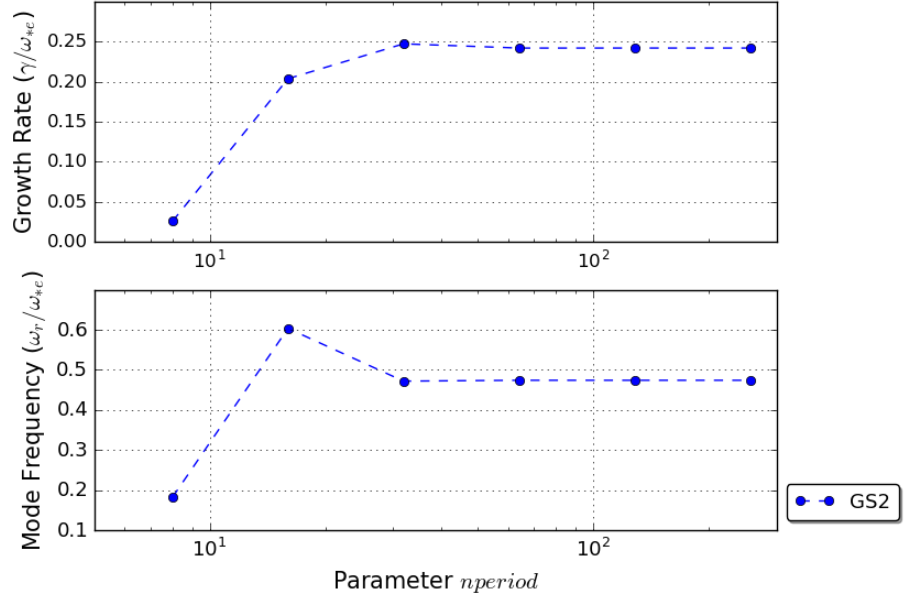


**Figure 4.5:** The convergence verification on mode growth rate and frequency for the GS2 numerical parameter  $ntheta$  in the collisionless branch. The physics parameters are  $k_y\rho_i = 0.3$ ,  $\eta_e = 5.0$ ,  $\beta = 0.005$ ,  $L_n/L_s = 0.5$  and  $\nu_{th}/\omega_{*e} = 0$ .

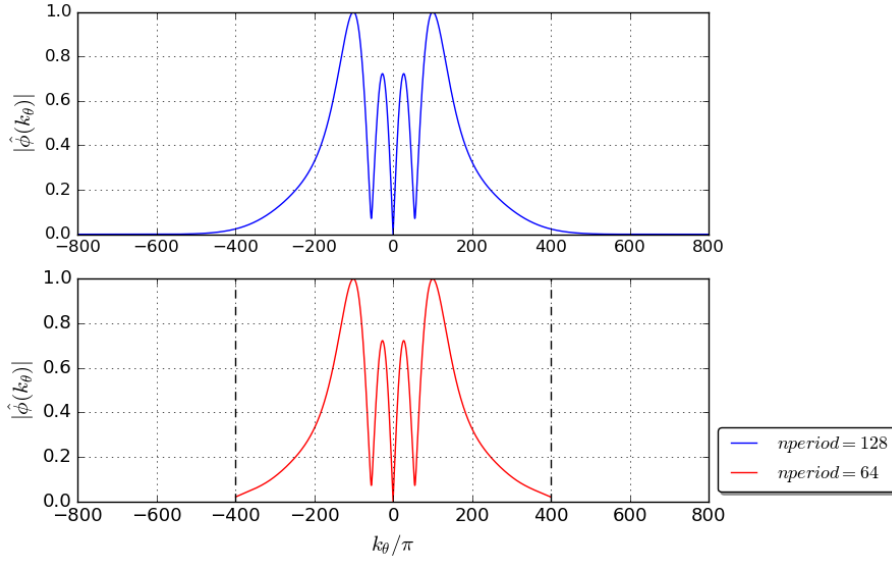


**Figure 4.6:** The comparison of the mode structure with sufficient and insufficient grid extent in GS2 simulations. The graph shows the modulus of  $\hat{\phi}$  in GS2 simulations as a function of the GS2 grid  $k_\theta$ . The top panel is calculated with sufficient grid extent ( $nperiod = 128$ ) while the bottom panel is calculated with insufficient grid extent ( $nperiod = 64$ ). The dash lines in the bottom panel denotes the grid size of the simulations. The physics parameters are kept the same as in figure (4.5).

Figure (4.6) shows the comparison of the accurate and inaccurate field calculated with sufficient or insufficient grid extent in GS2, respectively. It can be seen that in the bottom panel where the  $nperiod$  is not large enough, the edge of the field cannot well resolve to zero. In this case the simulation gives an inaccurate result. The GS2 results presented in figure (4.2) require  $nperiod = 128$  and  $ntheta = 8$  for the collisionless branch while for the collisional branch  $nperiod = 16$  and  $ntheta = 4$  are already adequate. Similarly, the velocity space resolution parameters,  $negridd$  (energy grid parameter) and  $ngauss$  (pitch angle grid parameter) are also checked. For both branches, we need  $negridd = 8$  and  $ngauss = 16$ . Besides, a relatively fine time step  $delt$  is required for the correctly resolved result. For our simulations it requires  $delt = 0.2$  for the collisional branch and  $delt = 0.05$  for the collisionless branch.

The highly extended grid size and fine spatial and temporal resolutions make the simulations for the collisionless branch very expensive<sup>4</sup>. We suspect that this might be a reason for the collisionless tearing parity mode not been seen in previous slab work, for example, in [101].

<sup>4</sup>Although some recent studies [98, 99, 100] probe the possibility of advanced re-mapping algorithm to reduced the need of large resolutions, those methods have not yet been implemented in simulation codes.

Some other numerical parameters, on the other hand, does not affect the accuracy of simulation results, for example, unit length  $f_{prim}$  and reference shear length  $shat$ . As our simulations are linear, as long as these related numerical parameters are kept in the correct ratio regarding the real physics parameters, the GS2 simulation results are correct and accurate.

### 4.3 Reviewing and verifying the assumptions in slab model derivation

To understand why the collisionless branch is not recovered in the slab model, we recall the assumptions taken for the derivation in Section 3.4.1. The two most important ones are small  $\mathbf{v}_{\parallel} \cdot \nabla g_i$  and small  $k_x$  assumption. Mathematically these two can be written as  $|\omega| \gg k_{\parallel} v_i$  and  $k_x \rho_i \ll 1$ . The first one is related to the ion dynamics model while the second one is about FLR effects.

#### 4.3.1 Ion dynamics model

The assumption  $|\omega| \gg k_{\parallel} v_i$  is tested in figure (4.7). It is shown to be broadly satisfied across the collision frequency range. Note that this assumption is equivalent to treating ions as stationary compared with electrons, therefore the eigenmode equations for

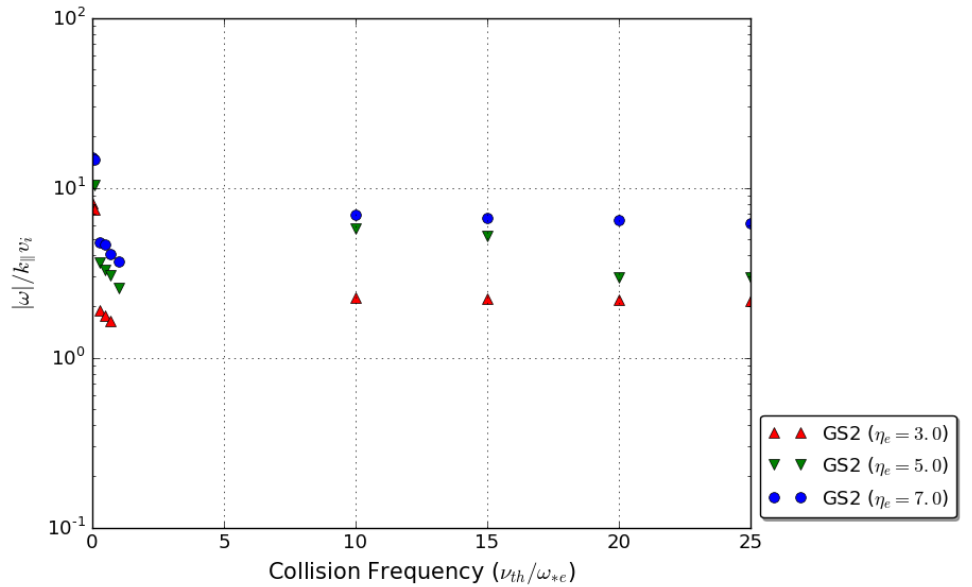


**Figure 4.7:** The validation test for the small  $k_{\parallel} v_i$  assumption for the data points in figure (4.2) for different collision frequencies. Shown in the graph are  $|\omega|/k_{\parallel} v_i$  values in GS2 calculation.

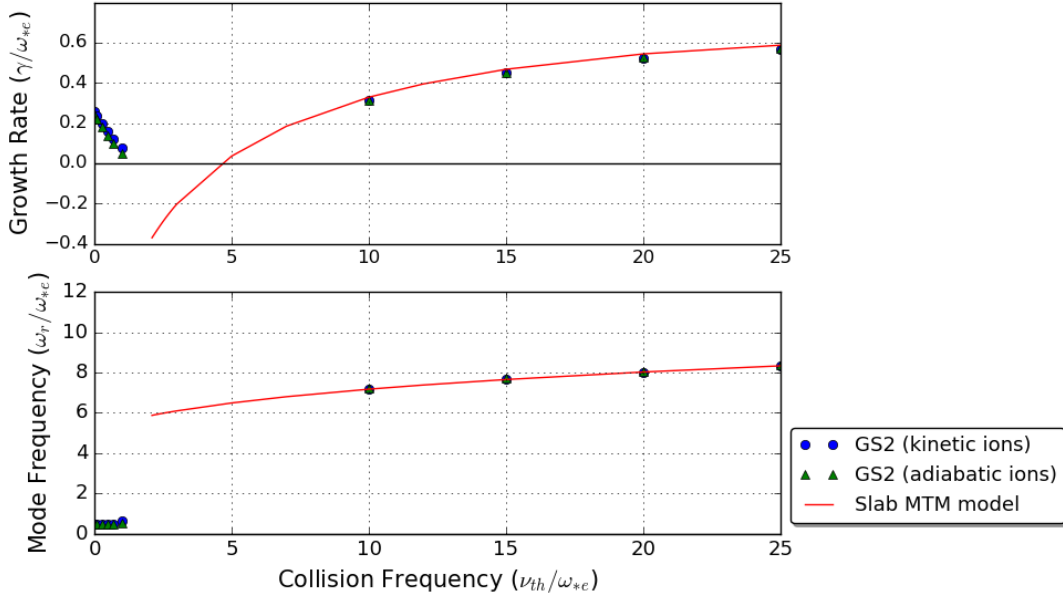


**Figure 4.8:** The validation for the inference of adiabatic ions using GS2. Data points for  $\eta_e = 5.0$  in figure (4.2) are calculated in GS2 with kinetic ions or adiabatic ions, respectively, and benchmarked against the numerical results from the slab MTM model. Electrons are kept kinetic.

MTM should be able to be further reduced by employing adiabatic ions. Without deriving another set of equations, we can conveniently test this argument in GS2 simulations by switching the ion dynamics model from kinetic to adiabatic. Figure (4.8) proves that the adiabatic ion model has little impact on both collisional and collisionless branches. This result is consistent with the physics picture that the main driving mechanism for MTMs lies in electrons. Exploiting this conclusion, we will use adiabatic ions to derive the eigenmode model of the collisionless branch in Chapter 5.

### 4.3.2 FLR effects from electrons

We have seen in figure (4.3) that the collisionless branch has narrower mode structures than the collisional one. In figure (4.9) we confirm that the radial wavenumber  $k_x$  becomes approximately  $10^2$  times larger when collision frequency decreases to zero. This transition, however, is not affected by the electron temperature gradient or other parameters. The  $k_x$  value is calculated through the width of the mode structures in GS2 data (in Fourier space, see figure (4.6)) as  $k_x = w_\theta \hat{s} k_y$ , where  $w_\theta$  is the measured mode structure width in GS2 coordinates and  $\hat{s}$  is a reference shear scale length set in GS2 simulations; shown in the figure it is normalised to  $k_x \rho_i$  (the left hand side coordinate) and  $k_x \rho_e$  (the right hand side coordinate). Due to the ambiguity in defining the width shown in figure (4.6) in the linear simulations, the measured  $k_x$  values are fitted with error bars. Never-

theless, it can be concluded that the observed  $k_x$  value violates the employed small  $k_x$  assumption in the collisionless condition, therefore the collisionless branch is actually excluded from the conventional slab MTM theory.

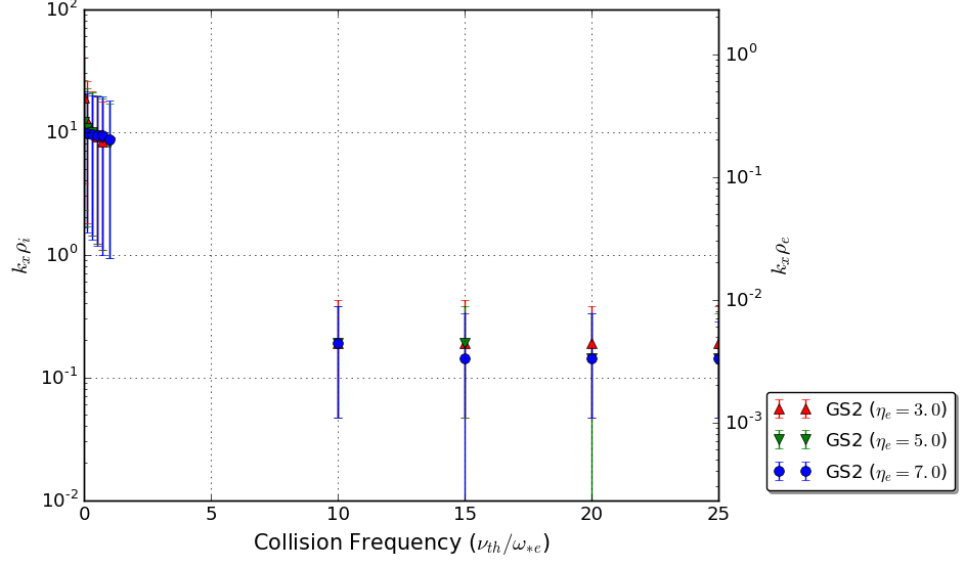


**Figure 4.9:** The validation for the small  $k_x$  assumption using GS2 calculated  $k_x\rho_i$  values for the data points in figure (4.2) along the collision frequencies. The right axis shows the value of  $k_x\rho_e$  as a comparison.

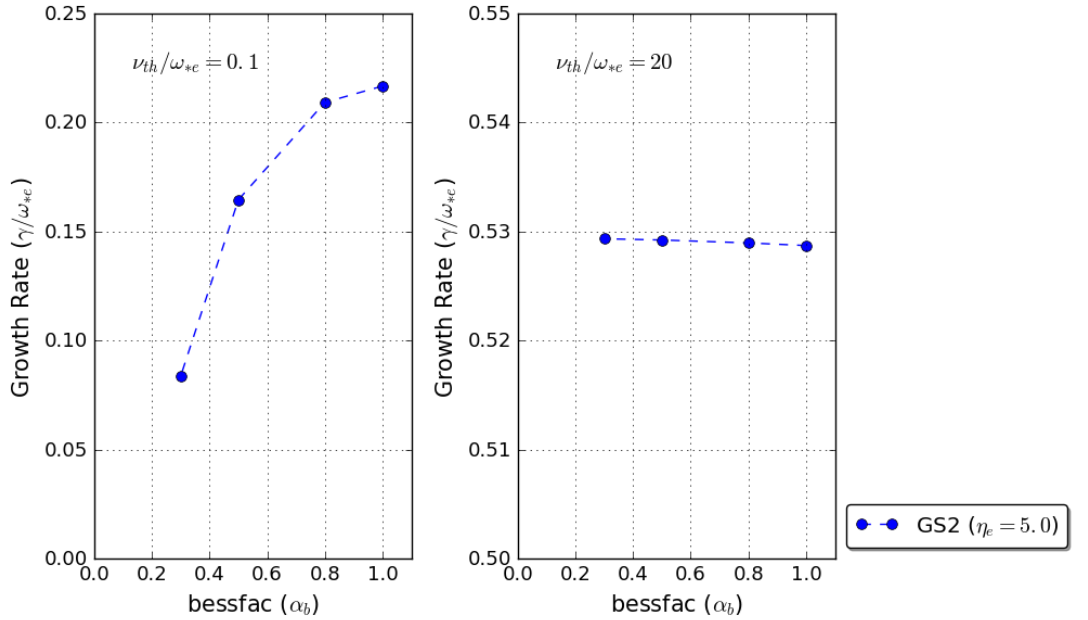


**Figure 4.10:** The impact of the electron FLR effects on the growth rate of collisionless and collisional branches in GS2 simulations. A collisionless case (left panel,  $\nu_{th}/\omega_{*e} = 0.1$ ) and collisional case (right panel,  $\nu_{th}/\omega_{*e} = 20$ ) are shown with  $k_y\rho_i = 0.3$ ,  $\eta_e = 5.0$ ,  $\beta = 0.005$  and  $L_n/L_s = 0.05$ .

Specifically, figure (4.9) shows that  $k_x \rho_e$  increases to comparable to 1 when collision frequency drops. This leads to a surmise that the Bessel function argument in the gyrokinetic equation (3.10) for electrons is actually not neglectable for the collisionless branch: it gives a clue that the electron FLR effects could be an important factor at the collisionless conditions.

To further test this surmise, we probe the impact of FLR effects directly in GS2 simulations by including a Bessel scaling parameter. This parameter, *bessfac* (noting as  $\alpha_b$ ), is defined within the Bessel function argument as a multiplying factor of the original argument, which can be written in the form of  $J_0(\alpha_b k)$ . By default  $\alpha_b = 1$  and all kinetic species are treated with full gyrokinetic effects including FLR effects. Such a treatment provides a means to suppress the weight of FLR effects in gyroaveraging. By tuning  $\alpha_b$  down towards 0, we can investigate the impact of ignoring the electron FLR effects in the analytic model. Figure (4.10) shows the impact on collisionless and collisional branches respectively. The growth rate of the collisionless branch is shown to drop rapidly with  $\alpha_b$  decreasing, while the collisional one is insensitive to this parameter. Note that here for the collisionless case, we have set collision frequency  $\nu_{th}/\omega_{*e} = 0.1$  rather than exact by zero. This is because the GS2 simulation requires certain dissipation to confine the mode; thus if the Bessel parameter and collision frequency are both zero, it needs infinite simulation domain and calculation time. The different behaviour of the two branches in figure (4.10) demonstrates that the electron FLR effects can be safely neglected for the collisional branch, but should be taken into consideration for the collisionless model.

## 4.4 Impact of the collision model

As mentioned in Section 3.3.3, GS2 employs a more complete collision model [82, 83] than the reduced pitch angle scattering operator. In Fourier space, the full set of electron-collision operator terms in GS2 can be summarised in the form of [95, 102]

$$C^{GS2}(\hat{g}) = C_L^{GS2}(\hat{g}) + C_E^{GS2}(\hat{g}) + C_M^{GS2}(\hat{g}), \quad (4.11)$$

in which

$$C_L^{GS2}(\hat{g}) = \frac{\nu}{2} \left[ \frac{\partial}{\partial \xi} (1 - \xi^2) \frac{\partial}{\partial \xi} - \frac{k_{\perp}^2 \rho^2}{2} (1 + \xi^2) \right] \hat{g} \quad (4.12)$$

is the full Lorentz operator derived from the linearised Landau collision operator [80],  $C_E^{GS2}$  is an energy diffusion operator and  $C_M^{GS2}$  contains momentum and energy conserving corrections. The first term in  $C_L^{GS2}$  is the pitch angle scattering in equation (3.15); the second term is derived from the change of gyrophase angle during the collisions [80],

which can be described as a gyro-diffusion effect, and is excluded from our slab MTM model. We notice that the second term in  $C_L^{GS2}$  is in the magnitude of  $(k_x \rho_e)^2$ , which becomes large only in the collisionless conditions. Therefore, this term in principle should be considered for the collisionless branch, but should not play an important role for the collisional mode.

In the input parameters for GS2 there are instructions to control which collision operators are included in the calculation, which provides a means to validate the choice of pitch angle scattering Lorentz operator in the slab MTM model. In the above GS2 simulations, the collision model is set as the *lorentz* option, which includes  $C_L^{GS2}$  and a flow correction term<sup>5</sup> in  $C_M^{GS2}$  [95]. The full collision option takes  $C_E^{GS2}$  and the rest of  $C_M^{GS2}$  into account and can be adopted by using the *default* option. Apart from the modular design of the GS2 collision model options, the diffusion term in  $C_L^{GS2}$  can be independently tested using another scaling parameter, *cfac* (noting as  $\alpha_c$ ), acting on  $k_\perp$  in GS2. Similar to  $\alpha_b$ , taking  $\alpha_c = 0$  turns off this term. Furthermore, by default the collision frequency  $\nu$  is velocity-dependent; based on a conclusion in [71] that the collisionless toroidal MTM can even be seen with a velocity-independent collision operator, it is worth conducting a test of the velocity dependency in the collision frequency for the collisionless branch in slab geometry. In GS2, this can be implemented with the *const\_v* option, which adopts  $\nu = \nu_{th}$  in the calculation and also turns off the diffusion term in  $C_L^{GS2}$  as well as the flow correction term.

Figure (4.11) compares the following four scenarios: the full collision model adopts all terms in  $C^{GS2}$  (with the *default* option); the GS2 Lorentz model uses both terms in  $C_L^{GS2}$  (with the *lorentz* option and  $\alpha_c = 1$ ); the pitch angle scattering model includes only the first term in  $C_L^{GS2}$  (with the *lorentz* option and  $\alpha_c = 0$ ); and the velocity-independent model takes  $\nu = \nu_{th}$  by the *lorentz* and *const\_v* options. The fact that the collisionless mode has positive growth rate even with simple collision operator implies that the choice of collision operator does not affect whether these modes are stable or unstable. It can be confirmed that the pitch angle scattering model matches well with the full Lorentz collision operator in the collisional regime, but in the collisionless regime the diffusion term is required. This result is consistent with the higher  $k_x$  of the collisionless branch identified in figure (4.9).

On the other hand, in the collisionless condition, the GS2 Lorentz operator gives a good agreement with the full collision model which also considers the conservation correction terms; however, in the collisional branch the slab MTM is shown to be suppressed signi-

<sup>5</sup>The form of this correction term can be found in equation (28) of [82]. We will discuss its impact in Section 6.3.

#### 4.4. Impact of the collision model

ificantly by  $C_E^{GS2}$  and  $C_M^{GS2}$  terms. Although this is a concern that requires further study for the collisional slab MTM theory, this is not the main focus of this thesis so we do not

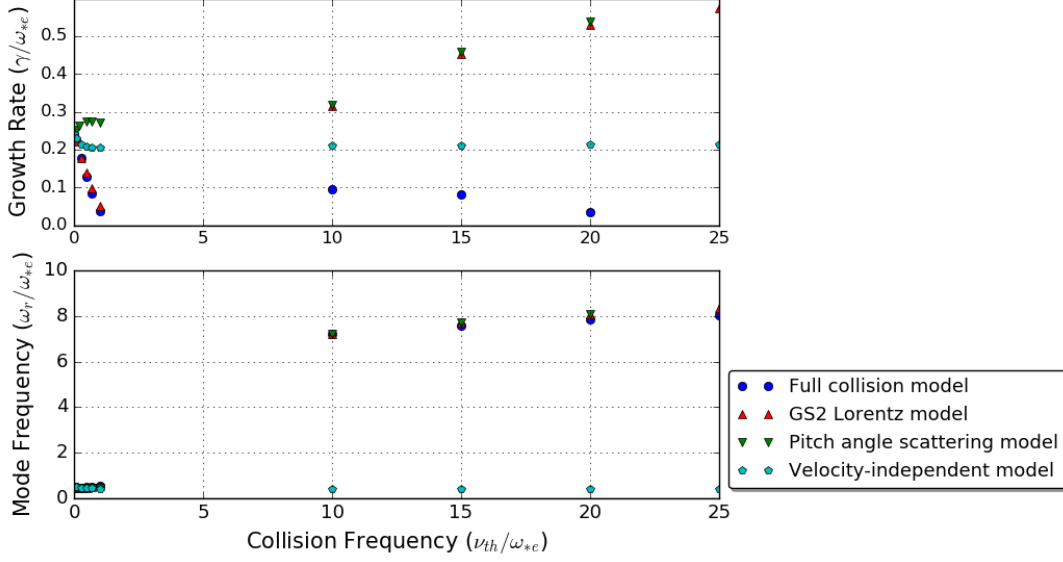


**Figure 4.11:** Comparison of the GS2 collision models in four options: the full collision model (all terms in  $C^{GS2}$ ), the GS2 Lorentz model ( $C_L^{GS2}$  with  $\alpha_c = 1$ ), the pitch angle scattering model ( $C_L^{GS2}$  with  $\alpha_c = 0$ ), and the velocity-independent model ( $C_L^{GS2}$  with *const\_v* option). The related physics parameters are  $k_y \rho_i = 0.3$ ,  $\eta_e = 5.0$ ,  $\beta = 0.005$  and  $L_n/L_s = 0.05$ .

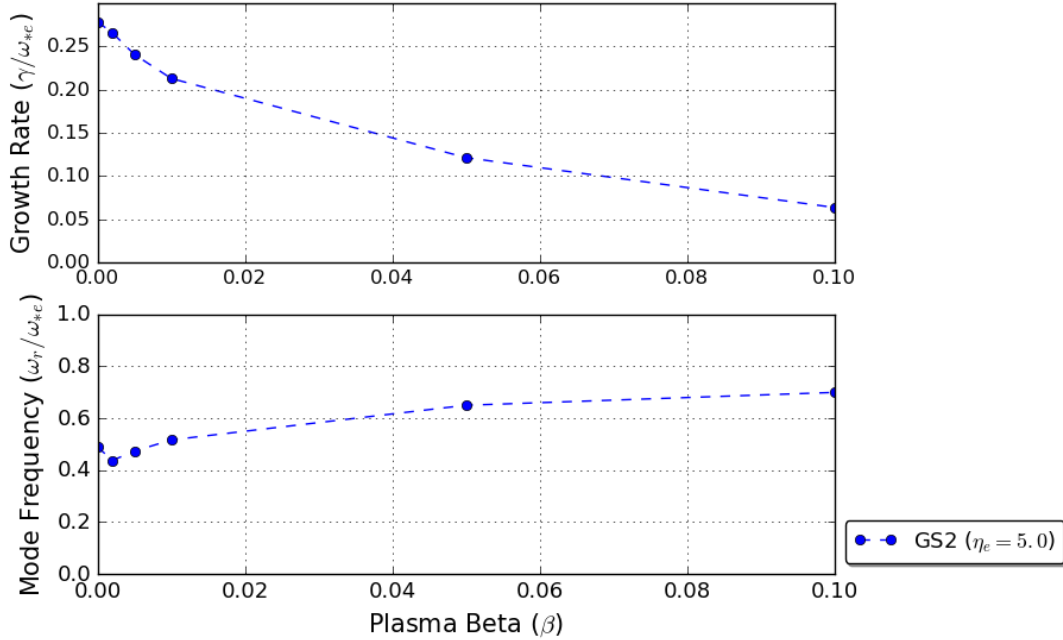


**Figure 4.12:** The growth rate and mode frequency of the collisionless instability as a function of plasma beta. Here  $k_y \rho_i = 0.3$ ,  $\eta_e = 5.0$ ,  $L_n/L_s = 0.05$  and  $\nu_{th}/\omega_{*e} = 0.0$ .

look into it here. Figure (4.11) also concludes that the velocity dependency in the collision frequency is necessary to capture the mode correctly. Actually the velocity-independent results shown in the collisional condition are the extension of the collisionless branch. Substituting  $\nu = \nu_{th}$  into the slab MTM model, we calculate that here the eigenvalue  $\omega$  has a negative growth rate, which therefore is not identified by GS2.

Focusing on the collisionless branch, we will adopt the full Lorentz collision operator<sup>6</sup> in equation (4.12) to derive the collisionless eigenmode model in Chapter 5, in which the collision frequency is velocity-dependent.

## 4.5 Electrostatic limit of the collisionless mode

In this subsection, we investigate the influence of the electromagnetic field fluctuations on this collisionless mode. This can be done by varying the value of plasma beta  $\beta$ . A higher  $\beta$  relates to stronger fluctuations in the magnetic field, while  $\beta = 0$  provides the electrostatic limit. The result is shown in figure (4.12). We find that the collisionless branch persists, and is even more unstable, in the electrostatic limit. Recalling the neglectable ion dynamics leads to a supposition that this collisionless mode, even though featuring with tearing parity, might fundamentally be an ETG mode. To verify this point, in Chapter 5 we first develop an electrostatic analytic model then an electromagnetic analytic model to allow detailed study.

---

<sup>6</sup>Note that figure (4.11) actually implies that the pitch angle scattering term in the collision operator does not play an important role. However, this does not reduce the complexity of derivation to be discussed in the next chapter due to the five-diagonal matrix  $\mathbf{P}$  in equation (5.28). In this thesis, we keep both terms.



# Chapter 5

## Developing the collisionless micro-scale tearing mode model

The GS2 simulation results demonstrate that the collisionless micro-scale tearing parity mode requires considering FLR effects for electrons. Meanwhile, as this mode can even exist in the electrostatic limit, we identify it with a tearing parity branch of an ETG mode, though the electromagnetic effects are still important (see Section 6.2). To demonstrate the physics interpretation of the drive mechanism, we develop two models from the gyrokinetic theory. In Section 5.1 we develop an electrostatic model in the zero collision frequency limit to prove the ETG nature of this mode. In Section 5.2, an electromagnetic model with finite collision frequency gives a more complete picture of this mode and provides a direct benchmark with GS2 results. The derivation is based on the same slab geometry as illustrated in figure (3.1). Adiabatic ions are adopted in both models as informed by GS2 and the assumptions for  $f_0 = f_M$  and  $T_i = T_e = T$  are kept.

### 5.1 Electrostatic model at zero collision frequency

The electron gyrokinetic equation for this case includes both the parallel perturbation term and the Bessel function. Following a similar procedure to that in Section 3.4.1 when calculating for ion perturbation and density, we can derive a second order differential eigenmode equation. However, due to the extreme complexity regarding the coupling of Bessel function and Legendre polynomial (see Appendix B), the previous derivation method does not work for an electromagnetic model in Section 5.2. We therefore develop an alternative expansion approach and we demonstrate the derivation for both models in this approach. It is more convenient to analyse in Fourier space. Fourier transformation

of the electron gyrokinetic equation and the quasi-neutrality equation yields

$$\left(\omega - i\frac{k_y}{L_s}v_{\parallel}\frac{\partial}{\partial k}\right)\hat{g}(k) = \frac{e}{T}f_M(\omega - \omega_{*e}^T)J_0(k_{\perp}\rho_e)\hat{\phi}(k), \quad (5.1)$$

$$-n_0\frac{e\hat{\phi}(k)}{T} + \int_{-\infty}^{\infty}d^3\mathbf{v}\cdot\hat{g}(k)J_0(k_{\perp}\rho_e) = n_0\frac{e\hat{\phi}(k)}{T}, \quad (5.2)$$

where we have adopted a Boltzmann response for the ions. Here, the  $\hat{\phantom{x}}$  symbol represents the functions in Fourier space and we have omitted the species subscript. Expanding Bessel functions to the second order, equations (5.1) and (5.2) become

$$\left(\omega - i\frac{k_y}{L_s}v_{\parallel}\frac{\partial}{\partial k}\right)\hat{g} = \frac{e}{T}f_M(\omega - \omega_{*e}^T)\left(1 - \frac{k_y^2v_{\perp}}{4\omega_{ce}^2} - \frac{k_x^2v_{\perp}}{4\omega_{ce}^2}\right)\hat{\phi}, \quad (5.3)$$

$$2n_0\frac{e\hat{\phi}}{T} = \int_{-\infty}^{\infty}d^3\mathbf{v}\cdot\left(1 - \frac{k_y^2v_{\perp}^2}{4\omega_{ce}^2} - \frac{k_x^2v_{\perp}^2}{4\omega_{ce}^2}\right)\hat{g}. \quad (5.4)$$

Conducting the inverse Fourier transform to real space gives

$$\left(\omega - \frac{k_y x}{L_s}v_{\parallel}\right)g = \frac{e}{T}f_M(\omega - \omega_{*e}^T)\left(1 - \frac{k_y^2v_{\perp}^2}{4\omega_{ce}^2} + \frac{v_{\perp}^2}{4\omega_{ce}^2}\frac{\partial^2}{\partial x^2}\right)\phi, \quad (5.5)$$

$$2n_0\frac{e\phi(x)}{T} = \int_{-\infty}^{\infty}d^3\mathbf{v}\cdot\left(1 - \frac{k_y^2v_{\perp}^2}{4\omega_{ce}^2} + \frac{v_{\perp}^2}{4\omega_{ce}^2}\frac{\partial^2}{\partial x^2}\right)g. \quad (5.6)$$

Substituting  $g$  from (5.5) into (5.6) gives the second order differential equation for  $\phi$  with  $\omega$  being the eigenvalue

$$2\pi^{3/2}v_e^3\phi = \int_{-\infty}^{\infty}d^3\mathbf{v}\cdot e^{-v^2/v_e^2}\left(1 - \frac{k_y^2v_{\perp}^2}{4\omega_{ce}^2} + \frac{v_{\perp}^2}{4\omega_{ce}^2}\frac{\partial^2}{\partial x^2}\right) \left[\frac{\omega - \omega_{*e}^T}{\omega - k_y x v_{\parallel}/L_s}\left(1 - \frac{k_y^2v_{\perp}^2}{4\omega_{ce}^2} + \frac{v_{\perp}^2}{4\omega_{ce}^2}\frac{\partial^2}{\partial x^2}\right)\phi\right]. \quad (5.7)$$

To simplify the notation, we normalise the variables as  $\bar{\omega} = \omega/\omega_{*e}$ ,  $\bar{k}_y = k_y\rho_e$ ,  $\bar{x} = x/\rho_e$ ,  $\bar{\phi} = -e\phi/T$  and note  $s = v_{\parallel}/v_e$ ,  $t = v_{\perp}/v_e$ ,  $\epsilon = L_n/L_s$ . The normalised equation becomes

$$16\sqrt{\pi}\bar{\phi} = \int_{-\infty}^{\infty}ds \int_0^{\infty}t dt \cdot e^{-(s^2+t^2)} \left[\bar{\omega} - 1 - \eta\left(s^2 + t^2 - \frac{3}{2}\right)\right] \left[(4 - \bar{k}_y^2 t^2)\left(\frac{4 - \bar{k}_y^2 t^2 + t^2 \frac{\partial^2}{\partial \bar{x}^2}}{\bar{\omega} - 2\epsilon \bar{x} s}\right) + t^2 \frac{\partial^2}{\partial \bar{x}^2} \left(\frac{4 - \bar{k}_y^2 t^2 + t^2 \frac{\partial^2}{\partial \bar{x}^2}}{\bar{\omega} - 2\epsilon \bar{x} s}\right)\right] \bar{\phi}. \quad (5.8)$$

In the parameter range relevant to our study,  $\bar{k}_y \ll 1$  holds<sup>1</sup>, so that  $\bar{k}_y^2$  terms can be safely neglected. Furthermore, the third and fourth orders of the differential operator are also negligible. Equation (5.8) then becomes

$$\begin{aligned} \sqrt{\pi}\bar{\phi} = & \int_{-\infty}^{\infty} ds \int_0^{\infty} dt \cdot e^{-s^2} e^{-t^2} t \left( \bar{\omega} - 1 + \frac{3}{2}\eta - \eta s^2 - \eta t^2 \right) \\ & \left[ \left( \frac{1}{\bar{\omega} - 2\epsilon\bar{x}s} + \frac{2\epsilon^2 s^2 t^2}{(\bar{\omega} - 2\epsilon\bar{x}s)^3} \right) \bar{\phi} + \frac{\epsilon s t^2}{(\bar{\omega} - 2\epsilon\bar{x}s)^2} \frac{\partial}{\partial \bar{x}} \bar{\phi} \right. \\ & \left. + \left( \frac{t^2}{2(\bar{\omega} - 2\epsilon\bar{x}s)} + \frac{\epsilon^2 s^2 t^4}{2(\bar{\omega} - 2\epsilon\bar{x}s)^3} \right) \frac{\partial^2}{\partial \bar{x}^2} \bar{\phi} \right]. \end{aligned} \quad (5.9)$$

The integration with respect to  $t$  is simply the Gaussian integral

$$\int_0^{\infty} e^{-t^2} t^n dt = \frac{1}{2} \Gamma\left(\frac{n+1}{2}\right), \quad t \in \mathcal{R} \text{ and } n \in \mathcal{N}. \quad (5.10)$$

To evaluate the integration with respect to  $s$ , we define a set of recursive functions in the form of a generalised plasma dispersion function

$$Z_{m,n}(\alpha) = \int_{-\infty}^{\infty} \frac{e^{-s^2} s^m}{(s - \alpha)^{n+1}} ds, \quad \alpha \in \mathcal{C}, \quad s \in \mathcal{R} \text{ and } m, n \in \mathcal{N}. \quad (5.11)$$

When  $\alpha = 0$ , it reduces to the Gaussian integral. When  $\alpha \neq 0$ , using integration by parts, all  $Z_{m,n}(\alpha)$  can be related to  $Z_{0,0}(\alpha)$  through

$$Z_{m,n}(\alpha) = \frac{m}{n} Z_{m-1,n-1}(\alpha) - \frac{2}{n} Z_{m+1,n-1}(\alpha), \quad \text{for } n \geq 1, \quad (5.12)$$

$$Z_{m,0}(\alpha) = \alpha Z_{m-1,0}(\alpha) + \frac{1 + (-1)^{m-1}}{2} \Gamma\left(\frac{m}{2}\right), \quad (5.13)$$

$$Z_{0,0}(\alpha) = \int_{-\infty}^{\infty} \frac{e^{-s^2}}{s - \alpha} ds = i\pi W(\alpha), \quad (5.14)$$

where  $W(\alpha)$  is known as the Faddeeva function

$$W(\alpha) = e^{-\alpha^2} \left( 1 + \frac{2i}{\sqrt{\pi}} \int_0^{\alpha} e^{t^2} dt \right), \quad \alpha, t \in \mathcal{C}. \quad (5.15)$$

Therefore, when  $\bar{x} \neq 0$ , equation (5.9) can be eventually simplified into a second order

<sup>1</sup>Note the anisotropy in  $k_y$  and  $k_x$ . As a consequence, the binormal wavelength of this mode is at the ion scale while the radial wavelength is at the electron scale. Such a parameter range is not typically captured by many gyrokinetic simulations. A very recent gyrokinetic study in [103] also finds a novel toroidal ETG mode in the small  $k_y$  condition. On the other hand, another recent gyrokinetic study in [104] demonstrates that it is possible for the modes at multiple (even largely separated) scales to nonlinearly interact, which gives a challenge regarding the future work (see Section 7.2).

differential equation in the form of

$$C_0 \bar{\phi} + C_1 \frac{\partial}{\partial \bar{x}} \bar{\phi} + C_2 \frac{\partial^2}{\partial \bar{x}^2} \bar{\phi} = 0, \quad (5.16)$$

in which the coefficients  $C_0$ ,  $C_1$  and  $C_2$  are given by

$$C_0 = -\sqrt{\pi} - \frac{1}{4\epsilon\bar{x}} \left[ \left( \bar{\omega} - 1 + \frac{1}{2}\eta \right) Z_{0,0} - \eta Z_{2,0} \right] - \frac{1}{8\epsilon\bar{x}^3} \left[ \left( \bar{\omega} - 1 - \frac{1}{2}\eta \right) Z_{2,2} - \eta Z_{4,2} \right], \quad (5.17)$$

$$C_1 = \frac{1}{8\epsilon\bar{x}^2} \left[ \left( \bar{\omega} - 1 - \frac{1}{2}\eta \right) Z_{1,1} - \eta Z_{3,1} \right], \quad (5.18)$$

$$C_2 = -\frac{1}{8\epsilon\bar{x}} \left[ \left( \bar{\omega} - 1 - \frac{1}{2}\eta \right) Z_{0,0} - \eta Z_{2,0} \right] - \frac{1}{16\epsilon\bar{x}^3} \left[ \left( \bar{\omega} - 1 - \frac{3}{2}\eta \right) Z_{2,2} - \eta Z_{4,2} \right], \quad (5.19)$$

with  $Z_{m,n} = Z_{m,n}(\bar{\omega}/2\epsilon\bar{x})$ . For the centre of the slab where  $\bar{x} = 0$ , these coefficients are well-defined as

$$C_0|_{\bar{x}=0} = \sqrt{\pi} \left[ -1 + \frac{\bar{\omega} - 1}{2\bar{\omega}} + \frac{\epsilon^2 (\bar{\omega} - 1 - 2\eta)}{2\bar{\omega}^3} \right], \quad (5.20)$$

$$C_1|_{\bar{x}=0} = 0, \quad (5.21)$$

$$C_2|_{\bar{x}=0} = \sqrt{\pi} \left[ \frac{\bar{\omega} - 1 - \eta}{4\bar{\omega}} + \frac{\epsilon^2 (\bar{\omega} - 1 - 3\eta)}{4\bar{\omega}^3} \right]. \quad (5.22)$$

Note that  $\bar{k}_y$  does not appear explicitly in the coefficients, but is contained implicitly in the normalisation by  $\omega_{*e}$ . This means that the eigenmode frequency and growth rate, if normalised to  $\omega_c$ , are approximately proportional to  $k_y$  when  $k_y$  is small; this is in agreement with the slab ETG dispersion relation  $\omega(k_y)$  [54, 103]. The coefficients also indicate that this mode is mostly sensitive to magnetic shear and electron temperature gradient. Numerical solution results for this model will be presented in Chapter 6.

## 5.2 Electromagnetic model at finite collision frequency

To study the electromagnetic effects and the impact of collision frequency on this mode, we include the parallel magnetic vector potential and full Lorentz collision operator in

equation (4.12). The gyrokinetic equation for electrons is

$$\begin{aligned} & \left[ \omega - i \frac{k_y}{L_s} v \xi \frac{\partial}{\partial k} - \frac{i\nu}{2} \frac{\partial}{\partial \xi} (1 - \xi^2) \frac{\partial}{\partial \xi} + \frac{i\nu}{4} k_\perp^2 \rho^2 (1 + \xi^2) \right] \hat{g} \\ & = \frac{e}{T} f_M (\omega - \omega_{*e}^T) J_0(k_\perp \rho_\perp) \left[ \hat{\phi}(k) - v \xi \hat{A}_\parallel(k) \right]. \end{aligned} \quad (5.23)$$

Following the same expansion approach and orthogonality relation explained in Section 5.1 and Section 3.4.1, equation (5.23) can be normalised to

$$\begin{aligned} & \frac{1}{2n+1} \left[ \left( \bar{\omega} + \frac{i\bar{\nu}}{2} n(n+1) \right) h_n - 2\epsilon \bar{x} s \left( \frac{n}{2n-1} h_{n-1} + \frac{n+1}{2n+3} h_{n+1} \right) \right. \\ & \quad \left. + \frac{i\bar{\nu}}{4} u^2 \left( \bar{k}_y^2 - \frac{\partial^2}{\partial \bar{x}^2} \right) \left( \frac{n(n-1)}{(2n-3)(2n-1)} h_{n-2} \right. \right. \\ & \quad \quad \left. \left. + \frac{6n^2 + 6n - 4}{(2n-1)(2n+3)} h_n + \frac{(n+1)(n+2)}{(2n+3)(2n+5)} h_{n+2} \right) \right] \\ & = -\frac{n_0}{\pi^{3/2} v_e^3} e^{-u^2} \left[ \bar{\omega} - 1 - \eta \left( u^2 - \frac{3}{2} \right) \right] \\ & \quad \begin{cases} \left[ \left( 1 - \frac{1}{6} \bar{k}_y^2 u^2 \right) \bar{\phi} + \frac{1}{6} u^2 \frac{\partial^2}{\partial \bar{x}^2} \bar{\phi} \right], & \text{for } n = 0, \\ \left[ -\left( \frac{2}{3} u - \frac{4}{15} \bar{k}_y^2 u^3 \right) \bar{A}_\parallel - \frac{4}{15} u^3 \frac{\partial^2}{\partial \bar{x}^2} \bar{A}_\parallel \right], & \text{for } n = 1, \\ \left[ \frac{1}{30} \bar{k}_y^2 u^2 \bar{\phi} - \frac{1}{30} u^2 \frac{\partial^2}{\partial \bar{x}^2} \bar{\phi} \right], & \text{for } n = 2, \\ \left[ -\frac{1}{35} \bar{k}_y^2 u^3 \bar{A}_\parallel + \frac{1}{35} u^3 \frac{\partial^2}{\partial \bar{x}^2} \bar{A}_\parallel \right], & \text{for } n = 3, \\ 0, & \text{for } n \geq 4, \end{cases} \end{aligned} \quad (5.24)$$

in which  $u = v/v_e$ ,  $\bar{\nu} = \nu/\omega_{*e} = \bar{\nu}_{th}/u^3$  and  $\bar{A}_\parallel = A_\parallel/\rho_e B$ . Compared with equations (3.25) to (3.27), the FLR effects result in a series of differential equations on the right hand side; the diffusion term in the full Lorentz collision operator broadens the coupling in  $\{h_n\}$  series to the second neighbours.

To derive a tractable eigenmode model, we introduce a matrix approach by writing the equation (5.24) in the form of

$$(\mathbf{M} + \bar{k}_y^2 \mathbf{P}) \cdot \mathbf{h} - \mathbf{P} \cdot \frac{\partial^2 \mathbf{h}}{\partial \bar{x}^2} = K \mathbf{D}, \quad (5.25)$$

in which  $M$  is a two dimensional infinite tridiagonal matrix

$$M = \begin{pmatrix} \bar{\omega} & -\frac{2}{3}\epsilon\bar{x}u & 0 & 0 & 0 & \cdots \\ -\frac{2}{3}\epsilon\bar{x}u & \frac{1}{3}(\bar{\omega} + i\bar{\nu}) & -\frac{4}{15}\epsilon\bar{x}u & 0 & 0 & \cdots \\ 0 & -\frac{4}{15}\epsilon\bar{x}u & \frac{1}{5}(\bar{\omega} + 3i\bar{\nu}) & -\frac{6}{35}\epsilon\bar{x}u & 0 & \cdots \\ \vdots & \ddots & \ddots & \ddots & \ddots & \vdots \\ 0 & \cdots & -\frac{2(n-1)\epsilon\bar{x}u}{(2n-3)(2n-1)} & \frac{1}{2n-1}(\bar{\omega} + \frac{n(n-1)}{2}i\bar{\nu}) & -\frac{2n\epsilon\bar{x}u}{(2n-1)(2n+1)} & \cdots \\ \vdots & \ddots & \ddots & \ddots & \ddots & \ddots \end{pmatrix}, \quad (5.26)$$

$h$  is an infinite column vector containing  $h_n$  terms

$$h = \begin{pmatrix} h_0 \\ h_1 \\ h_2 \\ \vdots \end{pmatrix}, \quad (5.27)$$

$P$  is a two dimensional infinite five-diagonal matrix (whose nearest subdiagonal and superdiagonal elements are zero)

$$P = \frac{i\bar{\nu}}{4}u^2 \begin{pmatrix} \frac{4}{3} & 0 & \frac{2}{15} & 0 & 0 & \cdots \\ 0 & \frac{8}{15} & 0 & \frac{2}{35} & 0 & \cdots \\ \frac{2}{15} & 0 & \frac{32}{105} & 0 & \frac{4}{105} & \cdots \\ \vdots & \ddots & \ddots & \ddots & \ddots & \vdots \\ 0 & \cdots & \frac{(n-2)(n-1)}{(2n-5)(2n-3)(2n-1)} & 0 & \frac{6n^2-6n-4}{(2n-3)(2n-1)(2n+1)} & 0 & \frac{n(n+1)}{(2n-1)(2n+1)(2n+3)} \cdots \\ \vdots & \ddots & \ddots & \ddots & \ddots & \ddots & \ddots \end{pmatrix}, \quad (5.28)$$

$K$  is the coefficients for the matrices

$$K = -\frac{n_0}{\pi^{3/2}v_e^3}e^{-u^2} \left[ \bar{\omega} - 1 - \eta \left( u^2 - \frac{3}{2} \right) \right], \quad (5.29)$$

and  $D$  is an infinite column vector containing the differential terms on the right hand

side

$$\mathbf{D} = \begin{pmatrix} (1 - \frac{1}{6}\bar{k}_y^2 u^2) \bar{\phi} + \frac{1}{6} u^2 \frac{\partial^2 \bar{\phi}}{\partial \bar{x}^2} \\ - (\frac{2}{3} u - \frac{4}{15} \bar{k}_y^2 u^3) \bar{A}_{\parallel} - \frac{4}{15} u^3 \frac{\partial^2 \bar{A}_{\parallel}}{\partial \bar{x}^2} \\ \frac{1}{30} \bar{k}_y^2 u^2 \bar{\phi} - \frac{1}{30} u^2 \frac{\partial^2 \bar{\phi}}{\partial \bar{x}^2} \\ - \frac{1}{35} \bar{k}_y^2 u^3 \bar{A}_{\parallel} + \frac{1}{35} u^3 \frac{\partial^2 \bar{A}_{\parallel}}{\partial \bar{x}^2} \\ 0 \\ 0 \\ \vdots \end{pmatrix}. \quad (5.30)$$

Exploiting the small  $\bar{k}_y$  condition, equation (5.25) can be reduced to

$$\mathbf{M} \cdot \mathbf{h} - \mathbf{P} \cdot \frac{\partial^2 \mathbf{h}}{\partial \bar{x}^2} = \mathbf{K} \mathbf{D}_*, \quad (5.31)$$

in which

$$\mathbf{D}_* = \begin{pmatrix} \bar{\phi} + \frac{1}{6} u^2 \frac{\partial^2 \bar{\phi}}{\partial \bar{x}^2} \\ - \frac{2}{3} u \bar{A}_{\parallel} - \frac{4}{15} u^3 \frac{\partial^2 \bar{A}_{\parallel}}{\partial \bar{x}^2} \\ - \frac{1}{30} u^2 \frac{\partial^2 \bar{\phi}}{\partial \bar{x}^2} \\ \frac{1}{35} u^3 \frac{\partial^2 \bar{A}_{\parallel}}{\partial \bar{x}^2} \\ 0 \\ 0 \\ \vdots \end{pmatrix}. \quad (5.32)$$

We will drop the subscript in  $\mathbf{D}_*$  in our following discussions. Equation (5.31) gives a set of second order differential equations about  $\mathbf{h}$ , in which, however, both  $\mathbf{M}$  and  $\mathbf{D}$  are matrix functions of  $\bar{x}$ .

Using the matrix operation, we symbolically have

$$\mathbf{h} = \mathbf{K} \mathbf{M}^{-1} \cdot \mathbf{D} + \mathbf{M}^{-1} \cdot \mathbf{P} \cdot \frac{\partial^2 \mathbf{h}}{\partial \bar{x}^2}. \quad (5.33)$$

With the assumption that  $\partial^3 \mathbf{h} / \partial \bar{x}^3$  and higher orders are all small, and noticing that in our matrix  $\mathbf{M}$  it holds  $\partial^2 \mathbf{M} / \partial \bar{x}^2 = 0$ , the second order differential  $\partial^2 \mathbf{h} / \partial \bar{x}^2$  can be approximated as (see Appendix A.3)

$$\frac{\partial^2 \mathbf{h}}{\partial \bar{x}^2} \approx \mathbf{K} (\mathbf{I} - 2\mathbf{N}_2 \cdot \mathbf{P})^{-1} \cdot \left( 2\mathbf{N}_2 \cdot \mathbf{D} - 2\mathbf{N}_1 \cdot \frac{\partial \mathbf{D}}{\partial \bar{x}} + \mathbf{M}^{-1} \cdot \frac{\partial^2 \mathbf{D}}{\partial \bar{x}^2} \right), \quad (5.34)$$

in which  $\mathbf{I}$  is the infinite two dimensional identity matrix, and

$$\mathbf{N}_1 = \mathbf{M}^{-1} \cdot \frac{\partial \mathbf{M}}{\partial \bar{x}} \cdot \mathbf{M}^{-1}, \quad (5.35)$$

$$\mathbf{N}_2 = \mathbf{M}^{-1} \cdot \frac{\partial \mathbf{M}}{\partial \bar{x}} \cdot \mathbf{M}^{-1} \cdot \frac{\partial \mathbf{M}}{\partial \bar{x}} \cdot \mathbf{M}^{-1}. \quad (5.36)$$

The quasi-neutrality equation (5.6) provides

$$\begin{aligned} \bar{\phi} &= -\frac{\pi v_e^3}{n_0} \int_0^\infty u^2 du \sum_{n=0}^\infty \int_{-1}^1 d\xi \cdot \mathbf{P}_n(\xi) \left( 1 + \frac{1}{4} u^2 \frac{\partial^2}{\partial \bar{x}^2} - \frac{1}{4} u^2 \xi^2 \frac{\partial^2}{\partial \bar{x}^2} \right) h_n \\ &= -\frac{2\pi v_e^3}{n_0} \int_0^\infty u^2 du \cdot \left( h_0 + \frac{1}{6} u^2 \frac{\partial^2}{\partial \bar{x}^2} h_0 - \frac{1}{30} u^2 \frac{\partial^2}{\partial \bar{x}^2} h_2 \right), \end{aligned} \quad (5.37)$$

which can be presented as a product of vectors using the expressions in equations (5.33) and (5.34). We now define two row vectors as

$$\mathbf{R}_\phi = \left( 1 \quad 0 \quad 0 \quad 0 \quad 0 \quad \dots \right), \quad (5.38)$$

$$\mathbf{Q}_\phi = \left( \frac{1}{6} u^2 \quad 0 \quad -\frac{1}{30} u^2 \quad 0 \quad 0 \quad \dots \right). \quad (5.39)$$

Then the quasi-neutrality equation (5.37) gives the first eigenmode equation about  $\bar{\phi}$  in the matrix form

$$\begin{aligned} \bar{\phi} &= -\frac{2\pi v_e^3}{n_0} \int_0^\infty u^2 du \cdot \left( \mathbf{R}_\phi \cdot \mathbf{h} + \mathbf{Q}_\phi \cdot \frac{\partial^2 \mathbf{h}}{\partial \bar{x}^2} \right) \\ &= \frac{2}{\sqrt{\pi}} \int_0^\infty du \cdot u^2 e^{-u^2} \left[ \bar{\omega} - 1 - \eta \left( u^2 - \frac{3}{2} \right) \right] \left[ \mathbf{R}_\phi \cdot \mathbf{M}^{-1} \cdot \mathbf{D} \right. \\ &\quad \left. + \left( \mathbf{R}_\phi \cdot \mathbf{M}^{-1} \cdot \mathbf{P} + \mathbf{Q}_\phi \right) \cdot \left( \mathbf{I} - 2\mathbf{N}_2 \cdot \mathbf{P} \right)^{-1} \cdot \left( 2\mathbf{N}_2 \cdot \mathbf{D} - 2\mathbf{N}_1 \cdot \frac{\partial \mathbf{D}}{\partial \bar{x}} + \mathbf{M}^{-1} \cdot \frac{\partial^2 \mathbf{D}}{\partial \bar{x}^2} \right) \right]. \end{aligned} \quad (5.40)$$

Note that although the right hand side of this expression is in a matrix product form, it eventually results in a scalar quantity. But because that these matrices or vectors are all functions of  $u$ , the complexity in  $\mathbf{M}^{-1}$  coming into the integration makes it difficult to further simplify the scalar expression.

Similarly, from the perturbed parallel current density  $j_{\parallel}$  we can derive the other required

equation for  $\bar{A}_{\parallel}$

$$\begin{aligned}
 \left( \bar{y}_y^z - \frac{\partial^2}{\partial \bar{x}^2} \right) \bar{A}_{\parallel} &= -\frac{2\pi\mu_0 e \rho_e v_e^4}{B} \int_0^{\infty} u^2 du \cdot u \left( \mathbf{R}_A \cdot \mathbf{h} + \mathbf{Q}_A \cdot \frac{\partial^2 \mathbf{h}}{\partial \bar{x}^2} \right) \\
 &= \frac{2\beta}{\sqrt{\pi}} \int_0^{\infty} du \cdot u^3 e^{-u^2} \left[ \bar{\omega} - 1 - \eta \left( u^2 - \frac{3}{2} \right) \right] \left[ \mathbf{R}_A \cdot \mathbf{M}^{-1} \cdot \mathbf{D} \right. \\
 &\quad \left. + (\mathbf{R}_A \cdot \mathbf{M}^{-1} \cdot \mathbf{P} + \mathbf{Q}_A) \cdot (\mathbf{I} - 2\mathbf{N}_2 \cdot \mathbf{P})^{-1} \cdot \left( 2\mathbf{N}_2 \cdot \mathbf{D} - 2\mathbf{N}_1 \cdot \frac{\partial \mathbf{D}}{\partial \bar{x}} + \mathbf{M}^{-1} \cdot \frac{\partial^2 \mathbf{D}}{\partial \bar{x}^2} \right) \right], \tag{5.41}
 \end{aligned}$$

in which

$$\mathbf{R}_A = \left( 0 \quad \frac{2}{3} \quad 0 \quad 0 \quad 0 \quad 0 \quad \dots \right), \tag{5.42}$$

$$\mathbf{Q}_A = \left( 0 \quad \frac{1}{15}u^2 \quad 0 \quad -\frac{1}{35}u^2 \quad 0 \quad 0 \quad \dots \right). \tag{5.43}$$

Equations (5.40) and (5.41) form the set of second order differential eigenmode equations for the electromagnetic model. Directly comparing with the conventional slab MTM model in equations (3.33) and (3.34), the expressions for parallel conductivity  $\sigma_{\parallel}$  and parallel electric field  $E_{\parallel}$  can be considered as embedded in these matrix productions<sup>2</sup>. The calculation of  $\mathbf{M}^{-1}$  is the most challenging, which in principle requires the full infinite size of  $\mathbf{M}$ , even though only a few elements in  $\mathbf{M}^{-1}$  actually contributes to the coefficients due to the small number of non-zero terms in  $\mathbf{R}_{\phi}$ ,  $\mathbf{Q}_{\phi}$ ,  $\mathbf{R}_A$ ,  $\mathbf{Q}_A$  and  $\mathbf{D}$ . In practice, due to the decreasing value of the elements towards the higher rank, the matrix  $\mathbf{M}$  can be truncated, albeit still at a large size, during the calculation (see Section 6.1). Some mathematics discussions on inverse of tridiagonal matrices can be found in [105, 106, 107, 108], especially [105] provides a technique to estimate the upper and lower bounds for the truncation.

In a few special cases it is possible to conduct a simplification. For the conventional slab MTM model where the FLR effects for electrons are ignored and only the pitch angle scattering model is included in the collision operator, if we apply this matrix approach to the derivation, matrix  $\mathbf{D}$  contains only the first two elements which are also ordinary terms. In this case, matrices  $\mathbf{Q}_{\phi}$  and  $\mathbf{Q}_A$  are not required and the need of elements in  $\mathbf{M}^{-1}$  is also further reduced. After some cumbersome algebra, this can eventually result in the continued fraction expression in equation (3.28). For another case where the collision frequency  $\bar{\nu}_{th} = 0$  and at the centre of the slab  $\bar{x} = 0$ , the matrix  $\mathbf{M}$  becomes diagonal. Dropping the electromagnetic terms in this case, the eigenmode equation (5.40) becomes

<sup>2</sup>Attempts on simplifying the matrix expression indicate that  $\sigma_{\parallel}$  and  $E_{\parallel}$  may be re-defined with an extra phase in the scalar expression (see Appendix B).

## 5.2. *Electromagnetic model at finite collision frequency*

---

the same as our electrostatic collisionless model (5.16).

In the next chapter, we include the matrix operations into the numerical integration algorithm to calculate the eigenmodes of our models. Note that the  $\bar{k}_y$  also does not appear in the coefficients of electromagnetic model in the small  $\bar{k}_y$  condition. This will be validated in Section 6.1.1.

# Chapter 6

## Numerical calculation and discussion

### 6.1 Confirming the collisionless instability

We upgrade our numerical calculation code to solve the new electrostatic and electromagnetic models developed in Chapter 5. The main algorithm of the code has been described in Section 4.1. For the electrostatic model, the generalised plasma dispersion function  $Z_{m,n}$  in coefficients  $C_0$ ,  $C_1$  and  $C_2$  are calculated through the recursive relations (5.12), (5.13) and (5.14) when  $\bar{x}$  is not too small, in which the Faddeeva function calculation uses the routine in [109]. When  $\bar{x}$  is close to zero, the truncation error regarding  $W(1/\bar{x})$  can be very large, therefore the expansion form

$$C_0 = C_0|_{\bar{x}=0} + \frac{\sqrt{\pi}\epsilon^2\bar{x}^2}{\bar{\omega}^3} \left[ \bar{\omega} - 1 - \eta + \frac{18\epsilon^2}{\bar{\omega}^2} (\bar{\omega} - 1 - 3\eta) \right], \quad (6.1)$$

$$C_1 = C_1|_{\bar{x}=0} + \frac{\sqrt{\pi}\epsilon^2\bar{x}}{\bar{\omega}^3} (\bar{\omega} - 1 - 2\eta), \quad (6.2)$$

$$C_2 = C_2|_{\bar{x}=0} + \frac{\sqrt{\pi}\epsilon^2\bar{x}^2}{2\bar{\omega}^3} \left[ \bar{\omega} - 1 - 2\eta + \frac{18\epsilon^2}{\bar{\omega}^2} (\bar{\omega} - 1 - 4\eta) \right], \quad (6.3)$$

is adopted for small  $\bar{x}$  values, in which  $C_0|_{\bar{x}=0}$ ,  $C_1|_{\bar{x}=0}$  and  $C_2|_{\bar{x}=0}$  are given in equations (5.20), (5.21) and (5.22).

In the code for the electromagnetic model, *zgetrf*, *zgetri*, *zgttrf* and *zgttrs* modules in LAPACK [110] are adopted in calculating the inverse of the matrices. The size of  $M$  depends on collision frequency  $\bar{\nu}_{th}$  and magnetic shear scale length  $\epsilon$ ; the grid size  $\bar{x}_{\max}$  depends on these two parameters, as well as plasma beta  $\beta$ . For the parameters in the range of our calculations, the matrix size is set to  $30 \times 30$  and the grid size is  $40\bar{x}$ , with which the code has been tested to provide a relative precision of  $10^{-6}$ . A special treatment

## 6.1. Confirming the collisionless instability

for  $\beta = 0$  is required, as then the special solution of  $\bar{A}_{\parallel} = 0$  holds from the eigenmode equation (5.41) and the tearing boundary condition in (3.35), which however conflicts with the discrete boundary condition in (4.10) at  $\bar{A}_{\parallel}(\bar{x} = 0)$  for the  $\beta \neq 0$  case.

The calculation results are presented in figure (6.1), which provides the mode frequency and growth rate as functions of collision frequency. The parameters are kept the same as for the slab MTM results in figure (4.2), in which the GS2 adopts the default Lorentz collision model. The electromagnetic model matches with GS2 to a good extent and also confirms the instability drive from the electron temperature gradient. Both show that this collisionless instability tends to be stabilised by collisions. The deviation between the electromagnetic model and GS2 increase with the collision frequency; the reason for this difference are to be discussed in Section 6.3. One phenomenon to note here is that the GS2 result switches to a slightly different branch at  $\nu_{th}/\omega_{*e} = 1.0$  when  $\eta_e = 5.0$  and  $\nu_{th}/\omega_{*e} = 0.7$  when  $\eta_e = 7.0$ , as indicated by the jump in frequency<sup>1</sup>. However, unlike the intrinsically different physics mode change as investigated in Section 4.2.1, the branches here are actually different orders of harmonic (see Section 6.1.3) of the same eigenmode equations. Figure (6.2) shows the difference in mode structures at different harmonics at  $\nu_{th}/\omega_{*e} = 0.1$ ,  $\eta_e = 5.0$  and  $\nu_{th}/\omega_{*e} = 1.0$ ,  $\eta_e = 5.0$ , where in the higher order harmonic, the mode has more fine structures. Different from GS2, our numerical code by default calculates the eigenmodes having the same order of harmonic.

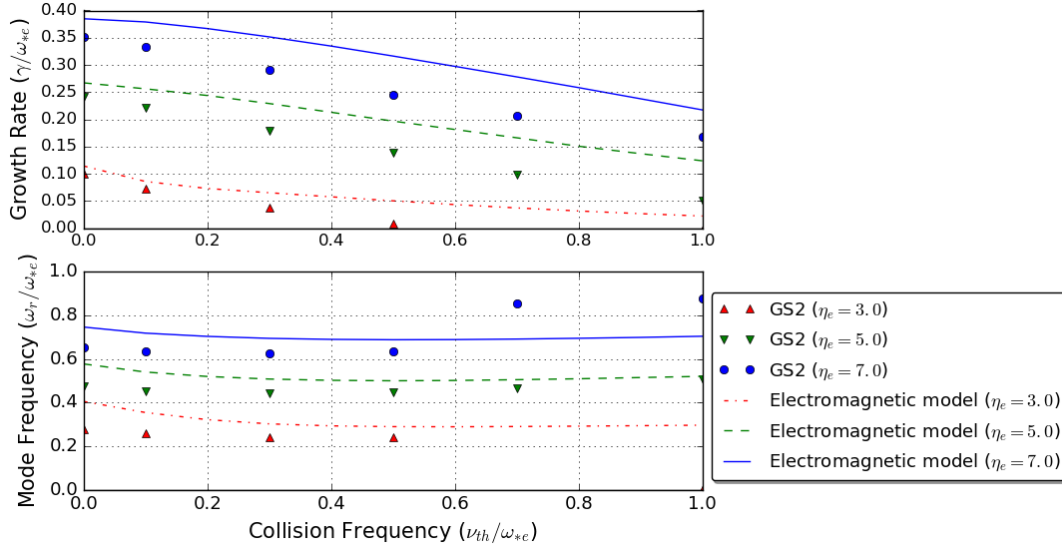


**Figure 6.1:** The benchmark for eigenvalue  $\omega$  as a function of collision frequency between the electromagnetic model and GS2. The physics parameters are kept the same as in figure (4.2), which are  $\beta = 0.005$ ,  $\epsilon = 0.05$  and  $k_y \rho_i = 0.3$  for GS2 simulations.

<sup>1</sup>As a time-dependent code, GS2 delivers the most unstable mode.

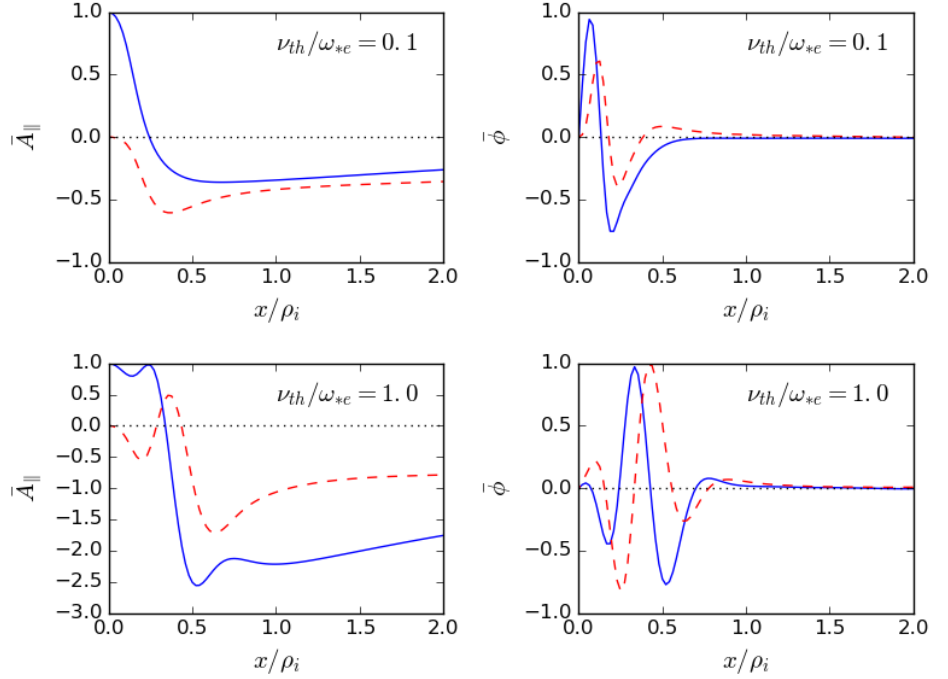


**Figure 6.2:** The mode structures of two harmonics in GS2 simulations of the collisionless instability. Samples taken from  $\eta_e = 5.0$  in figure (6.1), the top panels with  $\nu_{th}/\omega_{*e} = 0.1$  have a lower order of harmonic than the bottom panels with  $\nu_{th}/\omega_{*e} = 1.0$ . The real and imaginary parts of the fields are shown with blue solid lines and red dashed lines, respectively. The mode structures for  $\nu_{th}/\omega_{*e} = 0$  can be found in figure (4.3).

### 6.1.1 Validation for the small binormal wavenumber condition

Both our models have dropped the binormal wavenumber  $k_y$  in their coefficients due to the  $k_y \ll k_x$  condition applied. In other words, when the eigenmode  $\omega$  is normalised to  $\omega_{*e}$ , it does not vary with  $k_y$ . (Note again that  $\omega_{*e} = k_y v_e \rho_e / 2L_n$ .) This can be confirmed in GS2 simulations. As shown in figure (6.3), the normalised mode frequency and growth rate are constant with respect to  $k_y$ . This also infers that the collisionless mode has a linear dispersion relation with respect to  $k_y$ , which agrees with the slab ETG characteristics [55, 59, 103].

### 6.1.2 Validation for the electrostatic limit

We now benchmark both electromagnetic and electrostatic models at various plasma beta ( $\beta = 0$  for the electrostatic model). Figure (6.4) shows the mode growth rate and frequency as functions of  $\beta$  in electromagnetic and electrostatic models at zero collision frequency. The result at  $\beta = 0$  is the same whether using the electromagnetic model or electrostatic model, which confirms the fundamental ETG nature of this mode. The

### 6.1. Confirming the collisionless instability

GS2 results from figure (4.12) are also plotted in the figure. The electromagnetic model shows a trend that is consistent with GS2, though the difference between the two models becomes larger when plasma beta increases. This difference is partly due to the fact that with higher plasma beta the eigenmode with a higher harmonic becomes more unstable

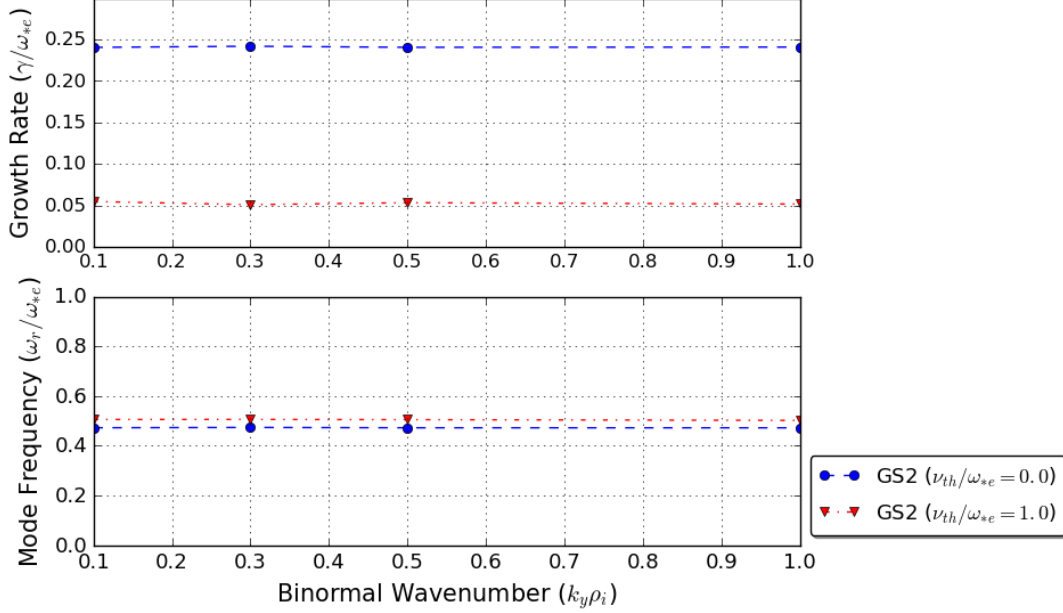


**Figure 6.3:** The validation for the small  $k_y$  condition with GS2 simulations. The normalised mode frequency and growth rate does not vary with  $k_y$ . The parameters for this graph include  $\eta_e = 5.0$ ,  $\epsilon = 0.05$ ,  $\beta = 0.005$ .

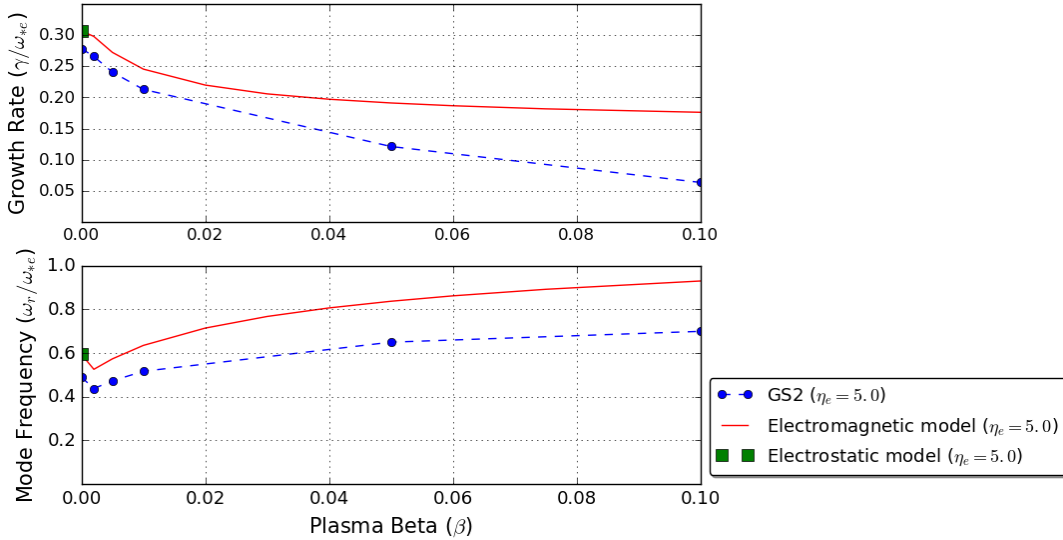


**Figure 6.4:** The comparison of the impact of plasma beta in the electromagnetic model and GS2. The parameters are kept the same as in figure (4.12), which are  $\eta_e = 5.0$ ,  $\nu_{th}/\omega_{*e} = 0.0$ ,  $\epsilon = 0.05$  and  $k_y\rho_i = 0.3$  for GS2 simulations. The data points at  $\beta = 0$  matches well with the electrostatic model.

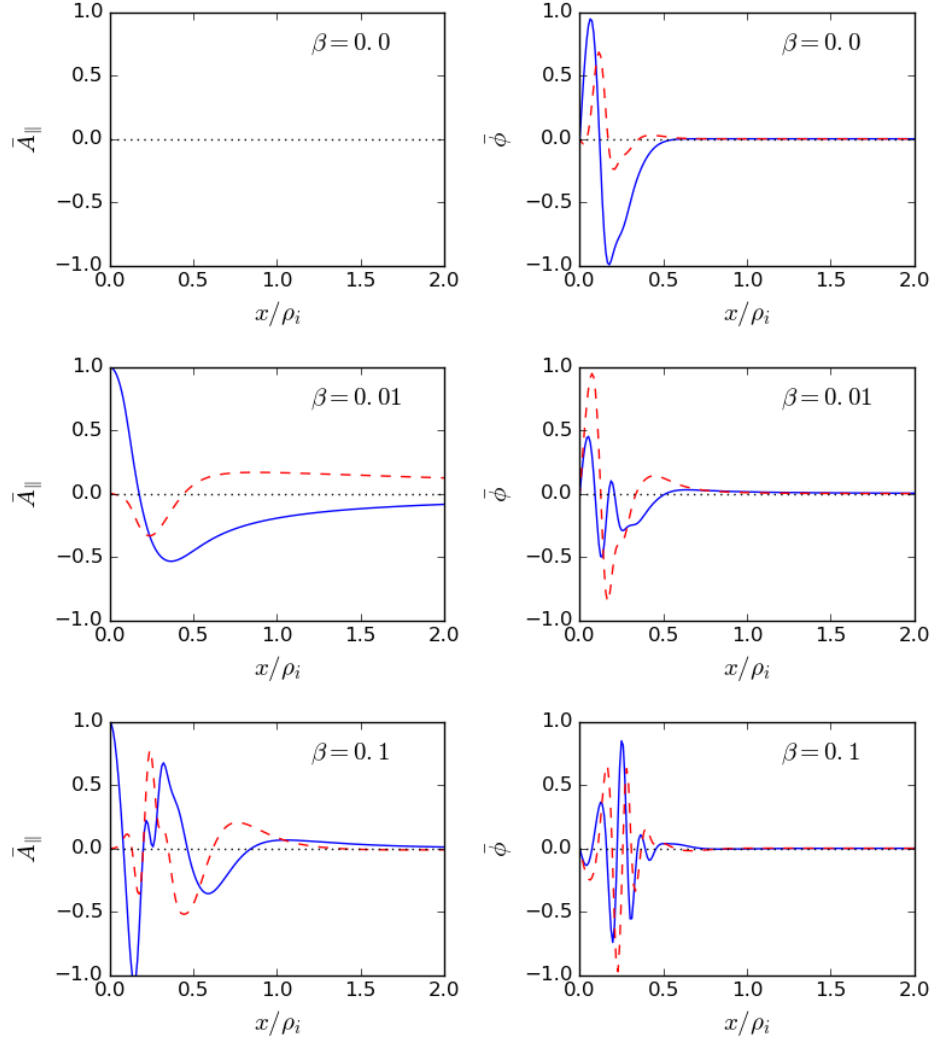


**Figure 6.5:** The mode structures of the most unstable harmonic in GS2 simulations at  $\beta = 0, 0.01$  and  $0.1$  in figure (6.4), in which  $\beta = 0$  corresponds to the electrostatic case where magnetic vector potential is not relevant. The real and imaginary parts of the fields are shown with blue solid lines and red dashed lines, respectively. The mode structures for  $\beta = 0.005$  can be found in figure (4.3).

and is therefore picked out in GS2. Figure (6.5) shows the change in mode structure with varying plasma beta, where more fine structures can be seen as  $\beta$  increases.

### 6.1.3 The eigenmode harmonic series

We have shown that this collisionless micro-scale tearing parity mode has the nature of ETG modes, though usually ETG modes are associated with twisting parity. In practice, if the boundary condition is not restricted, mathematically one eigenmode problem in general will have a family of harmonic solutions alternating between twisting and tearing

parity. In other words, even if the twisting parity eigenmode is the fundamental harmonic, there might also be higher orders of harmonic with tearing parity. These harmonics do not conflict with each other, and sometimes they can co-exist. Indeed, there actually is no physical or mathematical reason for the fundamental harmonic to always be the most unstable one. The phenomenon that higher order harmonics can be more unstable have been previously reported for the ITG mode [111, 112], ETG mode [113, 114] and ballooning mode [115, 116]. High harmonics excitation, parity mixture and transition under certain scenarios can be found in [117, 118].

In our models, the different harmonics can be found numerically using the contour method described in Section 4.1. Figure (6.6) shows the contour plot calculated with the electrostatic model. The cross points of blue lines ( $\text{Re}(\mathbf{L}) = 0$ ) and red lines ( $\text{Im}(\mathbf{L}) = 0$ ) are at the eigenvalue  $\omega$  of different harmonics, in which those solutions indicated with green dots are found to have tearing parity. Note the rapidly changing  $\mathbf{L}$  values around yellow dots - these have eigenmodes with twisting parity, and can be confirmed by solving the eigenmode equations with the twisting boundary condition. These twisting solutions are allowed in our eigenmode equations, and should be part of the harmonic set, because in the derivation we do not take any assumptions on the parity. The only restriction for the parity comes from the boundary conditions imposed for the calculation, such that the

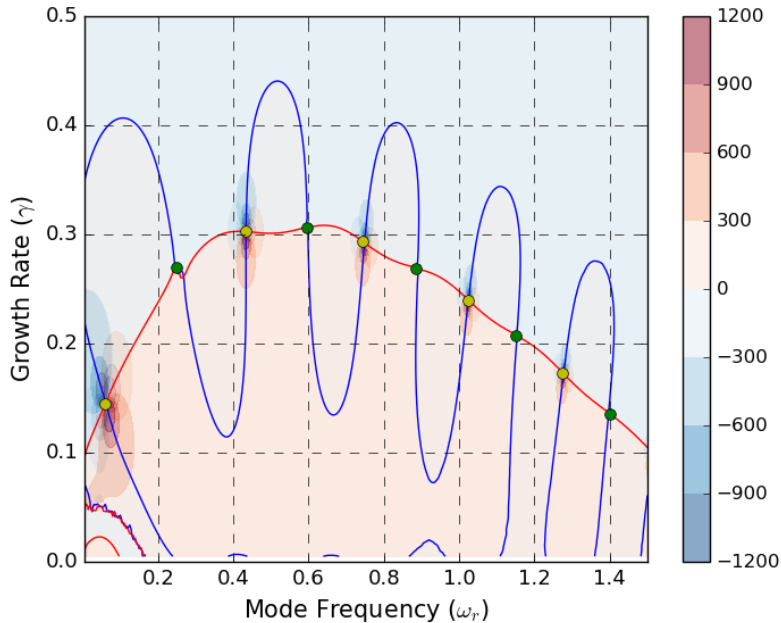


**Figure 6.6:** The contour plot of  $\omega$  is calculated from the electrostatic model at  $\eta_e = 5.0$ . The cross points of blue and red curves are at  $\omega$  eigenvalues.

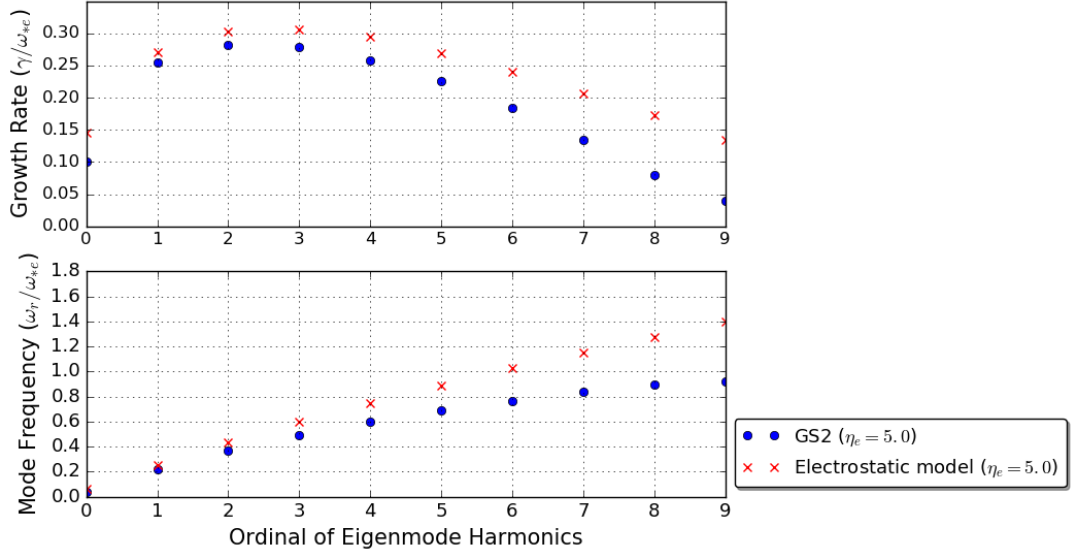


**Figure 6.7:** The growth rate and mode frequency of different harmonics calculated from the electrostatic model and GS2. In this figure,  $\nu_{th}/\omega_{*e} = 0.0$ ,  $\eta_e = 5.0$ ,  $\beta = 0.0$ ,  $\epsilon = 0.05$  and  $k_y \rho_i = 0.3$  for GS2 simulations.

twisting parity eigenmodes are found under the boundary condition

$$|\phi|, |A_{\parallel}| \rightarrow 0 \text{ as } |x| \rightarrow \infty, \quad A_{\parallel}(0) = 0, \quad \left. \frac{\partial \phi}{\partial x} \right|_{x=0} = 0. \quad (6.4)$$

Therefore, the odd harmonics are tearing parity modes while the even harmonics are twisting.

GS2 can also calculate our different harmonics if the code is used with its eigensolver setting. Extracting the harmonics calculated from GS2 and our models, we can compare them. Figure (6.7) shows in the electrostatic collisionless limit the different harmonic eigenmodes calculated by the electrostatic model and GS2. It can be seen that the most unstable eigenmode in this case is the third harmonic. This is a tearing parity mode even though the equation contains only ETG physics. In figure (6.1), the results from our electromagnetic model are consistent with the third harmonic, while the GS2 data points where the frequency jumps actually corresponds to the fifth harmonic.

## 6.2 Magnetic islands in the collisionless model

Although the underlying mechanism behind this small-scale collisionless tearing parity mode in slab geometry has been shown to come from ETG modes, we demonstrate that this mode is still capable of forming magnetic islands. This mechanism can be explained by the electron inertia - it is also the rationality behind the consideration for the electron

FLR effects. The structure of a magnetic island can be calculated from the magnetic vector potential  $A_{\parallel}$  by taking the contours of flux surface

$$\psi(x, y) = \frac{B_0 x^2}{2L_s} + \text{Re}(A_{\parallel} \cdot e^{ik_y y}). \quad (6.5)$$

A set of necessary but not sufficient conditions<sup>2</sup> for a magnetic island surface is

$$\left\{ \begin{array}{l} \frac{\partial \psi}{\partial x} \Big|_{x=0, y=y_0} = 0, \\ \frac{\partial \psi}{\partial y} \Big|_{x=x_w, y=y_w} = 0, \\ \psi(0, y_0) = \psi(x_w, y_w). \end{array} \right. \quad (6.6)$$

$$\left\{ \begin{array}{l} \frac{\partial \psi}{\partial y} \Big|_{x=x_w, y=y_w} = 0, \\ \psi(0, y_0) = \psi(x_w, y_w). \end{array} \right. \quad (6.7)$$

$$\psi(0, y_0) = \psi(x_w, y_w). \quad (6.8)$$

The island width  $w$  is given by the maximum of  $x_w$  which depends on the magnitude and the profile of  $A_{\parallel}$ . As in our linear model the amplitude of  $A_{\parallel}$  is arbitrary, the width of the island is actually undetermined.

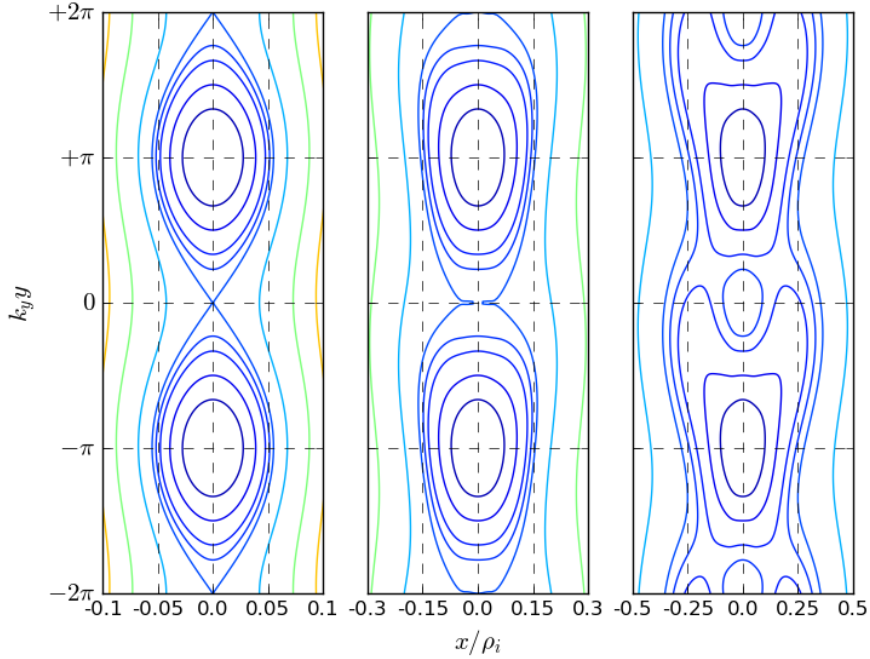


**Figure 6.8:** The magnetic islands structure evolution calculated by the electromagnetic model with  $\eta_e = 5.0$ ,  $\nu_{th}/\omega_e = 0.0$ ,  $\beta = 0.005$  and  $\epsilon = 0.05$ . The amplitudes of  $A_{\parallel}$  in the centre panel and the right-hand panel is 12 times larger and 60 times large, respectively, than that of the left-hand panel; the size of magnetic islands accordingly grows from order of  $\rho_e$  to  $\rho_i$  and a subsidiary island forms near original X-points.

<sup>2</sup>Equation (6.6) is trivial, noticing the boundary condition  $A'_{\parallel}(0) = 0$ .

Figure (6.8) demonstrates the magnetic island structure for the collisionless condition in the electromagnetic model. The three panels show the evolution of the island shape with growing island width. In the left-hand panel the width is of the order of electron gyroradius  $\rho_e$  while to the right-hand panels it grows to the order of ion gyroradius  $\rho_i$ . The left-hand panel corresponds to the classic island structure which occurs when  $A_{\parallel}$  is sufficiently small that its radial variation across the island can be neglected. Sometimes this is called the “constant- $\psi$ ” approximation. Under this approximation,  $A_{\parallel}(0) \approx A_{\parallel}(x_w) \approx \text{Re}(A_{\parallel}(0))$ , so the island width  $w$  is proportional to the square root of the  $A_{\parallel}$  magnitude

$$w \approx \sqrt{\frac{4L_s}{B_0} A_{\parallel}(0)}. \quad (6.9)$$

However, as  $A_{\parallel}$  increases in the centre and right-hand panels, from a certain point its radial variation across the island cannot be neglected. This results in the more complex structures shown in the figure, where the disconnection of the island separatrix happens and subsidiary islands can arise near the X-points. The island width can still be found through equations (6.7) and (6.8) provided the profile of  $A_{\parallel}$  is known, but usually there is not a general analytic expression.

Nevertheless, magnetic islands short circuit the flux surfaces at two sides, which as a consequence can increase radial transport. When a tearing parity eigenmode exists, even if it is not the most unstable eigenmode linearly, it is still possible that such a mode might provide a background degradation to the confinement nonlinearly. Although we must acknowledge that the order of  $k_x \rho_e$  and  $\beta$  in our research implies that the level of transport might be moderate [65, 119, 120]. How quantitatively this collisionless magnetic island affects the particle and heat transport is to be answered in future work.

### 6.3 The limitation of our collisionless models

Our models for the collisionless micro-scale tearing parity mode have been shown to present a good agreement with GS2 full gyrokinetic simulation results, but the agreement weakens at relatively higher collision frequency and at higher orders of eigenmode harmonic. This is due to two main simplifications in our derivation: the reduced collision operator and the limited order of expansions.

As mentioned in Section 4.4, the *lorentz* option in GS2 contains not only the full Lorentz collision operator in equation (4.12), but also a correction term regarding the flow velocity of the background, whose magnitude is proportional to the collision frequency (see equation (28) in [82]). Although here we do not discuss the form of this correction term

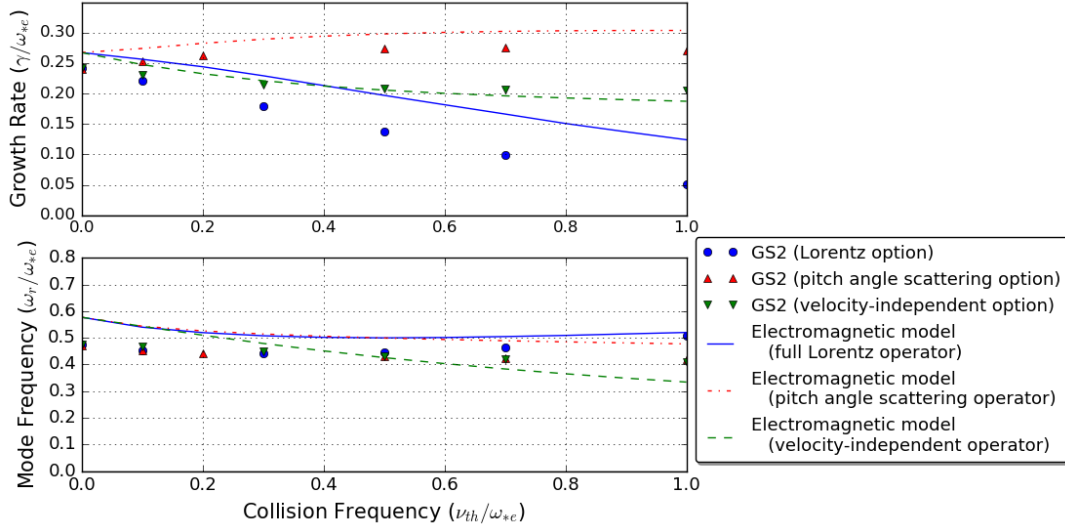


**Figure 6.9:** The benchmark for the collision operators between GS2 and the electromagnetic model. Three forms of the collision operator are shown in the figure. The related physics parameters are kept the same as in figure (4.11).

or re-derive the eigenmode equations including this term, we can estimate the impact of it by comparing the three different collision options as shown in figure (6.9) in GS2 and in our electromagnetic model. Both the *lorentz* option and the pitch angle scattering option in GS2 contains this flow correction term; however, it is turned off in the velocity-independent option. In our electromagnetic model, taking the matrix  $\mathbf{P}$  defined in equation (5.28) being zero reduces to the pitch angle collision operator; further taking  $\nu = \nu_{th}$  corresponds to the GS2 velocity-independent option. As shown in the figure, all three cases show good agreement and the distinguishable trend. Besides, the velocity-independent option, as the most alike model between GS2 and our electromagnetic model, matches better in the growth rate than the other two. The result differences using the other two options increases as the collision frequency rises, which agrees with the description of the flow correction term. Nevertheless, this concludes that the Lorentz operator contains the most important physics relevant to our study.

The limited expansion order leads to the discrepancy for higher harmonics. In our derivation, we expand the Bessel function to the second order only, and we neglect the higher order differential of the perturbed distribution function. This naturally loses information from higher harmonic components, and thus reduces the ability to capture more fine structures. In GS2, a full Bessel function is kept throughout the numerical calculation. The analytic derivation without expanding the Bessel function is needed for a more accurate model; however it faces mathematical challenges regarding a coupling that associates the FLR effects with pitch angle scattering. The detail is presented in Appendix B.

# Chapter 7

## Conclusions and future work

### 7.1 The physics of the collisionless micro-scale tearing mode in slab geometry

MTMs are one of the concerns for the effectiveness of confinement in MCF. They form fine scale magnetic islands thus enhancing the unwanted radial thermal transport. In this thesis, we demonstrate a collisionless physics mechanism that drives an ETG-based micro-scale tearing parity mode, which leads to the same consequence of magnetic islands as that of MTM. In slab geometry, this collisionless micro-scale tearing parity mode is also driven by the electron temperature gradient, but the radial wavenumber of this mode is much larger than the binormal wavenumber. Therefore FLR effects from electrons play an important role in the drive mechanism. The collision frequency and plasma beta tend to stabilise this mode, thus there may exist a window where both conventional MTMs and this collisionless micro-scale tearing parity mode are stable.

In numerical simulations, the large radial wavenumber poses difficulties to resolve this mode. A large Fourier space simulation domain and a fine resolution are required. This creates an extreme challenge for nonlinear simulations for the future work because the memory space is limited even with high performance supercomputers. Therefore interactions between this mode and others can be hard to study.

Using analytic gyrokinetic theory, we develop an electrostatic model and an electromagnetic model to interpret the physics of the drive mechanism. The electrostatic model proves the ETG nature of this mode, and demonstrates that FLR effects affect this mode through a series of plasma dispersion relation. The electromagnetic model can describe the influence of collision frequency and plasma beta, but the expression is in a complica-

ated matrix form, which disadvantages the calculation. Further simplification is needed to give a better physics interpretation and benefit to understand the impact of this mode in MCF. There is still more work in improving these models.

## 7.2 Extending to toroidal geometry

The models developed in this thesis are in slab geometry. To apply to real tokamaks, a toroidal model is necessary. In toroidal geometry, the drift term  $\mathbf{v}_D \cdot \nabla g$  in the gyrokinetic equation (3.10) is non-zero due to the curvature, which introduces a further expansion in  $g$  in toroidal direction; besides, the magnetic field along the parallel direction is non-constant due to the poloidal pathway of field lines, which causes different dynamics in trapped and passing electrons. Figures (7.1) and (7.2) show preliminary linear GS2 simulation results in a cylindrical geometry. Here, the cylindrical geometry can be regarded as a transition between slab and toroidal geometries. The curvature parameter in GS2 is normalised as  $\epsilon_L = 2L_s/R$ , in which  $R$  is the radius of the cylinder; slab geometry corresponds to  $\epsilon_L = 0$ . Both figures show that curvature acts as a strong driving parameter and that there exists two different branches of the mode at low or high curvature; the influence of electron FLR effects is shown to decrease when curvature increases. Considering

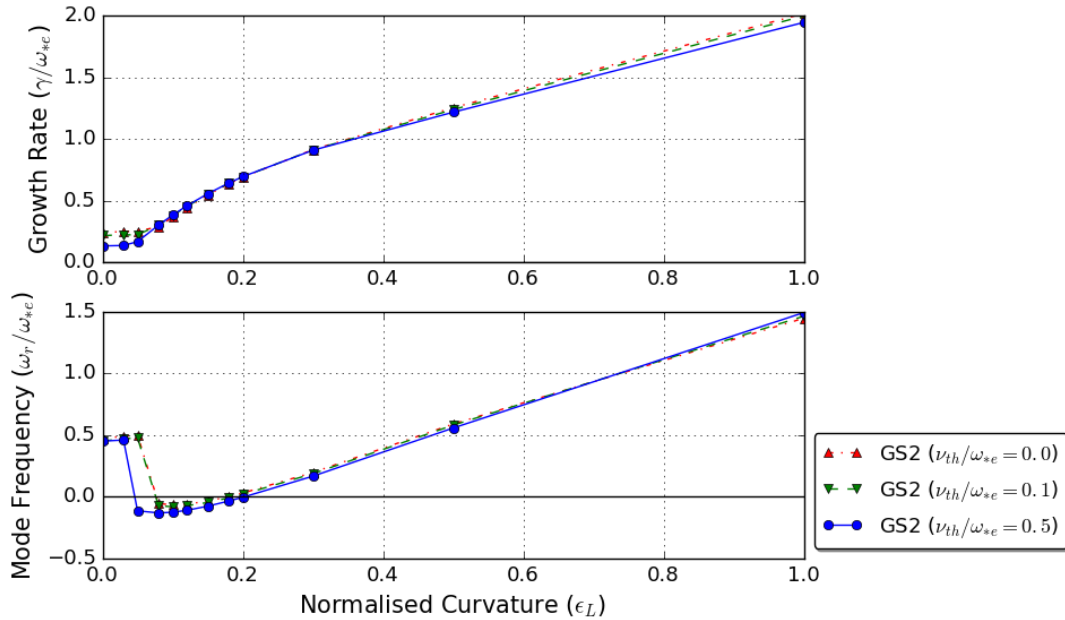


**Figure 7.1:** The GS2 simulations of the collisionless micro-scale tearing parity mode in cylindrical geometry against normalised curvature  $\epsilon_L$ . The red, green and blue colours are shown for  $\nu_{th}/\omega_{*e} = 0.0, 0.1, \text{ and } 0.5$ . Other physics parameters for this plot are  $k_y \rho_i = 0.3, \eta_e = 5.0, \epsilon = 0.05$  and  $\beta = 0.005$ . Note the frequency jump in the most unstable eigenmode at  $\epsilon_L \sim 0.05$ .

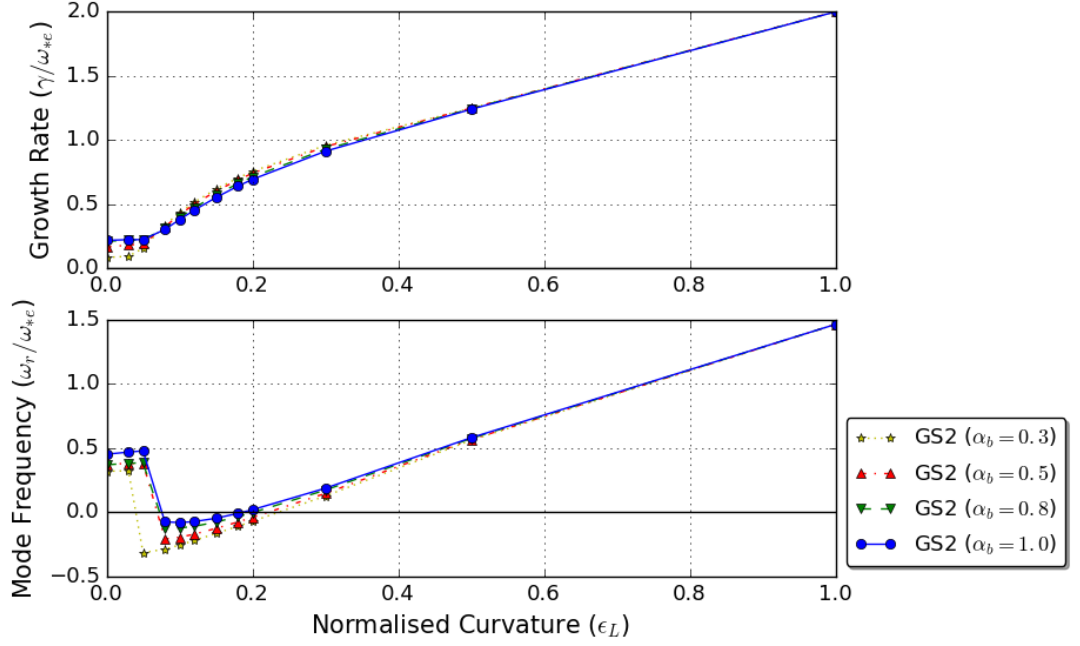


**Figure 7.2:** The GS2 simulations showing the impact of the Bessel factor  $\alpha_b$  on this collisionless micro-scale tearing parity mode in cylindrical geometry for varying curvature,  $\epsilon_L$ . The yellow, red, green and blue colours are shown for  $\alpha_b = 0.3, 0.5, 0.8$  and  $1.0$ . Other physics parameters for this plot are  $k_y \rho_i = 0.3$ ,  $\nu_{th}/\omega_{*e} = 0.1$ ,  $\eta_e = 5.0$ ,  $\epsilon = 0.05$  and  $\beta = 0.005$ .

the ETG nature of the slab mode, this phenomenon matches with the slab and toroidal ETG transition and dominance studies in [103, 121]. However, further research is needed regarding the tearing parity and its impact.

In addition to geometry, nonlinear effects are also required in order to determine the amplitude of this mode. When including nonlinear terms, modes with different wavenumbers can interact with each other. As a result, some modes will saturate while others may become more unstable. Modes with widely separated scales can also significantly couple together [104], which introduces further challenges in simulations. On the other hand, in collisionless conditions the fluctuating distribution function may not be a Maxwellian. Determine amplitude of the mode also helps better understanding and evaluating the critical threshold parameters for the unstable range.



# Appendix A

## Auxiliary derivations

### A.1 Lagrangian in single particle motion

As shown in figure (2.2), the particle's position is  $\mathbf{r} + \boldsymbol{\rho}_L$ , in which  $\mathbf{r}$  is the guiding centre's position. Using the dot notation above a variable to denote the time derivative,  $\dot{\mathbf{r}}$  is the motion of the guiding centre and  $\dot{\boldsymbol{\rho}}_L$  is the gyration component. Therefore,  $\dot{\mathbf{r}} \cdot \mathbf{b}$  is the parallel motion along the magnetic field line and  $-(\dot{\mathbf{r}} \times \mathbf{b}) \times \mathbf{b}$  is the drift motion perpendicular to the field line.

When the spatial variation of the magnetic field is slow compared with gyroradius, [31] gives an expression for the guiding centre system's Lagrangian as

$$\mathcal{L}(\mathbf{r}, v_{\parallel}, \mu, \theta, \dot{\mathbf{r}}, v_{\parallel}, \dot{\mu}, \dot{\theta}; t) = (mv_{\parallel}\mathbf{b} + q\mathbf{A}) \cdot \dot{\mathbf{r}} + \frac{m}{q}\mu\dot{\theta} - q\Phi - \mu B - \frac{1}{2}mv_{\parallel}^2, \quad (\text{A.1})$$

in which  $t$  is time;  $\theta = \theta(t)$  is the gyrophase angle of the particle; magnetic vector potential  $\mathbf{A} = \mathbf{A}(\mathbf{r}, t)$ , electric potential  $\Phi = \Phi(\mathbf{r}, t)$ , unit direction vector  $\mathbf{b} = \mathbf{B}/B = \mathbf{b}(\mathbf{r}, t)$  and magnetic field strength  $B = B(\mathbf{r}, t)$  are all functions of both  $\mathbf{r}$  and  $t$ . Therefore, the Lagrangian equations for the four generalised coordinates  $\mathbf{r}$ ,  $v_{\parallel}$ ,  $\mu$  and  $\theta$  give

$$\frac{d}{dt} \left( \frac{\partial \mathcal{L}}{\partial \dot{\mathbf{r}}} \right) - \frac{\partial \mathcal{L}}{\partial \mathbf{r}} = 0 \quad \Longrightarrow \quad \dot{\mathbf{r}} \times \mathbf{B} + \mathbf{E} - \frac{m}{q} \left( v_{\parallel} \dot{\mathbf{b}} + v_{\parallel} \dot{\mathbf{b}} + \frac{\mu}{m} \nabla B \right) = 0, \quad (\text{A.2})$$

$$\frac{d}{dt} \left( \frac{\partial \mathcal{L}}{\partial v_{\parallel}} \right) - \frac{\partial \mathcal{L}}{\partial v_{\parallel}} = 0 \quad \Longrightarrow \quad v_{\parallel} = \dot{\mathbf{r}} \cdot \mathbf{b}, \quad (\text{A.3})$$

$$\frac{d}{dt} \left( \frac{\partial \mathcal{L}}{\partial \dot{\mu}} \right) - \frac{\partial \mathcal{L}}{\partial \mu} = 0 \quad \Longrightarrow \quad \dot{\theta} = \frac{qB}{m}, \quad (\text{A.4})$$

$$\frac{d}{dt} \left( \frac{\partial \mathcal{L}}{\partial \dot{\theta}} \right) - \frac{\partial \mathcal{L}}{\partial \theta} = 0 \quad \Longrightarrow \quad \dot{\mu} = 0. \quad (\text{A.5})$$

Equations (A.3) and (A.4) are trivial. Equation (A.5) proves that the modulus of the magnetic motion  $\mu = |\boldsymbol{\mu}| = mv_{\perp}^2/2B$  is an adiabatic invariant. The dot product and cross product for equation (A.2) with regard to  $\mathbf{B}$  result in equations (2.9) and (2.12), respectively. Here, we do not need to assume  $dv_{\parallel}/dt \ll |d\mathbf{v}_{\perp}/dt|$  as we did in Section 2.1.

## A.2 Bessel functions from gyroaveraging

In the guiding centre coordinates described in Section 3.1, basis vectors  $\mathbf{e}_1$  and  $\mathbf{e}_2$  can be chosen as  $\mathbf{e}_1 = \mathbf{k}_{\perp}/k_{\perp}$  and  $\mathbf{e}_2 = \mathbf{b} \times \mathbf{k}_{\perp}/k_{\perp}$ . The gyroradius and perpendicular velocity can be expressed in  $\{\mathbf{e}_1, \mathbf{e}_2\}$  as  $\boldsymbol{\rho}_L = \rho_L(\cos \alpha, \sin \alpha)$  and  $\mathbf{v}_{\perp} = v_{\perp}(\sin \alpha, -\cos \alpha)$ , with  $\alpha$  being the gyroangle. Note the minus sign in the velocity expression. This is due to that the physics nature of gyromotion direction, considering the sign of charge, is against the mathematically defined positive angular direction (anti-clockwise). Therefore, equations (3.12), (3.13) and (3.14) can be derived as follows.

$$\begin{aligned} \langle e^{i\mathbf{k}_{\perp} \cdot \boldsymbol{\rho}_L} \rangle &= \frac{1}{2\pi} \int_0^{2\pi} e^{ik_{\perp}\rho_L \cos \alpha} d\alpha \\ &= \frac{1}{\pi} \int_0^{\pi} e^{ik_{\perp}\rho_L \cos \alpha} d\alpha \\ &= J_0(k_{\perp}\rho_L). \end{aligned} \tag{A.6}$$

$$\begin{aligned} \langle \boldsymbol{\rho}_L e^{i\mathbf{k}_{\perp} \cdot \boldsymbol{\rho}_L} \rangle &= \frac{\rho_L}{2\pi} \int_0^{2\pi} \left( \frac{\mathbf{k}_{\perp}}{k_{\perp}} \cos \alpha + \frac{\mathbf{b} \times \mathbf{k}_{\perp}}{k_{\perp}} \sin \alpha \right) e^{ik_{\perp}\rho_L \cos \alpha} d\alpha \\ &= i\rho_L \frac{\mathbf{k}_{\perp}}{k_{\perp}} \cdot \frac{-i}{\pi} \int_0^{\pi} e^{ik_{\perp}\rho_L \cos \alpha} \cos \alpha d\alpha \\ &= i\rho_L J_1(k_{\perp}\rho_L) \frac{\mathbf{k}_{\perp}}{k_{\perp}}. \end{aligned} \tag{A.7}$$

$$\begin{aligned} \langle \mathbf{v}_{\perp} e^{i\mathbf{k}_{\perp} \cdot \boldsymbol{\rho}_L} \rangle &= \frac{v_{\perp}}{2\pi} \int_0^{2\pi} \left( \frac{\mathbf{k}_{\perp}}{k_{\perp}} \sin \alpha - \frac{\mathbf{b} \times \mathbf{k}_{\perp}}{k_{\perp}} \cos \alpha \right) e^{ik_{\perp}\rho_L \cos \alpha} d\alpha \\ &= iv_{\perp} \frac{\mathbf{k}_{\perp} \times \mathbf{b}}{k_{\perp}} \cdot \frac{-i}{\pi} \int_0^{\pi} e^{ik_{\perp}\rho_L \cos \alpha} \cos \alpha d\alpha \\ &= iv_{\perp} J_1(k_{\perp}\rho_L) \frac{\mathbf{k}_{\perp} \times \mathbf{b}}{k_{\perp}}. \end{aligned} \tag{A.8}$$

### A.3 Differential of the matrix product

The second order differential  $\partial^2 \mathbf{h} / \partial \bar{x}^2$  in equation (5.34) is derived from equation (5.31) as follows. Note that  $\partial \mathbf{P} / \partial \bar{x} = 0$  and  $\partial^2 \mathbf{M} / \partial \bar{x}^2 = 0$ .

Taking the first order differential of equation (5.31) gives

$$\frac{\partial \mathbf{M}}{\partial \bar{x}} \cdot \mathbf{h} + \mathbf{M} \cdot \frac{\partial \mathbf{h}}{\partial \bar{x}} - \mathbf{P} \cdot \frac{\partial^3 \mathbf{h}}{\partial \bar{x}^3} = K \frac{\partial \mathbf{D}}{\partial \bar{x}}. \quad (\text{A.9})$$

Substituting the expression of  $\mathbf{h}$  in equation (5.33) gives

$$\frac{\partial \mathbf{h}}{\partial \bar{x}} = K \mathbf{M}^{-1} \cdot \frac{\partial \mathbf{D}}{\partial \bar{x}} - K \mathbf{N}_1 \cdot \mathbf{D} - \mathbf{N}_1 \cdot \mathbf{P} \cdot \frac{\partial^2 \mathbf{h}}{\partial \bar{x}^2} + \mathbf{M}^{-1} \cdot \mathbf{P} \cdot \frac{\partial^3 \mathbf{h}}{\partial \bar{x}^3}, \quad (\text{A.10})$$

with  $\mathbf{N}_1$  defined in equation (5.35). The next order differential of equation (A.9) is

$$2 \frac{\partial \mathbf{M}}{\partial \bar{x}} \cdot \frac{\partial \mathbf{h}}{\partial \bar{x}} + \mathbf{M} \cdot \frac{\partial^2 \mathbf{h}}{\partial \bar{x}^2} - \mathbf{P} \cdot \frac{\partial^4 \mathbf{h}}{\partial \bar{x}^4} = K \frac{\partial^2 \mathbf{D}}{\partial \bar{x}^2}. \quad (\text{A.11})$$

Substituting equation (A.10) results in

$$\begin{aligned} (\mathbf{I} - 2\mathbf{N}_2 \cdot \mathbf{P}) \cdot \frac{\partial^2 \mathbf{h}}{\partial \bar{x}^2} &= K \mathbf{M}^{-1} \cdot \frac{\partial^2 \mathbf{D}}{\partial \bar{x}^2} - 2K \mathbf{N}_1 \cdot \frac{\partial \mathbf{D}}{\partial \bar{x}} + 2K \mathbf{N}_2 \cdot \mathbf{D} \\ &\quad - 2\mathbf{N}_1 \cdot \mathbf{P} \cdot \frac{\partial^3 \mathbf{h}}{\partial \bar{x}^3} + \mathbf{M}^{-1} \cdot \mathbf{P} \cdot \frac{\partial^4 \mathbf{h}}{\partial \bar{x}^4}, \end{aligned} \quad (\text{A.12})$$

in which  $\mathbf{N}_2$  is defined in equation (5.36). Assuming that  $\partial^3 \mathbf{h} / \partial \bar{x}^3$  and  $\partial^4 \mathbf{h} / \partial \bar{x}^4$  are all small gives the expression of  $\partial^2 \mathbf{h} / \partial \bar{x}^2$  in equation (5.34).



## Appendix B

# Complexity regarding a Bessel-Legendre integration for developing the electromagnetic model

In Chapter 5 we have introduced a derivation approach based on Taylor expansion of the Bessel function. In Chapter 6 we have shown that this expansion approach is less accurate for higher harmonics of the eigenmode because of neglect of higher orders of differentials. A complete gyrokinetic operator is preferred; however, now we address the challenges in deriving this full gyrokinetic operator, most of which come from the complexity in a Bessel-Legendre integral.

We start with the gyrokinetic equation (5.23), but employ only the pitch angle scattering operator in equation (3.15) for now. Apply the Legendre series and conducting the inverse Fourier transform, the equation without expanding the Bessel function becomes

$$\begin{aligned} & \frac{2}{2n+1} \left[ \left( \omega + \frac{iv}{2}n(n+1) \right) h_n - k_{\parallel}v \left( \frac{n}{2n-1}h_{n-1} + \frac{n+1}{2n+3}h_{n+1} \right) \right] \\ &= \frac{e}{T} f_M (\omega - \omega_{*e}^T) \\ & \quad \mathcal{F}^{-1} \left[ \hat{\phi}(k) T_n \left( \frac{kv}{\omega_{ce}} \right) - \frac{n}{2n+1} v \hat{A}_{\parallel}(k) T_{n-1} \left( \frac{kv}{\omega_{ce}} \right) - \frac{n+1}{2n+1} v \hat{A}_{\parallel}(k) T_{n+1} \left( \frac{kv}{\omega_{ce}} \right); x \right], \end{aligned} \tag{B.1}$$

in which  $\mathcal{F}^{-1}[\hat{f}(k); x]$  represents the inverse Fourier transform operation from  $\hat{f}(k)$  to

$f(x)$ , and  $T_n(k)$  is defined as

$$T_n(k) = \int_{-1}^1 J_0(k\sqrt{1-\xi^2})P_n(\xi) d\xi, \quad k, \xi \in \mathcal{R} \text{ and } n \in \mathcal{N}. \quad (\text{B.2})$$

It can be seen that  $T_n(k) = 0$  if  $n$  is an odd number. We write the inverse Fourier transform of  $T_n(k)$  as  $S_n(x)$

$$\begin{aligned} S_n(x) &= \mathcal{F}^{-1}[T_n(k); x] \\ &= \int_{-1}^1 \mathcal{F}^{-1}[J_0(k\sqrt{1-\xi^2}); x] P_n(\xi) d\xi \\ &= \frac{1}{\pi} \int_{-\sqrt{1-x^2}}^{\sqrt{1-x^2}} \frac{P_n(\xi)}{\sqrt{1-x^2-\xi^2}} d\xi, \quad (|x| < 1). \end{aligned} \quad (\text{B.3})$$

Here, the inverse transform of Bessel function  $J_0(k)$  is calculated using equation (6.677.2) in [84] as

$$\begin{aligned} \mathcal{F}^{-1}[J_0(k); x] &= \frac{1}{2\pi} \int_{-\infty}^{\infty} J_0(k)e^{ikx} dk \\ &= \frac{1}{\pi} \int_0^{\infty} J_0(k) \cos(kx) dk \\ &= \begin{cases} (1-x^2)^{-1/2} / \pi, & \text{for } |x| < 1, \\ 0, & \text{elsewhere.} \end{cases} \end{aligned} \quad (\text{B.4})$$

The scaling relation  $\mathcal{F}^{-1}[\hat{f}(ak); x] = f(x/a)/|a|$  is also applied. For a given small  $n$ , it may be possible to solve  $T_n(k)$  and  $S_n(x)$  to provide simple forms, for example,

$$T_0(k) = \frac{2 \sin k}{k}, \quad (\text{B.5})$$

$$S_0(x) = \begin{cases} 1, & \text{for } |x| < 1, \\ 0, & \text{elsewhere,} \end{cases} \quad (\text{B.6})$$

$$T_2(k) = \frac{3 \sin k}{k^3} - \frac{3 \cos k}{k^2} - \frac{\sin k}{k}, \quad (\text{B.7})$$

$$S_2(x) = \begin{cases} (1-3x^2)/4, & \text{for } |x| < 1, \\ 0, & \text{elsewhere.} \end{cases} \quad (\text{B.8})$$

Equations (6.517), (6.554.2) and (6.567.1) in [84] are used here in the simplification. The general expressions for  $T_n(k)$  or  $S_n(x)$  at any given  $n$  is still too complex to analyse and present here. However, they are required for the next step, which gives the first

challenge in deriving the eigenmode equations. For now, we keep the notations of  $T_n(k)$  and  $S_n(x)$ .

Equation (B.1) therefore can be written as

$$\begin{aligned} \text{RHS} = \frac{e}{T} f_M (\omega - \omega_{*e}^T) \omega_{ce} \left[ \frac{1}{|v|} \phi(x) \otimes S_n\left(\frac{\omega_{ce}}{v} x\right) \right. \\ \left. - \frac{n}{2n+1} \frac{v}{|v|} A_{\parallel}(x) \otimes S_{n-1}\left(\frac{\omega_{ce}}{v} x\right) - \frac{n+1}{2n+1} \frac{v}{|v|} A_{\parallel}(x) \otimes S_{n+1}\left(\frac{\omega_{ce}}{v} x\right) \right], \end{aligned} \quad (\text{B.9})$$

in which  $\otimes$  is the convolution operator<sup>1</sup>

$$F(x) \otimes S(ax) = \int_{-\infty}^{\infty} F(\lambda) S(a(x - \lambda)) d\lambda. \quad (\text{B.10})$$

Again, the extraction for lower  $n$  orders are simpler than higher ones. Considering the  $v > 0$  half of phase space provides

$$n = 0 : \quad \omega h_0 - \frac{k_{\parallel} v}{3} h_1 = \frac{e f_M}{T} (\omega - \omega_{*e}^T) \frac{\omega_{ce}}{2v} \int_{x-v/\omega_{ce}}^{x+v/\omega_{ce}} \phi(\lambda) d\lambda, \quad (\text{B.11})$$

$$\begin{aligned} n = 1 : \quad (\omega + i\nu) h_1 - k_{\parallel} v \left( h_0 + \frac{2}{5} h_2 \right) = -\frac{e f_M}{T} (\omega - \omega_{*e}^T) \frac{\omega_{ce}}{2v} \\ \left[ \frac{3v}{2} \left( 1 - \frac{\omega_{ce}^2 x^2}{v^2} \right) \int_{x-v/\omega_{ce}}^{x+v/\omega_{ce}} A_{\parallel}(\lambda) d\lambda \right. \\ \left. + 3v \frac{\omega_{ce}^2 x}{v^2} \int_{x-v/\omega_{ce}}^{x+v/\omega_{ce}} A_{\parallel}(\lambda) \lambda d\lambda - \frac{3v}{2} \frac{\omega_{ce}^2}{v^2} \int_{x-v/\omega_{ce}}^{x+v/\omega_{ce}} A_{\parallel}(\lambda) \lambda^2 d\lambda \right], \end{aligned} \quad (\text{B.12})$$

$$n \geq 2 : \quad \text{RHS} \neq 0. \quad (\text{B.13})$$

The coefficient  $\omega_{ce}/2v$  acts as the averaging factor, thus the integral gives the moments of the fields over  $(x-v/\omega_{ce}, x+v/\omega_{ce})$  range. Note that this  $v$  is expected to be absorbed into the integration over the velocity space with the distribution function to give the expressions for  $n$  and  $j_{\parallel}$  as in equations (3.32) and (3.30). However, the distribution functions  $\{h_n(x, v)\}$  require solving the recursive relation regarding  $n \geq 2$ , of which the right hand side is now an interlocked function series about the fields  $\phi(x)$  and  $A_{\parallel}(x)$ . This loses the effectiveness of the technique of the continued fraction in (3.28). As  $\phi(x)$  and  $A_{\parallel}(x)$  are now in an implicit form, the integral over  $v$  brings in the next level of complexity.

---

<sup>1</sup>Note the coefficient difference compared with the standard definition.

---

We can write the averaged momentum of the fields as  $\langle \phi \rangle$ ,  $\langle A_{\parallel} \rangle$ ,  $\langle A_{\parallel} x \rangle$ ,  $\langle A_{\parallel} x^2 \rangle$  and so on, thus the parallel electric field  $E_{\parallel}$  in equation (3.29) can be symbolically defined as  $E_{\parallel} = i\omega \langle A_{\parallel} \rangle - ik_{\parallel} \langle \phi \rangle = i\omega(A_{\parallel} + \psi_A) - ik(\phi + \psi_{\phi})$ , where  $\psi$  represents for the extra phase arising from the momentum average.

In the limit of ignoring FLR effects, which is equivalent to  $\omega_{ce} \rightarrow \infty$ , it holds that  $\lim_{\omega_{ce} \rightarrow \infty} T_0(kv/\omega_{ce}) = 2$  and  $\lim_{\omega_{ce} \rightarrow \infty} T_n(kv/\omega_{ce}) = 0$  for  $n \geq 2$ . One may conclude that equations (B.11), (B.12) and (B.13) reduce to the conventional theory (3.25), (3.26) and (3.27). However, they do not. The difference is arisen from the convolution step, which in some sense is related with a differential operation. A further picture for the impacts of FLR effects is to be understood.

The procedure above has already demonstrated the mathematical challenge in deriving the electromagnetic model. With the diffusion term in equation (4.12) included, the algebra becomes too heavy to analyse. Therefore, an approach based on the expansion of the Bessel function and the matrix operations is developed in Section 5.2.

# Glossary

ETG mode    Electron temperature gradient mode

FLR effects    Finite Larmor radius effects

ICF            Inertial confinement fusion

ITG mode    Ion temperature gradient mode

MCF            Magnetic confinement fusion

MTM            Microtearing mode



## References

- [1] Wikipedia contributors. Nuclear binding energy - Wikipedia, the free encyclopedia, 2020. Online [https://en.wikipedia.org/wiki/Nuclear\\_binding\\_energy](https://en.wikipedia.org/wiki/Nuclear_binding_energy); Image File Date/Time: 09:59 23 August 2019. [Cited on page 1]
- [2] IAEA Nuclear Data Services. Evaluated nuclear data file, 2020. Online <https://www-nds.iaea.org/exfor/endl.htm>; Database Version: ENDF/B-VIII.0. [Cited on pages 2 and 5]
- [3] United Nations Department of Economic and Social Affairs. 2019 energy statistics pocketbook, 2019. Online <https://unstats.un.org/unsd/energystats/pubs/documents/2019pb-web.pdf>; Series E No.2. [Cited on pages 2 and 3]
- [4] S. Shafiee and E. Topal. When will fossil fuel reserves be diminished? *Energy Policy*, 37(1):181, 2009. doi:[10.1016/j.enpol.2008.08.016](https://doi.org/10.1016/j.enpol.2008.08.016). [Cited on page 2]
- [5] S. Sorrell, J. Speirs, R. Bentley, A. Brandt, and R. Miller. Global oil depletion: A review of the evidence. *Energy Policy*, 38(9):5290, 2010. doi:[10.1016/j.enpol.2010.04.046](https://doi.org/10.1016/j.enpol.2010.04.046). [Cited on page 2]
- [6] Al. Valero and A. Valero. A prediction of the exergy loss of the world's mineral reserves in the 21st century. *Energy*, 36(4):1848, 2011. doi:[10.1016/j.energy.2010.02.041](https://doi.org/10.1016/j.energy.2010.02.041). [Cited on page 2]
- [7] A. Stips, D. Macias, C. Coughlan, E. Garcia-Gorriz, and X. S. Liang. On the causal structure between CO<sub>2</sub> and global temperature. *Scientific Reports*, 6:21691, 2016. doi:[10.1038/srep21691](https://doi.org/10.1038/srep21691). [Cited on page 2]
- [8] S. Solomon, G.-K. Plattner, R. Knutti, and P. Friedlingstein. Irreversible climate change due to carbon dioxide emissions. *Proceedings of the National Academy of Sciences*, 106(6):1704, 2009. doi:[10.1073/pnas.0812721106](https://doi.org/10.1073/pnas.0812721106). [Cited on page 2]

## References

---

- [9] A. A. Lacis, G. A. Schmidt, D. Rind, and R. A. Ruedy. Atmospheric CO<sub>2</sub>: Principal control knob governing earth's temperature. *Science*, 330 (6002):356, 2010. doi:[10.1126/science.1190653](https://doi.org/10.1126/science.1190653). Corrected on 18 March 2011 doi:[10.1126/science.331.6023.1387-b](https://doi.org/10.1126/science.331.6023.1387-b). [Cited on page 2]
- [10] T. Boden, G. Marland, and R. J. Andres. Global, regional, and national fossil-fuel CO<sub>2</sub> emissions (1751 - 2014) (v. 2017), 2017. doi:[10.3334/CDIAC/00001\\_V2017](https://doi.org/10.3334/CDIAC/00001_V2017). [Cited on pages 3 and 4]
- [11] NASA Goddard Institute for Space Studies. GISS surface temperature analysis (v4), 2020. Online [https://data.giss.nasa.gov/gistemp/graphs\\_v4](https://data.giss.nasa.gov/gistemp/graphs_v4); Updated monthly; Accessed on March 2020. [Cited on pages 3 and 4]
- [12] United Nations. The intergovernmental panel on climate change (webpage), 2020. Online <https://www.ipcc.ch>. [Cited on page 3]
- [13] NASA. Global climate change (webpage), 2020. Online <https://climate.nasa.gov>. [Cited on page 3]
- [14] Brookhaven National Laboratory. Nuclear database, 2020. Online <https://www.nndc.bnl.gov/nudat2>; Database Version: 2.8. [Cited on page 3]
- [15] United States Energy Information Administration. International energy outlook 2019, 2019. Online <https://www.eia.gov/outlooks/ieo/pdf/ieo2019.pdf>; Updated on 18 October 2019. [Cited on page 4]
- [16] K. S. Krane. *Introductory Nuclear Physics*. John Wiley & Sons, 1987. ISBN [9780471805533](https://www.isbn-international.org/product/9780471805533). [Cited on page 5]
- [17] I. Amdur, M. C. Kells, and D. E. Davenport. Collision cross sections of hydrogen and of deuterium. *The Journal of Chemical Physics*, 18(12):1676, 1950. doi:[10.1063/1.1747561](https://doi.org/10.1063/1.1747561). [Cited on page 6]
- [18] A. Kramida, Yu. Ralchenko, J. Reader, and NIST ASD Team. NIST atomic spectra database ionization energies form, 2019. Online <https://physics.nist.gov/PhysRefData/ASD/ionEnergy.html>; Database Version: 5.7.1. [Cited on page 6]
- [19] J. P. Freidberg. *Plasma Physics and Fusion Energy*. Cambridge University Press, 2007. ISBN 9780511755705. doi:[10.1017/CBO9780511755705](https://doi.org/10.1017/CBO9780511755705). [Cited on page 7]
- [20] ITER project. ITER webpage, 2020. Online <https://www.iter.org>. [Cited on page 9]

- [21] M. Laberge. Magnetized target fusion with a spherical tokamak. *Journal of Fusion Energy*, 38(1):199, 2018. doi:[10.1007/s10894-018-0180-3](https://doi.org/10.1007/s10894-018-0180-3). [Cited on page 9]
- [22] G. G. Dolgov-Saveliev, D. P. Ivanov, V. S. Mukhovatov, et al. Investigations of the stability and heating of plasmas in toroidal chambers. *Proceedings of Second United Nations International Conference on the Peaceful Use of Atomic Energy, Geneva*, 32:82, 1958. Online [https://www-naweb.iaea.org/napc/physics/2ndgenconf/data/Proceedings%201958/papers%20Vol32/Paper09\\_Vol32.pdf](https://www-naweb.iaea.org/napc/physics/2ndgenconf/data/Proceedings%201958/papers%20Vol32/Paper09_Vol32.pdf). [Cited on page 9]
- [23] S. V. Mirnov. Tokamak evolution and view to future. *Nuclear Fusion*, 59(1):015001, 2018. doi:[10.1088/1741-4326/aaee92](https://doi.org/10.1088/1741-4326/aaee92). [Cited on page 9]
- [24] L. Spitzer. The stellarator concept. *The Physics of Fluids*, 1(4):253, 1958. doi:[10.1063/1.1705883](https://doi.org/10.1063/1.1705883). [Cited on page 9]
- [25] T. Klinger, T. Andreeva, S. Bozhenkov, et al. Overview of first Wendelstein 7-X high-performance operation. *Nuclear Fusion*, 59(11):112004, 2019. doi:[10.1088/1741-4326/ab03a7](https://doi.org/10.1088/1741-4326/ab03a7). [Cited on page 9]
- [26] H. A. B. Bodin and A. A. Newton. Reversed-field-pinch research. *Nuclear Fusion*, 20(10):1255, 1980. doi:[10.1088/0029-5515/20/10/006](https://doi.org/10.1088/0029-5515/20/10/006). [Cited on page 9]
- [27] H. A. B. Bodin. The reversed field pinch. *Nuclear Fusion*, 30(9):1717, 1990. doi:[10.1088/0029-5515/30/9/005](https://doi.org/10.1088/0029-5515/30/9/005). [Cited on page 9]
- [28] P. Helander, C. D. Beidler, T. M. Bird, et al. Stellarator and tokamak plasmas: a comparison. *Plasma Physics and Controlled Fusion*, 54(12):124009, 2012. doi:[10.1088/0741-3335/54/12/124009](https://doi.org/10.1088/0741-3335/54/12/124009). [Cited on page 9]
- [29] Y. Xu. A general comparison between tokamak and stellarator plasmas. *Matter and Radiation at Extremes*, 1(4):192, 2016. doi:[10.1016/j.mre.2016.07.001](https://doi.org/10.1016/j.mre.2016.07.001). [Cited on page 9]
- [30] F. F. Chen. *Introduction to Plasma Physics and Controlled Fusion*. Springer International Publishing, 3 edition, 2016. ISBN 9783319223087. doi:[10.1007/978-3-319-22309-4](https://doi.org/10.1007/978-3-319-22309-4). [Cited on pages 11, 19, 20, 25, and 35]
- [31] R. G. Littlejohn. Variational principles of guiding centre motion. *Journal of Plasma Physics*, 29(1):111, 1983. doi:[10.1017/S002237780000060X](https://doi.org/10.1017/S002237780000060X). [Cited on pages 14 and 85]

## References

---

- [32] J. Wesson. *Tokamaks*. OUP Oxford, 4 edition, 2011. ISBN 9780199592234. [Cited on pages 18, 22, 23, 25, 27, 31, and 34]
- [33] L. Landau. On the vibrations of the electronic plasma. *Journal of Physics*, X(1): 25, 1946. doi:10.1016/B978-0-08-010586-4.50066-3. [Cited on page 19]
- [34] EUROfusion project. Tokamak illustration, 2020. Online <https://www.euro-fusion.org>; Previously known as EFDA-JET project. [Cited on pages 20 and 21]
- [35] C. E. Kessel. Bootstrap current in a tokamak. *Nuclear Fusion*, 34(9):1221, 1994. doi:10.1088/0029-5515/34/9/i04. [Cited on page 22]
- [36] M. Kikuchi and M. Azumi. Experimental evidence for the bootstrap current in a tokamak. *Plasma Physics and Controlled Fusion*, 37(11):1215, 1995. doi:10.1088/0741-3335/37/11/003. [Cited on page 22]
- [37] J. P. Freidberg. *Ideal MHD*. Cambridge University Press, 2014. ISBN 9780511795046. doi:10.1017/CBO9780511795046. [Cited on page 22]
- [38] M. Kikuchi. Steady state tokamak reactor based on the bootstrap current. *Nuclear Fusion*, 30(2):265, 1990. doi:10.1088/0029-5515/30/2/006. [Cited on page 22]
- [39] V. D. Shafranov. Equilibrium of a toroidal plasma in a magnetic field. *Journal of Nuclear Energy. Part C, Plasma Physics, Accelerators, Thermonuclear Research*, 5(4):251, 1963. doi:10.1088/0368-3281/5/4/307. [Cited on page 23]
- [40] R. D. Hazeltine and J. D. Meiss. *Plasma Confinement*. Dover Publications, 2003. ISBN 9780486432427. [Cited on pages 23, 31, and 32]
- [41] E. S. Benilov and O. A. Power. A drift model of interchange instability. *Physics of Plasmas*, 14(8):082101, 2007. doi:10.1063/1.2752815. [Cited on page 24]
- [42] C. H. Ma and X. Q. Xu. Global kinetic ballooning mode simulations in BOUT++. *Nuclear Fusion*, 57(1):016002, 2017. doi:10.1088/0029-5515/57/1/016002. [Cited on page 24]
- [43] A. Fick. V. on liquid diffusion. *The London, Edinburgh, and Dublin Philosophical Magazine and Journal of Science*, 10(63):30, 1855. doi:10.1080/14786445508641925. [Cited on page 25]
- [44] F. L. Hinton and R. D. Hazeltine. Theory of plasma transport in toroidal confinement systems. *Reviews of Modern Physics*, 48(2):239, 1976. doi:10.1103/RevModPhys.48.239. [Cited on page 25]

- [45] R. S. Pease. The UK fusion programme. *Plasma Physics and Controlled Fusion*, 29(10B):1439, 1987. doi:[10.1088/0741-3335/29/10b/405](https://doi.org/10.1088/0741-3335/29/10b/405). [Cited on page 25]
- [46] T. Fülöp and P. Helander. Nonlinear neoclassical transport in toroidal edge plasmas. *Physics of Plasmas*, 8(7):3305, 2001. doi:[10.1063/1.1372179](https://doi.org/10.1063/1.1372179). [Cited on page 25]
- [47] F. L. Hinton, J. C. Wiley, D. F. Düchs, H. P. Furth, and P. H. Rutherford. Neoclassical transport in tokamaks in banana/plateau regimes. *Physical Review Letters*, 29:698, 1972. doi:[10.1103/PhysRevLett.29.698](https://doi.org/10.1103/PhysRevLett.29.698). [Cited on page 25]
- [48] S. Tsuji. Experimental scaling of particle confinement in tokamaks. *Fusion Engineering and Design*, 15(4):311, 1991. doi:[10.1016/0920-3796\(92\)90017-x](https://doi.org/10.1016/0920-3796(92)90017-x). [Cited on page 25]
- [49] S. S. Henderson, L. Garzotti, F. J. Casson, et al. Neoclassical and gyrokinetic analysis of time-dependent helium transport experiments on MAST. *Nuclear Fusion*, 54(9):093013, 2014. doi:[10.1088/0029-5515/54/9/093013](https://doi.org/10.1088/0029-5515/54/9/093013). [Cited on page 25]
- [50] J. W. Connor. Pressure gradient turbulent transport and collisionless reconnection. *Plasma Physics and Controlled Fusion*, 35(6):757, 1993. doi:[10.1088/0741-3335/35/6/009](https://doi.org/10.1088/0741-3335/35/6/009). [Cited on page 25]
- [51] A. I. Smolyakov. Nonlinear evolution of tearing modes in inhomogeneous plasmas. *Plasma Physics and Controlled Fusion*, 35(6):657, 1993. doi:[10.1088/0741-3335/35/6/002](https://doi.org/10.1088/0741-3335/35/6/002). [Cited on page 25]
- [52] J. W. Connor and H. R. Wilson. Survey of theories of anomalous transport. *Plasma Physics and Controlled Fusion*, 36(5):719, 1994. doi:[10.1088/0741-3335/36/5/002](https://doi.org/10.1088/0741-3335/36/5/002). [Cited on page 25]
- [53] D. Dickinson. *Effects of profiles on microinstabilities in tokamaks*. PhD thesis, University of York, 2012. Online <https://etheses.whiterose.ac.uk/3331>. [Cited on pages 25, 31, 32, and 43]
- [54] S. C. Cowley, R. M. Kulsrud, and R. Sudan. Considerations of ion-temperature-gradient-driven turbulence. *Physics of Fluids B: Plasma Physics*, 3(10):2767, 1991. doi:[10.1063/1.859913](https://doi.org/10.1063/1.859913). [Cited on pages 25 and 64]
- [55] B. Coppi, M. N. Rosenbluth, and R. Z. Sagdeev. Instabilities due to temperature gradients in complex magnetic field configurations. *Physics of Fluids*, 10(3):582, 1967. doi:[10.1063/1.1762151](https://doi.org/10.1063/1.1762151). [Cited on pages 25 and 73]

- [56] P. N. Guzdar. Ion-temperature-gradient instability in toroidal plasmas. *Physics of Fluids*, 26(3):673, 1983. doi:[10.1063/1.864182](https://doi.org/10.1063/1.864182). [Cited on page 25]
- [57] D. L. Brower, W. A. Peebles, S. K. Kim, et al. Observation of a high-density ion mode in tokamak microturbulence. *Physical Review Letters*, 59:48, 1987. doi:[10.1103/PhysRevLett.59.48](https://doi.org/10.1103/PhysRevLett.59.48). [Cited on page 25]
- [58] M. Artun and W. M. Tang. Gyrokinetic analysis of ion temperature gradient modes in the presence of sheared flows. *Physics of Fluids B: Plasma Physics*, 4(5):1102, 1992. doi:[10.1063/1.860118](https://doi.org/10.1063/1.860118). [Cited on page 25]
- [59] W. Dorland, F. Jenko, M. Kotschenreuther, and B. N. Rogers. Electron temperature gradient turbulence. *Physical Review Letters*, 85(26 Pt 1):5579, 2000. doi:[10.1103/PhysRevLett.85.5579](https://doi.org/10.1103/PhysRevLett.85.5579). [Cited on pages 25 and 73]
- [60] F. Jenko, W. Dorland, and G. W. Hammett. Critical gradient formula for toroidal electron temperature gradient modes. *Physics of Plasmas*, 8(9):4096, 2001. doi:[10.1063/1.1391261](https://doi.org/10.1063/1.1391261). [Cited on page 25]
- [61] J. F. Drake and Y. C. Lee. Kinetic theory of tearing instabilities. *Physics of Fluids*, 20:1341, 1977. doi:[10.1063/1.862017](https://doi.org/10.1063/1.862017). [Cited on pages 28, 29, and 35]
- [62] H. Doerk. *Gyrokinetic Simulation of Microtearing Turbulence*. PhD thesis, University Ulm, 2012. [Cited on page 28]
- [63] N. T. Gladd, J. F. Drake, C. L. Chang, and C. S. Liu. Electron temperature gradient driven microtearing mode. *Physics of Fluids*, 23:1182, 1980. doi:[10.1063/1.863119](https://doi.org/10.1063/1.863119). [Cited on pages 28, 29, 35, 36, 40, 46, and 47]
- [64] D. Dickinson, C. M. Roach, S. Saarelma, et al. Microtearing modes at the top of the pedestal. *Plasma Physics and Controlled Fusion*, 55:074006, 2013. doi:[10.1088/0741-3335/55/7/074006](https://doi.org/10.1088/0741-3335/55/7/074006). [Cited on pages 28 and 29]
- [65] A. B. Rechester and M. N. Rosenbluth. Electron heat transport in a tokamak with destroyed magnetic surfaces. *Physical Review Letters*, 40:38, 1978. doi:[10.1103/PhysRevLett.40.38](https://doi.org/10.1103/PhysRevLett.40.38). [Cited on pages 28 and 79]
- [66] K. L. Wong, S. Kaye, D. R. Mikkelsen, et al. Microtearing instabilities and electron transport in the NSTX spherical tokamak. *Physical Review Letters*, 99:135003, 2007. doi:[10.1103/PhysRevLett.99.135003](https://doi.org/10.1103/PhysRevLett.99.135003). [Cited on page 28]

- [67] H. Doerk, F. Jenko, M. J. Pueschel, and D. R. Hatch. Gyrokinetic microtearing turbulence. *Physical Review Letters*, 106:155003, 2011. doi:[10.1103/PhysRevLett.106.155003](https://doi.org/10.1103/PhysRevLett.106.155003). [Cited on page 28]
- [68] W. Guttenfelder, J. Candy, S. M. Kaye, et al. Electromagnetic transport from microtearing mode turbulence. *Physical Review Letters*, 106:155004, 2011. doi:[10.1103/PhysRevLett.106.155004](https://doi.org/10.1103/PhysRevLett.106.155004). [Cited on page 28]
- [69] D. R. Hatch, M. Kotschenreuther, S. Mahajan, et al. Microtearing turbulence limiting the JET-ILW pedestal. *Nuclear Fusion*, 56(10), 2016. doi:[10.1088/0029-5515/56/10/104003](https://doi.org/10.1088/0029-5515/56/10/104003). [Cited on page 28]
- [70] R. D. Hazeltine, D. Dobrott, and T. S. Wang. Kinetic theory of tearing instability. *Physics of Fluids*, 18(12):1778, 1975. doi:[10.1063/1.861097](https://doi.org/10.1063/1.861097). [Cited on pages 28, 29, and 35]
- [71] D. J. Applegate, C. M. Roach, J. W. Connor, et al. Micro-tearing modes in the mega ampere spherical tokamak. *Plasma Physics and Controlled Fusion*, 49(8):1113, 2007. doi:[10.1088/0741-3335/49/8/001](https://doi.org/10.1088/0741-3335/49/8/001). [Cited on pages 29 and 57]
- [72] I. Predebon and F. Sattin. On the linear stability of collisionless microtearing modes. *Physics of Plasmas*, 20(4):040701, 2013. doi:[10.1063/1.4799980](https://doi.org/10.1063/1.4799980). [Cited on page 29]
- [73] A. K. Swamy, R. Ganesh, J. Chowdhury, et al. Global gyrokinetic stability of collisionless microtearing modes in large aspect ratio tokamaks. *Physics of Plasmas*, 21(8):082513, 2014. doi:[10.1063/1.4893314](https://doi.org/10.1063/1.4893314). [Cited on page 29]
- [74] S. Moradi, I. Pusztai, W. Guttenfelder, T. Fülöp, and A. Mollén. Microtearing modes in spherical and conventional tokamaks. *Nuclear Fusion*, 53(6):063025, 2013. doi:[10.1088/0029-5515/53/6/063025](https://doi.org/10.1088/0029-5515/53/6/063025). [Cited on page 29]
- [75] A. K. Swamy, R. Ganesh, S. Brunner, J. Vaclavik, and L. Villard. Collisionless microtearing modes in hot tokamaks: Effect of trapped electrons. *Physics of Plasmas*, 22(7):072512, 2015. doi:[10.1063/1.4927579](https://doi.org/10.1063/1.4927579). [Cited on page 29]
- [76] P. H. Rutherford. Drift instabilities in general magnetic field configurations. *Physics of Fluids*, 11(3):569, 1968. doi:[10.1063/1.1691954](https://doi.org/10.1063/1.1691954). [Cited on page 31]
- [77] J. B. Taylor and R. J. Hastie. Stability of general plasma equilibria - I formal theory. *Plasma Physics*, 10(5):479, 1968. doi:[10.1088/0032-1028/10/5/301](https://doi.org/10.1088/0032-1028/10/5/301). [Cited on page 31]

## References

---

- [78] G. Hammett. Lecture notes on gyrokinetics, 2014. Online [https://w3.pppl.gov/~hammett/talks/2014/gk\\_intro/Hammett\\_GK\\_slab\\_derivation\\_handwritten.pdf](https://w3.pppl.gov/~hammett/talks/2014/gk_intro/Hammett_GK_slab_derivation_handwritten.pdf). [Cited on page 31]
- [79] H. Wilson. Private notes on gyrokinetics, 2018. [Cited on page 31]
- [80] P. Helander and D.J. Sigmar. *Collisional Transport in Magnetized Plasmas*. Cambridge University Press, 2005. ISBN 9780521020985. [Cited on pages 35 and 56]
- [81] P. H. Rutherford, L. M. Kovrizhnikh, M. N. Rosenbluth, and F. L. Hinton. Effect of longitudinal electric field on toroidal diffusion. *Physical Review Letters*, 25(16):1090, 1970. doi:10.1103/PhysRevLett.25.1090. [Cited on page 35]
- [82] I. G. Abel, M. Barnes, S. C. Cowley, W. Dorland, and A. A. Schekochihin. Linearized model fokker–planck collision operators for gyrokinetic simulations. I. theory. *Physics of Plasmas*, 15:122509, 2008. doi:10.1063/1.3046067. [Cited on pages 35, 56, 57, and 79]
- [83] M. Barnes, I. G. Abel, W. Dorland, et al. Linearized model fokker–planck collision operators for gyrokinetic simulations. II. numerical implementation and tests. *Physics of Plasmas*, 16:072107, 2009. doi:10.1063/1.3155085. [Cited on pages 35 and 56]
- [84] I.S. Gradshteyn and I.M. Ryzhik. *Table of Integrals, Series, and Products*. Academic Press, 8 edition, 2014. ISBN 9780123849335. doi:10.1016/C2010-0-64839-5. [Cited on pages 37 and 90]
- [85] M. Abramowitz and I. A. Stegun. *Handbook of Mathematical Functions with Formulas, Graphs, and Mathematical Tables*. U.S. National Bureau of Standards, 9 edition, 1970. ISBN 0486612724. [Cited on page 37]
- [86] GS2 developers. GS2 webpage, 2020. Online <https://bitbucket.org/gyrokinetics/gs2/wiki/Home>. [Cited on page 40]
- [87] GENE developers. GENE webpage, 2020. Online <https://genecode.org>. [Cited on page 40]
- [88] GEM developers. GEM webpage, 2020. Online <https://www.gemgyrokinetic.org>. [Cited on page 40]
- [89] GKW developers. GKW webpage, 2020. Online <https://www.gkw.org.uk/tikiwiki/HomePage>. [Cited on page 40]

- [90] GYRO developers. GYRO webpage, 2020. Online <https://gafusion.github.io/doc/gyro.html>. [Cited on page 40]
- [91] X. Garbet, Y. Idomura, L. Villard, and T.H. Watanabe. Gyrokinetic simulations of turbulent transport. *Nuclear Fusion*, 50(4):043002, 2010. doi:[10.1088/0029-5515/50/4/043002](https://doi.org/10.1088/0029-5515/50/4/043002). [Cited on page 40]
- [92] R. V. Bravenec, Y. Chen, J. Candy, W. Wan, and S. Parker. A verification of the gyrokinetic microstability codes GEM, GYRO, and GS2. *Physics of Plasmas*, 20(10):104506, 2013. doi:[10.1063/1.4826511](https://doi.org/10.1063/1.4826511). [Cited on page 41]
- [93] M. Kotschenreuther, G. Rewoldt, and W. M. Tang. Comparison of initial value and eigenvalue codes for kinetic toroidal plasma instabilities. *Computer Physics Communications*, 88:128, 1995. doi:[10.1016/0010-4655\(95\)00035-E](https://doi.org/10.1016/0010-4655(95)00035-E). Errata at <https://w3.pppl.gov/~hammett/gyrofluid/papers/kot95errata.html>. [Cited on page 41]
- [94] E. A. Belli. *Studies of Numerical Algorithms for Gyrokinetics and the Effects of Shaping on Plasma Turbulence*. PhD thesis, Princeton University, 2006. Online <https://w3.pppl.gov/~hammett/gyrofluid/papers/2006/thesis-belli.pdf>. [Cited on page 41]
- [95] E. Highcock. *The Zero-Turbulence Manifold in Fusion Plasmas*. PhD thesis, University of Oxford, 2012. Online <https://ora.ox.ac.uk/objects/uuid:7ed1774d-88a5-4764-ba06-1de00c348d26>. [Cited on pages 41, 56, and 57]
- [96] M. Barnes, D. Dickinson, W. Dorland, et al. GS2 (v8.0.1). 2019. doi:[10.5281/zenodo.2551067](https://doi.org/10.5281/zenodo.2551067). [Cited on page 41]
- [97] T. M. R. Ellis, I. R. Philips, and T. M. Lahey. *Fortran 90 Programming*. Addison-Wesley Publishing, 1994. ISBN [0201544466](https://www.isbn-international.org/product/0201544466). [Cited on page 46]
- [98] B. Scott. Shifted metric procedure for flux tube treatments of toroidal geometry: Avoiding grid deformation. *Physics of Plasmas*, 8(2):447, 2001. doi:[10.1063/1.1335832](https://doi.org/10.1063/1.1335832). [Cited on page 52]
- [99] T.-H. Watanabe, H. Sugama, A. Ishizawa, and M. Nunami. Flux tube train model for local turbulence simulation of toroidal plasmas. *Physics of Plasmas*, 22(2):022507, 2015. doi:[10.1063/1.4907793](https://doi.org/10.1063/1.4907793). [Cited on page 52]
- [100] J. Ball, S. Brunner, and A. C.J. Eliminating turbulent self-interaction through the parallel boundary condition in local gyrokinetic simulations. *Journal of Plasma Physics*, 86(2):905860207, 2020. doi:[10.1017/S0022377820000197](https://doi.org/10.1017/S0022377820000197). [Cited on page 52]

- [101] M. Hamed, M. Muraglia, Y. Camenen, X. Garbet, and O. Agullo. Impact of electric potential and magnetic drift on microtearing modes stability. *Physics of Plasmas*, 26(9):092506, 2019. doi:[10.1063/1.5111701](https://doi.org/10.1063/1.5111701). [Cited on page 52]
- [102] M. Barnes, W. Dorland, and T. Tatsuno. Resolving velocity space dynamics in continuum gyrokinetics. *Physics of Plasmas*, 17(3):032106, 2010. doi:[10.1063/1.3313348](https://doi.org/10.1063/1.3313348). [Cited on page 56]
- [103] J. F. Parisi, F. I. Parra, C. M. Roach, et al. Toroidal and slab ETG instability dominance in the linear spectrum of JET-ILW pedestals. *Nuclear Fusion*, 60(12):126045, 2020. doi:[10.1088/1741-4326/abb891](https://doi.org/10.1088/1741-4326/abb891). [Cited on pages 63, 64, 73, and 83]
- [104] M. R. Hardman, M. Barnes, C. M. Roach, and F. I. Parra. A scale-separated approach for studying coupled ion and electron scale turbulence. *Plasma Physics and Controlled Fusion*, 61(6):065025, 2019. doi:[10.1088/1361-6587/ab1323](https://doi.org/10.1088/1361-6587/ab1323). [Cited on pages 63 and 83]
- [105] P. N. Shivakumar and C. X. Ji. Upper and lower bounds for inverse elements of finite and infinite tridiagonal matrices. *Linear Algebra and its Applications*, 247:297, 1996. doi:[10.1016/0024-3795\(95\)00113-1](https://doi.org/10.1016/0024-3795(95)00113-1). [Cited on page 69]
- [106] C. M. da Fonseca and J. Petronilho. Explicit inverses of some tridiagonal matrices. *Linear Algebra and its Applications*, 325(1):7, 2001. doi:[10.1016/S0024-3795\(00\)00289-5](https://doi.org/10.1016/S0024-3795(00)00289-5). [Cited on page 69]
- [107] H.-B. Li, T.-Z. Huang, X.-P. Liu, and H. Li. On the inverses of general tridiagonal matrices. *Linear Algebra and its Applications*, 433(5):965, 2010. doi:[10.1016/j.laa.2010.04.042](https://doi.org/10.1016/j.laa.2010.04.042). [Cited on page 69]
- [108] V. Tomeo. Factorization and inversion of finite and infinite comrade matrices. *Computational and Mathematical Methods*, 2(1):e1071, 2019. doi:[10.1002/cmm4.1071](https://doi.org/10.1002/cmm4.1071). [Cited on page 69]
- [109] G. P. M. Poppe and C. M. J. Wijers. Algorithm 680: Evaluation of the complex error function. *ACM Transactions on Mathematical Software*, 16(1):47, 1990. doi:[10.1145/77626.77630](https://doi.org/10.1145/77626.77630). [Cited on page 71]
- [110] E. Anderson, Z. Bai, C. Bischof, et al. *LAPACK Users' Guide*. Society for Industrial and Applied Mathematics, third edition, 1999. ISBN [0898714478](https://www.isbn-international.org/product/0898714478). [Cited on page 71]

- 
- [111] Z. Gao, J. Q. Dong, G. J. Liu, and C. T. Ying. Electromagnetic ion temperature gradient modes of tearing mode parity in high  $\beta$  sheared slab plasmas. *Physics of Plasmas*, 9(5):1692, 2002. doi:[10.1063/1.1471516](https://doi.org/10.1063/1.1471516). [Cited on page 76]
- [112] G. G. Plunk, P. Helander, P. Xanthopoulos, and J. W. Connor. Collisionless microinstabilities in stellarators. III. the ion-temperature-gradient mode. *Physics of Plasmas*, 21(3):032112, 2014. doi:[10.1063/1.4868412](https://doi.org/10.1063/1.4868412). [Cited on page 76]
- [113] Y. C. Lee, J. Q. Dong, P. N. Guzdar, and C. S. Liu. Collisionless electron temperature gradient instability. *Physics of Fluids*, 30:1331, 1987. doi:[10.1063/1.866248](https://doi.org/10.1063/1.866248). [Cited on page 76]
- [114] A. Zocco, N. F. Loureiro, D. Dickinson, R. Numata, and C. M. Roach. Kinetic microtearing modes and reconnecting modes in strongly magnetised slab plasmas. *Plasma Physics and Controlled Fusion*, 57(6):065008, 2015. doi:[10.1088/0741-3335/57/6/065008](https://doi.org/10.1088/0741-3335/57/6/065008). [Cited on page 76]
- [115] H.-S. Xie and Y. Xiao. Unconventional ballooning structures for toroidal drift waves. *Physics of Plasmas*, 22(9):090703, 2015. doi:[10.1063/1.4931072](https://doi.org/10.1063/1.4931072). [Cited on page 76]
- [116] H.-S. Xie, Z.-X. Lu, and B. Li. Kinetic ballooning mode under steep gradient: High order eigenstates and mode structure parity transition. *Physics of Plasmas*, 25(7):072106, 2018. doi:[10.1063/1.5025949](https://doi.org/10.1063/1.5025949). [Cited on page 76]
- [117] M. J. Pueschel, D. R. Hatch, D. R. Ernst, et al. On microinstabilities and turbulence in steep-gradient regions of fusion devices. *Plasma Physics and Controlled Fusion*, 61(3):034002, 2019. doi:[10.1088/1361-6587/aaf8c1](https://doi.org/10.1088/1361-6587/aaf8c1). [Cited on page 76]
- [118] A. Ishizawa, Y. Kishimoto, and Y. Nakamura. Multi-scale interactions between turbulence and magnetic islands and parity mixture - a review. *Plasma Physics and Controlled Fusion*, 61(5):054006, 2019. doi:[10.1088/1361-6587/ab06a8](https://doi.org/10.1088/1361-6587/ab06a8). [Cited on page 76]
- [119] E. Vanden Eijnden and R. Balescu. Statistical description and transport in stochastic magnetic fields. *Physics of Plasmas*, 3(3):874, 1996. doi:[10.1063/1.871791](https://doi.org/10.1063/1.871791). [Cited on page 79]
- [120] M. Neuer and K. H. Spatschek. Diffusion of test particles in stochastic magnetic fields for small Kubo numbers. *Physical Review E*, 73:026404, 2006. doi:[10.1103/PhysRevE.73.026404](https://doi.org/10.1103/PhysRevE.73.026404). [Cited on page 79]

- [121] A. Balbaky, V. Sokolov, and A. K. Sen. The study of the transition regime between slab and mixed slab-toroidal electron temperature gradient modes in a basic experiment. *Physics of Plasmas*, 22(5):052108, 2015. doi:[10.1063/1.4919617](https://doi.org/10.1063/1.4919617). [Cited on page [83](#)]